

NORTHWESTERN UNIVERSITY

Transport Studies of Superconductors for Quantum Applications

A DISSERTATION

SUBMITTED TO THE GRADUATE SCHOOL
IN PARTIAL FULFILLMENT OF THE REQUIREMENTS

for the degree

DOCTOR OF PHILOSOPHY

Field of Physics

By

Kevin Michael Ryan

EVANSTON, ILLINOIS

December 2025

© Copyright by Kevin M. Ryan, 2025

All Rights Reserved

ABSTRACT

In the emerging field of quantum technology, superconducting devices serve many roles and are today the most widely adopted basis for quantum computation. This is because ideally behaved superconductors obey macroscopic quantum phenomena which are relatively easy to manipulate. However, in the laboratory things are almost never ideal, and the superconducting quantum devices which are hoped to someday yield fully fault tolerant quantum computers are in fact, quite faulty. Chief among their most pressing issues are excitations of the superconductor itself out of its many-body ground state, and other stray defects which can arise during construction of these devices. These issues, known colloquially as quasiparticle poisoning and two-level systems respectively, continue to be the subject of considerable study and will require extensive and detailed examinations if we are going to someday obtain truly competitive quantum computers.

With this in mind, in this thesis we present studies into both quasiparticles and material defects in superconductors. By taking a transport approach to process development, we have explored the phenomenology of both conventionally prepared superconducting films and those produced via emerging techniques, so as to develop metrics for comparing superconducting devices. Via corroboration with material investigations, we have established compelling connections between inhomogeneity and transport properties which may be important in future developments. In parallel, we explore quasiparticle dynamics in the low temperature regime to better establish how these excitations behave collectively and shed new light on their fundamental behaviors. Such non-equilibrium transport studies of superconductors allow for rich, spectroscopic examination of quasiparticle interactions and may ultimately allow us to answer open questions on both the origin and mitigation of quasiparticle poisoning.

ACKNOWLEDGEMENTS

This thesis, completed in pieces over what now seems like an endless series of tangentially related projects taken on during my time at Northwestern, is the culmination of seven years of effort into developing unconventional techniques for precision transport experiments in emerging areas of condensed matter physics. In this time, I have had the pleasure to work with a great many people on an even greater number of projects (and side projects). Picking things up a little at a time across so many topics has given me a great breadth of experience as an experimentalist, but an even greater respect for the expertise of my many peers and colleagues. Without the companionship of my friends, family and collaborators; the support of Northwestern University and of the Physics and Astronomy Department; and the leadership and guidance of my mentors, none of the work I have completed today would be possible. This is especially true thinking back on the extraordinary circumstances under which we have all been working since 2019. All of us have faced immense challenges during these last few years, which have felt like a constant sequence of new and extraordinary roadblocks to science and progress. It goes without saying that we have weathered and will continue to weather these storms somehow, even if we can't always see the way to a lasting calm.

With these things said, I am pleased to have many people to dedicate this thesis to.

First and foremost, forever and always, I write this for the love of my life Stephanie Elise Ryan. Through every challenge, every success and every failure along the way she has supported me without hesitation. She has been a part of me and my journey as a physicist at every step, and without her I would never have had the strength or the courage to pursue my dreams. I owe her everything—She is my everything.

For my father, a role-model, a benefactor and a guide through my (now quite-very-many) college years, and also a fellow academic with an unparalleled work ethic and moral conviction. And for my mother, ever understanding and deeply considerate, without whom I might never have known I was able to achieve much at all. I love them always.

To my current lab mates, most importantly, to Max, Yanpei, Austin and Jasmine, and to Lila and Andrew, and to my other former mentees and colleagues, and to our future successors. I will miss working alongside each of them. Not just for the cardgames and happy-hours, but also the emergency pump-repairs and blocked reliquifiers, and the papers and meetings and midnight emails. All of it (with a little hindsight) has been instrumental not just to my own work, but to giving that work purpose and blessing me with the motivation to complete this thesis. The research we do is not possible if we work alone, and I hope they continue to take care of and learn from each-other well into the future.

To the many collaborators I have worked with who have helped me find the heart of my own research. One does not learn in a vacuum, and so I give everyone thanks for their contributions.

To John Scott, a truer peer I have never met, and none a better friend. I have nothing but kind words, but words are probably not enough to express my respect and admiration anyway. We came into Northwestern together, and have been fast friends the whole time. Although I may be graduating first, I trust he will be close behind, and I wish him all the best.

Finally, I give my thanks to Venkat, with whom I have had the pleasure to work alongside, and from whom I have learned so much of physics, life, and academia. He is an essential leader and role-model not just to our lab, but to the entire condensed matter program at Northwestern as we know it today. It hasn't always (*or even often*) been easy, but Venkat has lead us through so much, and I am so glad to have learned all that I have from him.

Glossary

Notation	Description
$D (D_N)$	Diffusion Coefficient (Normal State).
E_k	Single Quasiparticle Excitation Energy.
$G (G^N)$	Conductance (Normal State).
G_{BA}	Non-local Conductance at B due to A .
$H_{c, c1, c2}$	Superconducting Thermodynamic, 1st, and 2nd Critical Fields.
$I_c (J_c)$	Critical Current (Density).
$I_{A/B}, V_{A/B}$	Injector/Detector Current, Voltage Bias.
L_T	Thouless Length.
N_0	Density of States at the Fermi-level.
$N_S (N_N)$	Superconducting Density of States (Normal Case).
Q^*	Quasiparticle Charge Imbalance.
$R (R^N)$	Resistance (Normal State).
RRR	Residual Resistance Ratio.
T^*	Effective Quasiparticle Temperature.
T_1 / T_2	Decoherence/Dephasing Time.
T_c	Superconducting Critical Temperature.

Notation	Description
X	Separation Between Non-local Junctions.
Δ	Superconducting Gap Energy.
Γ	Dynes Parameter/Energy.
Ω_{\square}	Sheet Resistance.
Φ_0	Superconducting Flux Quanta.
δf_k	Non-Equilibrium Deviation of the Distribution Function.
$\gamma_k^{\dagger} / \gamma_k$	Quasiparticle Creation/Annihilation Operators.
\hat{N}	Cooper-pair Number Operator.
$\hat{\phi}$	Superconducting Phase Operator.
$\hat{\tau}^i$	Nambu-space Pauli Matrices.
κ	Ginzburg-Landau Parameter.
λ_{BCS}	BCS Coupling Parameter.
$\lambda_{eff} / \lambda_L$	Effective/London Penetration Depth.
μ (μ_{Q^*})	Chemical Potential (Charge Imbalance Case).
$\sigma^{x,y,z}$	Pauli-spin Matrices in TLS Eigenbasis.
τ_{Eff}	Effective Inelastic Scattering Time.
τ_E	Inelastic Scattering Time.
τ_N	Nyquist Scattering Time.
$\tau_{Q^*} / \tau_{\Delta}$	Charge/Gap Relaxation Time.
τ_{ee}	Electron-electron Scattering Time.

Notation Description

$\tilde{g}^{R,A,K}$	Retarded, Advanced, and Keldysh Green's Functions.
ξ (ξ_0)	Superconducting Coherence Length (Zero Temperature).
ξ_k	Single Quasiparticle Energy.
c_k^\dagger / c_k	Electron Creation/Annihilation Operators.
d	Sample Thickness.
f_k (f_0)	Distribution Function (Equilibrium Case).
h_L / h_T	Quasiclassical Longitudinal/Transverse Distribution Functions.
k_f (v_f)	Fermi-wavevector (-velocity).
l	Sample Length.
l_{mfp}	Carrier Mean Free Path.
q_k	Quasiparticle Charge.
u_k / v_k	Complex BCS Coherence Factors.
v_s	Superfluid Velocity.
w	Sample Width.
x_{qp}	Fractional Quasiparticle Density.

TABLE OF CONTENTS

Abstract 3

Acknowledgments 6

Glossary 8

List of Figures 13

List of Tables 17

Chapter 1: Introduction 18

Chapter 2: Background and Theory 21

 2.1 Superconducting Quantum Devices 21

 2.1.1 A Generic Hamiltonian for a Superconducting Qubit 22

 2.1.2 Quasiparticle Poisoning of Qubits 25

 2.1.3 Two-Level Systems and Other Defects in Qubits 33

 2.2 Non-equilibrium Superconductivity 39

 2.2.1 The BCS Ground-state and Quasiparticle Excitations 39

	10
2.2.2	Quasiparticles at Finite Temperature 44
2.2.2.1	Quasiparticle Excitation from Athermal Sources 50
2.2.3	Quasiparticle Non-equilibrium 51
2.2.4	Quasiparticle Tunneling from a Normal Metal 55
2.2.5	Quasiparticle Transport in Superconductors 59
2.2.5.1	Quasiclassical Description 62
2.3	Superconducting Phenomenology 69
2.3.1	Ginzburg-Landau Phase Boundary 69
2.3.1.1	Notes on Superconductivity in Nb 75
2.3.2	Current and Phase in Superconducting Wires 78
Chapter 3: Methods 81
3.1	Lithography and Fabrication 81
3.1.1	Physical Vapor Deposition 82
3.1.2	Photolithography and Ion Milling 85
3.1.2.1	Recipe for Soft Masked Ar Ion Milling 85
3.1.3	Electron Beam Lithography and Deposition 88
3.1.3.1	SEM Interface Buffers 89
3.1.3.2	Recipes for Electron Beam Lithography and Deposition 90
3.1.3.3	Recipes for Electron Beam Lithography and Reactive Ion Etching 93
3.2	Measurement and Control 95

	11
3.2.1 Sample Mounting	95
3.2.2 Conductance Measurements	96
3.2.2.1 2+1 Terminal Quasiparticle Conductance Measurements	100
3.2.2.2 2+1(+1) Terminal Quasiparticle Chemical Potential Measurements	102
3.2.3 Feedback Controlled Measurements	103
Chapter 4: Niobium Films for Superconductivity Devices	106
4.1 Superconducting Phase Boundary Studies of Niobium Films used in Qubits	106
4.1.1 Results on HiPIMS Nb Films	107
4.1.1.1 HiPIMS Nb on Si	107
4.1.1.2 HiPIMS Nb on Sapphire	110
4.1.2 Results on DC Sputtered Nb Films on Si	114
4.1.3 Results on PLD Grown Films on Al ₂ O ₃	116
4.2 PPMS Studies of High Temperature Nb Films Grown on Al ₂ O ₃	119
Chapter 5: Quasiparticle Transport Studies	127
5.1 Observations of Quasiparticles via Charge Imbalance	128
5.1.1 Enhancement of Quasiparticle Relaxation in Cu/Al Bilayers	129
5.1.1.1 Estimating Inelastic Rates in Al and Cu Wires and Bilayers	137
5.1.2 Voltage Asymmetry of the Quasiparticle Chemical Potential	140
5.2 Dual Bias Experiments in Junction Array Devices	143

5.2.1	Dual Bias Differential Voltage Measurements	145
5.2.2	Replication Studies and Issues with Differential Voltage Detection	148
5.3	Results on a Mesoscopic Thin Film Device	151
5.3.1	Basic Characterization and Non-local Conductance	152
5.3.1.1	Evidence for Energy Mode Non-equilibrium	154
5.3.2	Effect of a Large in Plane Magnetic Field	157
5.3.3	Imbalance Mode Mixing via Supercurrent Injection	160
Chapter 6: Conclusions and Future Work		166
6.1	On Transport Measurements in Nb	166
6.2	On Quasiparticle Non-equilibrium	167
Vita		188

LIST OF FIGURES

2.1	Energy level tuning between Cooper Pair Boxes (CPB) and transmon qubits.	25
2.2	Rabi-oscillation between a current biased qubit and individual TLSs.	35
2.3	Electrostatic gating of TLS defects resonantly coupled to frequency tunable qubits.	36
2.4	Quasiparticle excitation energy E_k and charge q_k as a function of ξ_k	43
2.5	Quasiparticle density of states, occupation and BCS coherence factors as a function of E_k	46
2.6	Dynes model of the quasiparticle density of states.	47
2.7	Self consistent BCS gap and quasiparticle suppression as a function of temperature.	50
2.8	Normalized conductance spectra calculated for an Al based NIS tunnel junction as a function of voltage.	57
2.9	Dual-band gap structures for Nb at each point of the Fermi surfaces.	76
3.1	Example Hall bar produced via photolithography.	87
3.2	Images of the new Tescan SEM for EBL.	89
3.3	Fabrication process used to produce bilayers with normal metal tunnel junctions for non-local conductance measurements.	92
3.4	Process for fabrication of RIE defined devices with EBL patterning.	93

3.5	Circuit schematic for a voltage-biased transimpedance pre-amplifier for conductance measurements.	98
3.6	Equipment layout for a 2+1 terminal conductance measurement.	101
3.7	Thermal hysteresis in $R(T)$ under applied magnetic fields.	103
3.8	Representative errors in phase boundary analysis due to sweep rate.	104
4.1	$H - T$ phase boundaries of HiPIMS Nb on Si films for different film thicknesses.	108
4.2	$H - T$ phase boundaries of HiPIMS Nb on Si films for differently prepared Si substrates.	109
4.3	AFM micrographs of as deposited and UHV annealed 40 nm Nb films on a- and c- Al_2O_3 substrates.	111
4.4	Transition width broadening and effective coherence lengths for 40 nm Nb films on a- Al_2O_3 and c- Al_2O_3 substrates.	112
4.5	$H - T$ phase boundaries for UHV annealed 40 nm thick Nb films on a- Al_2O_3 substrates.	113
4.6	$H - T$ phase boundaries and extracted coherence lengths for dc-sputtered 40 nm Nb films on Si (001) and H:Si (111) substrates.	115
4.7	Epitaxial relations and $R(T)$ traces for PLD grown Nb on a- Al_2O_3	117
4.8	$H - T$ phase boundary diagram for a PLD grown epitaxial Nb film along the principle crystallographic directions.	118
4.9	AFM Mapping of a PLD grown Nb film on a- Al_2O_3 and its underlying substrate.	119
4.10	XRD measurements of HT and RT Nb samples on a- Al_2O_3 samples subject to various post-annealing conditions in UHV.	120
4.11	$R(T)$ and $RRR(\theta_{110})$ for RT and HT devices of the annealing study.	121

4.12	$R(T)$ near the superconducting transition and $T_c(\theta_{110})$ for RT and HT devices of the annealing study.	123
4.13	$R(H)$ near the superconducting transition for RT and HT devices of the annealing study.	124
5.1	Schematic of the non-local injector/detector scheme and example device used for charge imbalance measurements.	131
5.2	Local conductance of junctions and temperature characterization of the control and bilayer devices.	132
5.3	Quasiparticle conductance as a function of X for both the control and bilayer devices.	134
5.4	Fits to λ_{Q^*} and g^* for both the control and bilayer devices.	136
5.5	Extracted values of λ_{Q^*} and τ_E^{-1} for the control device as a function of injector bias V_A	138
5.6	Nonlocal differential-voltage measurements of the control and bilayer devices, and further analysis.	140
5.7	Dual-bias conductance measurements for $X = 2 \mu\text{m}$ of both the bilayer and control devices.	144
5.8	Schematic of the three junction differential measurement.	146
5.9	Three junction differential voltage/conductance measurement on the control device.	147
5.10	SEM micrographs of the short junction, three terminal device for the replication study.	148
5.11	Characteristic data obtained from the three terminal device used in the replication study.	149
5.12	SEM micrographs of the mesoscopic three terminal devices.	151
5.13	Local conductance of a representative junction used in the mesoscopic device. . . .	153

5.14	Local and non-local conductance data on the A, B junction pair of the mesoscopic device.	154
5.15	Non-local conductance measurements of the A, B and A, C junction pairs on the mesoscopic device.	155
5.16	Local conductance spectra of the A, B junction pair of the mesoscopic device, with and without an in plane field.	158
5.17	Local and non-local conductance of the mesoscopic high field device in a 1T magnetic field.	159
5.18	Local conductance and injector current measured during the application of a supercurrent across the mesoscopic device as a function of I_S	161
5.19	Local conductance and injector current measured during the application of a supercurrent across the mesoscopic device as a function of V_A	162
5.20	Fits to the local conductance of the mesoscopic device during supercurrent injection.	162
5.21	Non-local conductance and detector current measured over a range of I_S values, as a function of V_A	163
5.22	Symmetry decompositions of the I_S biased non-local conductance G_{BA}	164

LIST OF TABLES

2.1	Probability and possible outcomes due to electron tunneling across an NIS junction.	58
3.1	Typical deposition conditions for metals prepared via electron-beam deposition. . .	83
3.2	Recipe for photolithography of Nb devices	86
3.3	Process parameters for etching Nb films via Ar Ion Mill.	88
3.4	Recipe for EBL defined samples using a PMMA/PMGI process.	91
3.5	Parameters for etching Nb films via the SAMCO RIE system.	94
4.1	Zero field transition properties of HiPIMS deposited films.	107
4.2	Description and bulk transport properties of two studied directions for PLD grown Nb films.	116
5.1	Deposition conditions during device fabrication for control and proximity effect bilayer devices.	129
5.2	Measured and Drude model calculated values for both control and bilayer devices. .	137
5.3	Normal state transport properties and physical dimensions of the junctions used in the mesoscopic device.	152

CHAPTER 1

INTRODUCTION

Over the last 25 years, superconducting quantum devices have risen to prominence and are now driving many emerging quantum technologies. At their core, these systems descend from concepts first explored in the context of mesoscopic superconductivity, although the two fields have diverged considerably over time. In principle, the earliest “true” quantum devices, such as the Cooper-pair box first demonstrated by Nakamura et al. in 1999 [1], were extensions of many earlier experiments on the Coulomb blockade effect dating back to work by Fulton and Dolan on single electron transistors [2]. Over time, experiments involving the quantum coherence of mesoscopic devices on topics such as quantum phase slips [3], Josephson tunneling [4], and charging effects due to single Cooper-pairs [5] ultimately led to the modern study of the readout and control of addressable quantum states.

Moving towards the present, considerable work has gone into formalizing the language of quantum information, developing tool-sets for calculations and extending these experiments into the high frequency domain. State of the art quantum devices now have lifetimes as high as $T_1 \gtrsim 1$ ms [6] and extremely low operational errors have been demonstrated [7]. Nevertheless, there continue to be serious questions about the actual mechanisms responsible for limiting the performance of existing quantum technologies, especially in their construction [8, 9, 10, 11, 12, 13] and apparent non-equilibrium dynamics [14, 15, 16, 17, 18].

In the spirit of these issues, this thesis explores two topics in superconductivity which may be sig-

nificant in the development of future superconducting quantum devices, by returning to mesoscopic effects via dc transport experiments. The first matter will be the nature of the superconductivity evident in deposited metal films used in quantum computers at the moment. We will explore the behavior of the superconducting state in such materials, and demonstrate that many current generation quantum devices are built upon impure Nb films at an interesting boundary between amorphous and epitaxial. The second topic of importance for this thesis are the fundamental excitations of superconductors, and the nature of non-equilibrium Bogoliubov quasiparticles. Non-equilibrium superconductivity has been a subject of considerable scrutiny for over five-decades. To explore this topic anew we have performed several state of the art measurements on quasiparticle dynamics in superconductors and proximity effect bilayers at mK temperatures. In this regime, we find a number of surprising effects and unexplained physics occurring in the quasiparticle dynamics of low temperature superconductors which may have significant implications for quantum devices.

This thesis is structured into the following chapters:

Chapter two consists of two parts. The first contains an introduction to elementary superconducting quantum devices and their Hamiltonian; outlines several of the issues related to quasiparticle tunneling in quantum bits; and finally addresses the mechanisms by which defects can couple to these devices. In the second part, we consider important elements of superconductivity, particularly related to non-equilibrium quasiparticles, as well as certain bulk phenomena which are necessary to understand the superconducting behavior of Nb films we have studied under applied magnetic fields.

Chapter three will consist of the methods used to perform the dc transport measurements which form the experimental body of this thesis. In particular, we will outline many important details relevant for replication of the present results; describe the basis for much of the home-built equip-

ment used in our measurements; and provide some detailed recipes for device fabrication which may be of future use.

Chapter four consists of bulk materials characterization of Nb films grown by partners in the Superconducting Quantum Materials and Systems Center, particularly at Rigetti Computing and the National Institute of Standards and Technology. These studies compliment several works, both published and unpublished, at Northwestern University as part of this center. From these results, we make several recommendations about the preparation of Nb films for quantum devices, and in general find that there is considerable room for advancement towards the clean-limit in Nb films.

Chapter five explores quasiparticle non-equilibrium via electron tunneling in Normal-Insulator-Superconductor devices. In the first major finding of this chapter, we demonstrate a means by which quasiparticle relaxation can be substantially tuned by induced disorder in a proximity effect bilayer, and comment on possible applications of this effect. Then, we consider as-yet unexplained measurements of non-equilibrium quasiparticles in superconducting wires, which allow us to argue that the relaxation and recombination of such non-equilibrium states at mK temperatures remains poorly understood.

Finally, chapter six contains a summary of these findings; concluding remarks on the state of superconductivity within modern superconducting quantum devices; and ideas for several future experiments which would continue in the direction of this work.

CHAPTER 2

BACKGROUND AND THEORY

2.1 Superconducting Quantum Devices

At present, there is a great deal of interest on quantum systems which can be dynamically coupled to measurement devices to manipulate, transport or read out the wavefunction of an ensemble quantum states. Many systems have been proposed or demonstrated in this functionality, and can be broadly categorized into atomic [19] (i.e. physical transitions in isolated matter), bosonic [20] (i.e. photonic/photonic modes of resonant cavities), and solid state [21, 22] (i.e. quantum degrees of freedom in a material) quantum systems. Superconducting quantum devices are unique in this regard as one of the few (potentially only true) systems in which a quantum state can be mapped onto the macroscopic behavior of an *entire* system in the thermodynamic limit. Rather than encoding an isolated object or subsystem of a device (or distributing the information across a countable number of non-interacting quantum states etc.) each superconducting device, often on the mm size scale, contains a single quantum state corresponding to its global, macroscopic wavefunction Ψ . As a result, it is relatively easy to construct and interact with such devices, and they are currently the most widely deployed type of quantum device for research around the world. Conversely, superconducting quantum devices are strongly coupled to their defects and to their environment, as well as microscopic and macroscopic sources of energy loss which limit their coherence lifetimes dramatically compared to other platforms. As the quantum state is essentially a property of the entire device, determining the exact origin of these limits is a challenging and long standing issue.

To begin to unpack this topic, we must first consider how the Hamiltonian of such a system can become coupled to sources of decoherence. This will lead into two broad topics of this thesis: macroscopic/materials sources of decoherence and on microscopic and non-equilibrium effects in superconductors .

2.1.1 A Generic Hamiltonian for a Superconducting Qubit

While numerous descriptions exist to derive a functional qubit Hamiltonian, for the purpose of this introduction we will follow closely the work of L. Glazman and G. Catelani [23, 24], with supplementary citations where appropriate, as this will lead naturally to a description of quasiparticle induced qubit transitions. This most basic description starts by considering the Hamiltonian of two superconducting islands linked by a tunnel junction. On each island, we define the operator $\hat{\phi}$ as the phase of the order parameter and \hat{N} to be the number of Cooper-pairs, which obey a the canonical commutation relationship

$$\left[\hat{N}, \hat{\phi} \right] = 1 \quad (2.1)$$

such that

$$\hat{N} = \frac{1}{i} \frac{d}{d\phi}. \quad (2.2)$$

In linking the islands with a tunnel junction, it is well known that a “Josephson current” of tunneling Cooper pairs is established, and is sinusoidal in the difference in the phases ϕ_L and ϕ_R between the left and right islands

$$I_J = I_c \sin(\phi_R - \phi_L), \quad (2.3)$$

where I_c is the critical current of the junction itself. From this the Josephson energy component of the Hamiltonian will be

$$H_J \equiv \int I_J \times d(\phi_R - \phi_L) = -E_J \cos(\phi_R - \phi_L). \quad (2.4)$$

This comes from the energy stored in the Josephson current, and has a magnitude $E_J \propto I_c$. The critical current of a symmetric superconducting tunnel junction is generally known by the Ambegaokar-Baratoff relation to approximately behave as

$$I_c R^N = \frac{\pi}{2e} \Delta(T) \tanh\left(\frac{\Delta(T)}{2k_B T}\right), \quad (2.5)$$

where we have introduced $\Delta(T)$ as the temperature dependent superconducting gap of the material, while R^N is the normal state resistance of the junction due to tunneling of charge carriers. For very small junctions, this resistance is large due to the lack of available conductance paths via tunneling, and the corresponding I_c is reduced. Note that the gap value is that of the superconducting element on either side of the junction. In many devices, this junction is composed of Al, while the remainder of the device is composed of Nb formed by a separate lithographic step (to add capacitance etc.). As these materials have very different superconducting gaps, one must keep in mind that the gap value which appears here is of only the Al junction. This distinction may be important when considering the effective parameters of certain models, but is not important for the following analysis.

When a Cooper-pair tunnels across the junction, it adds a charge of $2e$ to the charge on one of the islands, which given some capacitance C between them will contribute a charging energy to the Hamiltonian. In the presence of unpaired electrons or an external voltage-bias, there can also be a charge n_g on the opposing island which also contributes to this potential energy, giving us a

term

$$H_C = 4E_c \left(\hat{N} - n_g \right)^2, \quad (2.6)$$

where $E_c = e^2/2C$ is the charging energy of a single electron. The construction is identical to what is typically followed in describing the Coulomb blockade effect for a metallic island [25, 26], although it must be kept in mind that this is actually a continuous, periodic function of n_g with a period of $2e$. When applying an external voltage bias, this is essentially the polarization surface charge between the superconducting island and the gate electrode.

Putting these together and expressing everything in terms of the operator ϕ (i.e. $\phi = \phi_R - \phi_L$) we have a sinusoidal-well Hamiltonian for the qubit

$$H_\phi \equiv H_c + H_J = 4E_c \left(\frac{1}{i} \frac{d}{d\phi} - n_g \right)^2 - E_J \cos \phi, \quad (2.7)$$

which is suitable for describing simple qubits such as charge-/phase-qubits or transmons [27].

The energy levels within this potential well are discrete and not evenly spaced (as they would be in a harmonic oscillator) due to the $\cos \phi$ term, however fluctuations in n_g will shift the energy levels randomly. For this reason, transmon qubits introduce a large capacitance to increase the ratio of E_J/E_c , which flattens out the dependence of the energy levels with n_g and makes them insensitive to that degree of freedom [27]. This is shown schematically in Fig. 2.1, which also serves to explain the periodicity with respect to n_g (in units of $2e$). This stability has led to transmons and their general variants to be the predominant style of superconducting qubit currently in use, and places the excitation energy to be $\approx \sqrt{8E_J E_C}$. For most applications, this is chosen to give an angular excitation frequency ω_0 of about 5 GHz, which is 1 to 2 orders of magnitude smaller than

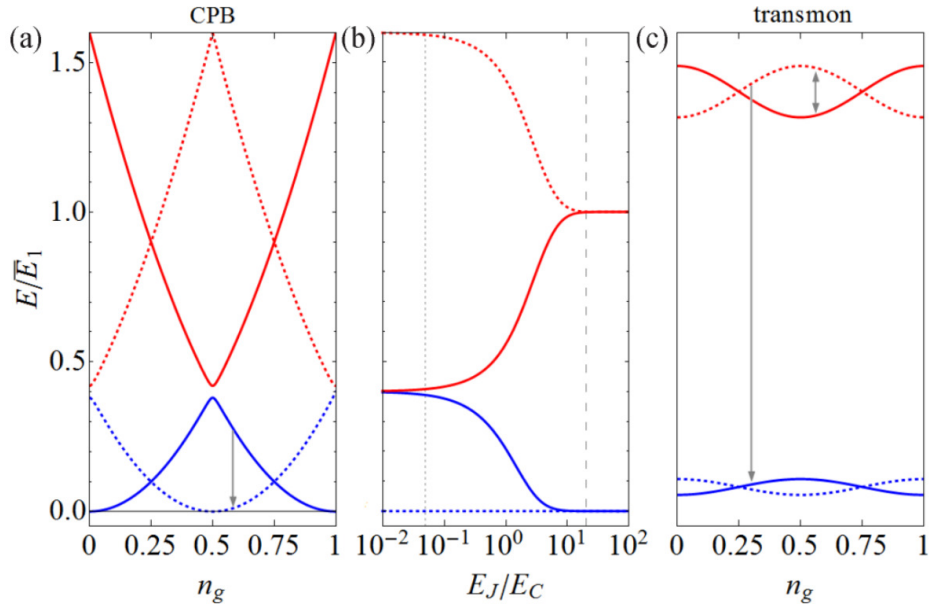


Figure 2.1: Energy level tuning between Cooper Pair Boxes (CPB) and transmon qubits, based on the ratio E_J/E_C , reproduced from Ref. [28]. “Solid (dotted) lines are used for even (odd) parity states in all panels. Arrows denote possible quasiparticle-induced transitions. (a) Energy levels as functions of n_g for a Cooper pair box with $E_J/E_C = 0.05$. Energy is normalized by the average energy of the third and fourth state, $\bar{E}_1 = (E_{1e} + E_{1o})/2$, at $n_g = 1/2$. (b) Energy of the four lowest states at $n_g = 1/2$ as function of the ratio E_J/E_C . The vertical scale is the same as in panel (a). The vertical dotted line is at $E_J/E_C = 0.05$, while the dashed line at $E_J/E_C = 20$ demarcates the transmon regime to its right. (c) schematic representation (energies not to scale) of the energy levels as functions of n_g for a transmon.”

Δ/\hbar for the superconductors most commonly used today. On a final note, while we are discussing these as “qubit” systems, there are always higher energy levels which can be accessed above the first excited states.

2.1.2 Quasiparticle Poisoning of Qubits

So far, the only external variable to this Hamiltonian is contained in the number of unpaired electrons n_g . As we will describe in more detail later, unpaired electrons are not energy eigen-states of the BCS model, which are instead “quasiparticles”, or many body excitations which carry

charge and momentum in addition to that of the condensate. As such, when describing lone electrons we use the Bogoliubov transformation, [29]

$$c_{k\uparrow} = u_k^* \gamma_{k\uparrow} + v_k \gamma_{-k\downarrow}^\dagger, \quad (2.8)$$

$$c_{-k\downarrow}^\dagger = u_k \gamma_{-k\downarrow}^\dagger - v_k^* \gamma_{k\uparrow}, \quad (2.9)$$

to diagonalize the BCS Hamiltonian (as we will see later in §2.2.1). Now, we will consider the creation operator $c_{k\uparrow}^\dagger$ which corresponds to an electron with spin up and positive momentum to be composed of quasiparticles and quasi-holes of opposite spin and momentum, with complex weights u_k and v_k . These must be chosen to correctly diagonalize the BCS wavefunction at quasiparticle energies ξ_k . To do this, one finds that

$$|v_k|^2 = \frac{1}{2} \left(1 - \frac{\xi_k}{\sqrt{\xi_k^2 + \Delta^2}} \right) \equiv \frac{1}{2} \left(1 - \frac{\xi_k}{E_k} \right) \quad (2.10)$$

in which

$$E_k = \sqrt{\xi_k^2 + \Delta^2} \quad (2.11)$$

is the total energy required to *excite* a quasiparticle into that energy state [30]. By normalization, we have also

$$u_k^2 = 1 - v_k^2 = \frac{1}{2} \left(1 + \frac{\xi_k}{E_k} \right). \quad (2.12)$$

As we will discuss later in § 2.2.1, the BCS coherence factors u_k and v_k are complex quantities which are related by a factor $e^{i\phi}$ due to the requirement that the combination $\Delta_k^* v_k / u_k$ is a real

valued function of energy [29]. Similarly, the density of the available quasiparticle states will turn out to be proportional to E_k/ξ_k , and thus diverges at $E_k = \Delta$.

We will be concerned shortly with the tunneling of quasiparticles or electrons, where certain conservation rules can become obscured by the notation. This occurs when one does not account for the creation or annihilation of Cooper-pairs when constructing the corresponding operators for γ^\dagger , as it is commonly the case that the total number of Cooper-pairs is not-conserved. To avoid this, one sometimes chooses to include an operator S for the annihilation of a Cooper pair [31] in these definitions:

$$\gamma_{k\uparrow}^\dagger = u_k^* c_{k\uparrow}^\dagger - v_k^* S^\dagger c_{-k\downarrow}, \quad (2.13)$$

$$\gamma_{-k\downarrow} = u_k c_{-k\downarrow} + v_k S c_{k\uparrow}^\dagger. \quad (2.14)$$

The excitation of a $k \uparrow$ quasiparticle is now evidently a combination of the creation of an electron and the creation of a hole *and* a Cooper pair, such that the change in the total charge is always $1e$, even when the resulting charge is shared between the quasiparticle and the condensate.

The presence of quasiparticles (indexed now by n) and their tunneling across the junction contribute two additional terms to the qubit Hamiltonian. The first consists of just the energies of the quasiparticles themselves,

$$H_{qp} = \sum E_n \gamma_n^\dagger \gamma_n, \quad (2.15)$$

and is thus not immediately consequential. The second contribution consists of transport of a quasiparticle from the left to the right island (or vice versa) by tunneling, and requires some key physical assumptions to obtain. The approach taken by Glazman and Catelani pre-supposes that

tunneling across the Josephson junction occurs via either Cooper-pairs or single electrons. The latter case would connect the islands via a Hamiltonian with terms that go as $c_{nL\sigma}^\dagger c_{nR\sigma}$ for both spin orientations σ , where subscripts L, R denote separate sub-spaces for electrons on the left and right islands. Expanding such a combination gives two dissimilar components

$$c_{L\sigma}^\dagger c_{R\sigma} = (u_L u_R^*) \gamma_{L,k\sigma}^\dagger \gamma_{R,k\sigma} - (v_L^* v_R) \gamma_{L,-k\bar{\sigma}} \gamma_{R,-k\bar{\sigma}}^\dagger \quad (2.16)$$

$$+ (u_L v_R) \gamma_{L,k\sigma}^\dagger \gamma_{R,-k\bar{\sigma}}^\dagger - (v_L^* u_R^*) \gamma_{L,-k\bar{\sigma}} \gamma_{R,k\sigma}. \quad (2.17)$$

This highlights the somewhat tricky aspect of these operators. Clearly in tunneling an electron, there are terms in which quasiparticles or quasi-holes are added or removed from *both* sides of the junction (with opposite spin and momentum) to transfer the electron. However the remaining terms in Eq. 2.17 add or remove a quasiparticle and a quasi-hole to or from both sides, which corresponds to breaking a Cooper pair and moving half of the resulting charge instead. From an energy perspective, these two terms require a $2\Delta/\hbar$ photon/phonon to participate in the tunneling, which is said to be inconsequential for low energy perturbations of the qubit. Dropping those terms, one arrives at the following Hamiltonian for quasiparticle tunneling.

$$H_{qp}^T = \sum_{\sigma, n_L, n_R} t_{n_L, n_R} (u_{n_L} u_{n_R}^* - v_{n_L} v_{n_R}^*) \gamma_{n_L \sigma} \gamma_{n_R \sigma}^\dagger + H.C.. \quad (2.18)$$

The summation index σ again corresponds to spin of the quasiparticle (which is preserved during tunneling) while, n_L and n_R are the energy indices of the quasiparticle states on either side of the junction. $H.C.$ denotes the remaining terms of the Hermetian conjugate. The prefactor t_{n_L, n_R} is the matrix element determining the rate of tunneling across the junction.

Before considering this further, one might wonder why any coherence factors would appear at all,

as we could have just as easily started with a term $\gamma_L \gamma_R^\dagger$ associated with taking a quasiparticle with momentum $+k$ and spin-up from the left side of the junction and tunneling it into the right. To see how this would work, let us expand this in terms of the relations given in Eq. 2.1.2. This keeps track of the pair-breaking terms more easily, yielding:

$$\gamma_{k\uparrow,L} \gamma_{k\uparrow,R}^\dagger = (u_k c_{k\uparrow} + v_k S c_{-k\downarrow}^\dagger)_L (u_k^* c_{k\uparrow}^\dagger - v_k^* S^\dagger c_{-k\downarrow})_R \quad (2.19)$$

$$\equiv (u_k c_{k\uparrow})_L (u_k^* c_{k\uparrow}^\dagger)_R - (v_k S c_{-k\downarrow}^\dagger)_L (v_k^* S^\dagger c_{-k\downarrow})_R \quad (2.20)$$

$$- (u_k c_{k\uparrow})_L (v_k^* S^\dagger c_{-k\downarrow})_R + (v_k S c_{-k\downarrow}^\dagger)_L (u_k^* c_{k\uparrow}^\dagger)_R. \quad (2.21)$$

Clearly we have the same issue as before. The first two terms are associated with tunneling of a single $k \uparrow$ electron, and a single $-k \downarrow$ electron plus tunneling of a pair in the other direction, and once summing over k we would have the same coherence factor of $u_{n_L} u_{n_R}^* - v_{n_L} v_{n_R}^*$. The latter terms once more contain pair-breaking and require a 2Δ photon/phonon, and would be dropped by the same argument as before. Again, every term still amounts to a single e charge being transferred across the junction in one way or another. This correspondence implies that either quasiparticle tunneling or electron tunneling across a qubit amounts to a transformation which always respects the fact that charge transfer is quantized on the galvanically isolated qubit itself. As the quasiparticles described by γ_k can have a charge of less than e , the expectation value of the total charge transferred is accounted for by combinations of these terms, and thus the coherence factors keep everything consistent.

Picking back up at Eq. 2.1.2, Glazman and Catelani perform the gauge choice that $u = u^*$ for both sides of the qubit, such that $v_{n_{L/R}} = |v_{n_{L/R}}| e^{i\phi_{L/R}}$, to account for the total phase difference between the two sides. As we defined the operator $\hat{\phi}$ to be the phase difference across the junction,

the coherence factors can be rephrased as

$$\left(|u_{n_L}u_{n_R}| - |v_{n_L}v_{n_R}|e^{-i\hat{\phi}}\right) \gamma_{n_L\sigma}\gamma_{n_R\sigma}^\dagger \equiv \left(|u_{n_L}u_{n_R}|e^{i\hat{\phi}/2} - |v_{n_L}v_{n_R}|e^{-i\hat{\phi}/2}\right) \gamma_{n_L\sigma}\gamma_{n_R\sigma}^\dagger. \quad (2.22)$$

In this last step, a global phase factor is applied as a gauge choice to simplify the later results. Putting this into the Hamiltonian, it can be seen that H_{qp}^T is in fact an interaction Hamiltonian between the qubit's phase degree of freedom and the occupation of quasiparticles on both sides by tunneling, due to the product of the qubit phase $\hat{\phi}$ and the quasiparticle tunneling operators γ :

$$H_{qp}^T = \sum_{\sigma, n_L, n_R} t_{n_L, n_R} \left(|u_{n_L}u_{n_R}|e^{i\hat{\phi}/2} - |v_{n_L}v_{n_R}|e^{-i\hat{\phi}/2}\right) \gamma_{n_L\sigma}\gamma_{n_R\sigma}^\dagger + H.C.. \quad (2.23)$$

During this tunneling, the quasiparticle carries away the qubit's energy and is scattered into a higher excitation state $E_{k'}$. If the tunneling rate is not too large (i.e., $t \ll 1$), this can be treated as a perturbation on the qubit Hamiltonian H_ϕ , and using the Ambegaokar-Baratoff relation to relate the tunneling matrix element to the normal state resistance of the junction and then the Josephson energy E_j , one can arrive at the following expression of the Fermi golden rule for the transition rate Γ between eigenstates i, f of the Hamiltonian:

$$\Gamma_{i,f} = \frac{16E_j}{\hbar\pi\Delta} \int_{\Delta}^{\infty} dE_k f(E_k, \beta)(1 - f(E_k + \hbar\omega_{i,f}, \beta)) \quad (2.24)$$

$$\times \left[\frac{E_k(E_k + \hbar\omega_{i,f}) + \Delta^2}{\sqrt{E_k^2 - \Delta^2}\sqrt{(E_k + \hbar\omega_{i,f})^2 - \Delta^2}} \left| \langle f | \sin \frac{\phi}{2} | i \rangle \right|^2 + \right. \quad (2.25)$$

$$\left. \frac{E_k(E_k + \hbar\omega_{i,f}) - \Delta^2}{\sqrt{E_k^2 - \Delta^2}\sqrt{(E_k + \hbar\omega_{i,f})^2 - \Delta^2}} \left| \langle f | \cos \frac{\phi}{2} | i \rangle \right|^2 \right]. \quad (2.26)$$

In this expression, the energy $\hbar\omega_{if} = E_i - E_f$ for the initial and final states as usual. The bounds

of integration here start at $E_k = \Delta$ as this is the minimum possible quasiparticle energy from BCS theory (discussed further in §2.2.1). As $E_k \geq \Delta$, the numerator for the cos term is always smaller than the sin term and can be ignored.

At equilibrium, the occupation of the quasiparticle states $f(E_k, \beta)$ will be the usual equilibrium Fermi-functions f_0 , where

$$f_0(E, \beta) = \frac{1}{e^{E\beta} + 1} \equiv \frac{1}{2} \left[1 - \tanh\left(\frac{\beta E}{2}\right) \right], \quad (2.27)$$

with $\beta = 1/k_B T$. As we will consider later, quasiparticles in superconductors can be in non-equilibrium states which may or may not resemble a thermal distribution at all. The fractional density of quasiparticles to Cooper-pairs is proportional to the integral

$$x_{qp} \equiv \frac{n_{qp}}{n_{CP}} = \int_{\Delta}^{\infty} dE_k f(E_k) N(E_k) \equiv \int_{\Delta}^{\infty} dE_k \frac{f(E_k) E_k}{\sqrt{E_k^2 - \Delta^2}}, \quad (2.28)$$

which can be easily identified within the form of Eq. 2.26, such that the relaxation rate of the first excited state is approximately

$$\Gamma_{10} \approx |\langle 1 | \sin(\phi/2) | 0 \rangle|^2 \frac{8E_j}{\hbar\pi} x_{qp} \sqrt{\frac{2\Delta}{\hbar\omega_{10}}}. \quad (2.29)$$

The important takeaway here is that the tunneling of quasiparticles between superconducting islands should be expected to cause uncontrolled energy transfer between the qubit and the excitations of the material, due to the coherence factors associated with quasiparticle tunneling between superconductors with independent phases. Increasing the quasiparticle density near the junction will increase the decoherence rate of the qubit, as will lowering the resistance of the tunnel junction

R^N as this increases the tunneling probability.

At mK temperatures, the thermodynamic expectation of the number of quasiparticles in a typical elemental superconductor in the BCS model is approximately zero, as it is suppressed by a factor $\approx \exp(-\Delta/k_B T)$ [18]. More specifically, one can derive that for a superconducting island of volume V and temperature T , the fractional density of quasiparticles due to thermal excitations is

$$x_{qp} \approx \sqrt{\frac{2\pi k_B T}{\Delta}} e^{-\Delta/k_B T}, \quad (2.30)$$

or alternatively that quasiparticles have an effective “ionization” temperature of

$$k_B T \approx \Delta / \ln(n_{CP} V). \quad (2.31)$$

depending on the system size [23]. Because of the logarithm in the denominator, this will always be a modest fraction of the transition temperature of the superconductor, and so long as the qubit is kept colder than this, zero quasiparticles would be expected at equilibrium. Intuitively, one might say that thermal excitations of quasiparticles from the bath/phonon-system are generally not a source of decoherence for qubit excitations.

However, it is currently well known that a steady state population of quasiparticles does exist in superconducting devices at low temperatures, and that most experiments in this regime are at least somewhat out of equilibrium. In early work on the subject by J. Aumentado *et al.*, unexpectedly large numbers of quasiparticles were observed via $1e$ transitions in charge sensitive devices due to tunneling of quasiparticles off of a superconducting gate electrode [32]. This was later found to agree with measurements of the energy decay rate Γ_{10} of qubits with a density

$n_{qp} \approx 10 \mu\text{m}^{-3}$ consistent with a greatly elevated effective temperature of the quasiparticle distribution of $\approx 140 \text{ mK}$ [17]. Along with energy decay, there is also the issue of parity of the qubit's charge, which flips due to the discrete $\Delta n_g = 0.5$ change that occurs when a quasiparticle tunnels. This not only shifts the energy levels of the qubit (although only slightly in the transmon limit) but causes a dephasing of qubit wavefunctions due to the parity reversal [33]. This too has been experimentally seen in a number of works [34, 35], and large changes in qubit lifetimes have been demonstrated by deliberate photo-excitation of quasiparticles to empirically relate qubit lifetimes to excess quasiparticle densities [36, 37]. As the process of quasiparticle tunneling pumps further energy into the non-equilibrium distribution (in units of $\hbar\omega_{i,f}$), the manner in which the qubit is operated has also been shown to affect the population of quasiparticles in vicinity to the junction [38]. At present, there remains considerable debate on both the origins and dynamics of these quasiparticles, as they appear at high densities yet also seem to have a thermal-like distribution [39, 40], suggesting that their origin may be a confluence of many systematic sources stemming from the cryogenic environment.

2.1.3 Two-Level Systems and Other Defects in Qubits

So far we have considered only interactions in the qubit Hamiltonian which arise due to superconducting quasiparticles, however a second much broader class of issues arise due to microscopic defects in the qubit itself. If we consider a defect to have a single energy level spacing that is close enough to that of the qubit to become resonant, we expect it to exchange energy with the qubit in a coherent manner. As this will be a totally uncontrolled Hilbert space coupled to that of the qubit, this will compromise the fidelity of the qubit itself over time, leading to decoherence. In addition, ensembles of TLSs with transitions far from resonance, typically associated with lossy dielectrics with small energy level splittings, can collectively lead to dispersive interactions with the qubit [41].

Such defects are broadly classified as Two-Level Systems (TLSs), based on the approximation that a given defect probably does not have more than one transition coupled to the qubit frequency (and even if it did, it could not be easily probed). The exact nature of the interaction between a particular TLS and qubit is not universal, and can be classified into roughly three categories [42, 43]: critical current fluctuations coming from defects in the Josephson junction, dipole moments within dielectrics the vicinity of the qubit, and magnetic moments which can lead to flux being threaded through the qubit. We first will introduce potential interaction Hamiltonians based on a review by Zhen-Tao Zhang and Yang Yu [43] for resonantly coupled TLSs, and then consider experimental evidence for these types of TLS in qubits.

For a critical current fluctuation of magnitude δI_c caused by, for instance, the motion of a defect at the junction which changes its area or transparency, one can express the interaction for a single TLS as [44]:

$$H_{I_c} = \frac{\delta I_c \Phi_0}{2\pi} \cos(\phi) \times (\cos \theta \sigma^x + \sin \theta \sigma^z). \quad (2.32)$$

Here, $\sigma^{x,z}$ are Pauli-spin operators for the TLS eigen-basis (i.e. $\sigma^z = \begin{pmatrix} 1 & 0 \\ 0 & -1 \end{pmatrix}$) corresponds to the TLS transition $|1\rangle \leftrightarrow |0\rangle$ and so on). The angle θ defines the coupling type for the defect, which we will see for the other two types of Hamiltonian is a generic property by which TLS are categorized as being “transverse” (coupling to the energy of the qubit via the σ^z term) or “longitudinal” (coupling to the phase of the qubit via the σ^x term) [42]. This coupling is eminently of the form of H_J , and was first identified by observations of Rabi-oscillations of a qubit state as the qubit frequency was tuned by an inductively coupled current $I \lesssim I_c$ across the qubit junction as shown in Fig. 2.2 [44]. More recent work has found these to be rarer than initially presumed, but distinguishable from other TLS sources based more refined measurement schemes [45].

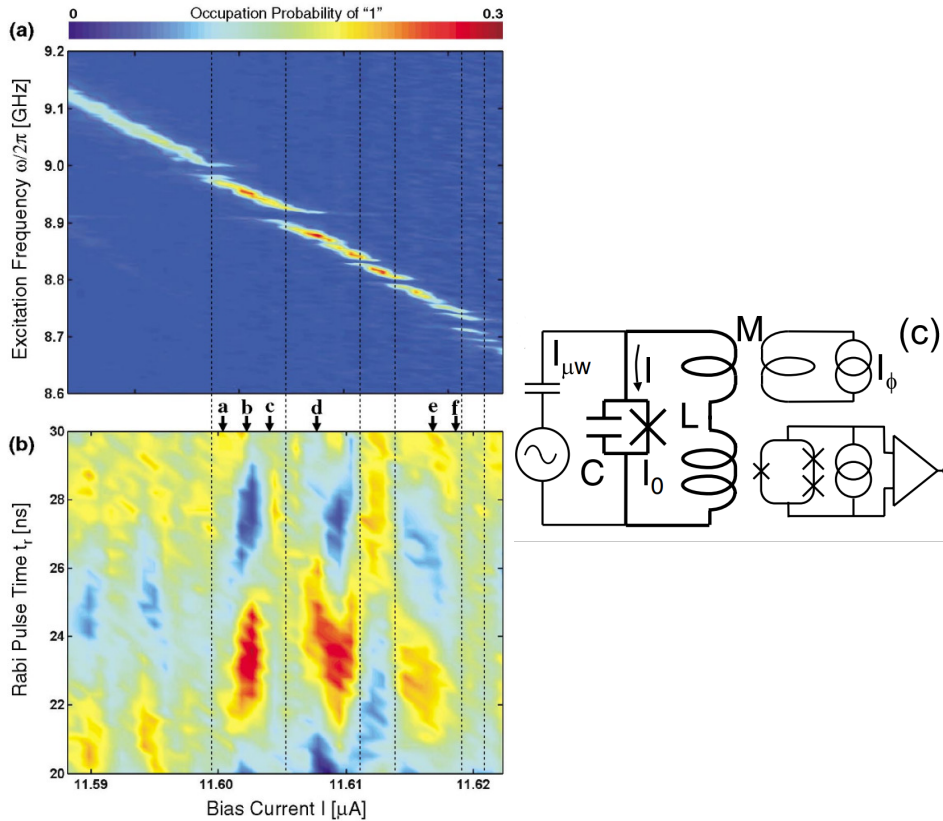


Figure 2.2: Rabi-oscillation between a current biased qubit and individual TLSs, reproduced from Ref. [44]. “(a) Measured probability of state “1” versus microwave excitation frequency $\omega/2\pi$ and bias current I for a fixed microwave power. Data indicate ω_{10} transition frequency. Dotted vertical lines are centered at spurious resonators. (b) Measured occupation probability of $|1\rangle$ versus Rabi-pulse time t_r and bias current I . In (b), a color change from dark blue to red corresponds to a probability change of 0.4. Color modulation in time t_r (vertical direction) indicates Rabi oscillations.” (c) “Circuit diagram for the Josephson junction qubit. Junction current bias I is set by I_ϕ and microwave source I_w . Parameters are $I_0 \approx 11.659 \mu\text{A}$, $C \approx 1.2 \text{ pF}$, $L \approx 168 \text{ pH}$, and $L/M \approx 81$.”

TLSs which interact via an electric dipole take a different form, and have turned out to be the predominant type. Under the assumption that an electric dipole moment $\vec{\mu}$ exists and is oriented at an angle η within the electric field \vec{E} across the Josephson junction (which depends on the oxide thickness t_{Ox} and the charge across the junction \hat{N}), the resulting interaction Hamiltonian could

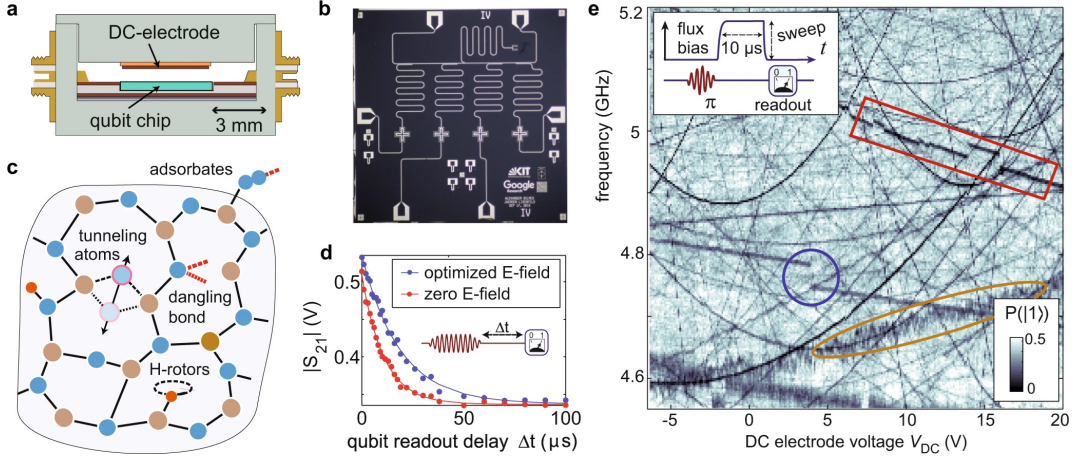


Figure 2.3: Electrostatic gating of TLS defects resonantly coupled to frequency tunable qubits, reproduced from Ref. [46]. “a) Cross-section through the sample housing. The electrode to generate the E-field consists of a Copper-foil/Kapton foil stack glued to the lid of the sample holder above the qubit chip, and voltage-biased against ground. b) Photograph of the XMon qubit samples used in this work. c) Illustration of defects which appear in the amorphous oxides of qubit electrodes. d) Exemplary measurements of the decaying qubit population after a long exciting microwave pulse (see inset) to determine the T_1 time. Red (blue) points were acquired at zero (the optimized) applied E-field. e) Resonances of individual TLS (dark traces), observed as accelerated decay of the qubit’s excited state population (color scale) using the swap-spectroscopy protocol shown in the inset. The circle marks coupling of a TLS to a metastable fluctuator which may cause hysteresis in E-field sweeps. Rectangle and ellipse indicate the fluctuating resonance frequencies of TLS coupled to slowly and quickly fluctuating thermal TLSs, respectively.”

be of the form proposed by J. Martinis [47]:

$$H_{\vec{\mu}} = \vec{\mu} \cdot \vec{E} \equiv 4E_c \frac{\mu \hat{N}}{t_{Ox}.e} \cos(\eta) \times (\cos \theta \sigma^x + \sin \theta \sigma^z), \quad (2.33)$$

which also explained many of the former observations of critical current type TLSs. Note, that this fairly minimal model ignores the additional electric field due to the charge of unpaired electrons n_g across the qubit.

Now, this coupling is in terms of an effective interaction between the number of Cooper pairs

present on the islands, giving it a characteristically different effect on the Hamiltonian. Such defects can also form in the substrate [47], surface oxides [48], or grain boundaries [49] where they will experience different coupling strengths with the qubit. Different types of spectroscopy have been used to identify these as transverse couplings defects, which can also evolve over time due to motion of the defects within the electric field of the qubit [50]. More recent measurements have demonstrated the significant populations of such dipole TLSs via application of mechanical strain [51] or external dc-electric fields [46], which tilt or distort the dipole moments of the TLS populations and thus tune their energy levels in and out of resonance with the qubit. Characteristic results of this latter example are shown in Fig. 2.3, where both the qubit frequency and an external electric field are used to tune the resonance of the qubit with a large ensemble of electric dipole type TLSs. This effect can even be used to help locate them on the qubit itself by understanding the electric field and TLS coupling strength [52, 53].

For magnetic dipoles, a direct coupling between the TLS and the qubit phase is possible. For a fluctuation in flux of the magnitude $\delta\phi$ one can express an interaction Hamiltonian of the form [54]

$$H_L = -\frac{\delta\phi}{L} \left(\frac{\Phi_0}{2\pi} \right)^2 \hat{\phi} \times (\cos \theta \sigma^x + \sin \theta \sigma^z), \quad (2.34)$$

where L is the self inductance of the qubit around which the flux is being threaded. This coupling can be, perhaps unsurprisingly, longitudinal rather than purely transverse causing additional dephasing of the system [54].

Due to the large number and ambiguous nature of the defects possible in the fabrication of these devices, there are naturally many more models possible for describing individual TLSs, some of which do not express simply through an interaction Hamiltonian. An interesting case is that of TLSs which present themselves as fluctuations of the quasiparticle population. In this picture, a

TLS emerges from fluctuations of the local order parameter about

$$\Delta = \Delta_0 + \delta\Delta(\vec{r}) \quad (2.35)$$

which create small regions where quasiparticles are trapped in bound states by the reduced gap [55]. These types of defects are reported on the surfaces of NbN [56], as well as around defects found beneath the surface oxide in Nb [57] via scanning tunneling microscopy, but are relatively less studied than those discussed above. Trapped flux in superconducting films, known to otherwise lead to dissipation within their normal metal vortex cores [58], could also trap quasiparticles and lead to TLS like variations in qubit lifetimes. Even more exotic effects such as quantum jumps in the dynamics of the qubit's interactions with its environment have been considered [59], with some work even seeking to dynamically modify the interactions between the qubit and their TLSs to decouple them stochastically [60].

For the purpose of this thesis, the breadth of these possible TLS couplings serves to illustrate the importance of understanding the material quality of the superconductors used to build qubits. Dirty superconductors, of the type we will explore later on, contain so many defects that it impacts the fundamental properties of the condensate averaged across the entire material. While defects found in the substrate or in tunnel barrier oxides are less likely to contribute to transport properties such as bulk resistivity, those present in grain boundaries or in the native oxides atop of the superconductor can. Film granularity in particular is now thought to be related strongly to the formation of defects causing TLSs [49]. Finally, we can consider quasiparticle trapping on defects as a potential TLS or TLS like mechanism for qubit decoherence, which relates to both the superconducting properties of these film and their non-equilibrium dynamics.

2.2 Non-equilibrium Superconductivity

To better understand the origins and dynamics of non-equilibrium quasiparticles in superconductors in greater detail, in this section we will review the microscopic theories alluded to earlier in §2.1.2 which lead to the quasiparticle description of unpaired electrons. This will underpin the theory required for analysis of tunneling transport experiments described later in Ch. 5, as well as giving us a better understanding of the meanings of pairbreaking and proximity effects in Nb films by defects described in §2.3 and Ch. 4.

2.2.1 The BCS Ground-state and Quasiparticle Excitations

To begin, we will take it as a given that electrons in superconductors are bound to form Cooper-pairs due to the instability of the filled Fermi-sea towards forming a condensate by a small attractive potential between electrons [61]. For conventional superconductors, this attractive interaction is mediated by phonons. This serves to set the upper energy scale for the interaction at the Debye energy of the material, which for elemental superconductors is quite large [62]. Following next the derivations from M. Tinkham [30], we know this pair is a singlet formed of $+k, \uparrow$ and $-k, \downarrow$ electrons

$$|\psi_0\rangle = \sum_{k>k_f} g_k c_{k\uparrow}^\dagger c_{-k\downarrow}^\dagger |F\rangle \quad (2.36)$$

for some weights g_k , based on the state of the ordinarily filled Fermi-sea $|F\rangle$ of occupied electrons, for all wave-vectors k up to k_f . From this, one could build an N -body wavefunction of all of the electrons in the material and use the Slater determinant method to anti-symmetrize the ground state wavefunction appropriately, but this would have innumerable terms. Instead, this can be simplified

by introducing the concept of the BCS coherence factors to form a ground state wavefunction

$$|\psi_G\rangle = \prod_{k=k_1, k_2, \dots, k_M} (u_k + v_k c_{k\uparrow}^\dagger c_{-k\downarrow}^\dagger) |0\rangle \quad (2.37)$$

constructed now from the vacuum state $|0\rangle$. The weights $|v_k|^2$ and $|u_k|^2$ are the probability of the Cooper pair being occupied or not.

We can continue to understand this by expressing the BCS pairing Hamiltonian in terms of electron operators with wave-vectors k and l subject to a pairing interaction V_{kl} :

$$H_{BCS} = \sum_{k,\sigma} \epsilon_k n_{k\sigma} + \sum_{k,l} V_{kl} c_{k\uparrow}^\dagger c_{-k\downarrow}^\dagger c_{-l\downarrow} c_{l\uparrow}. \quad (2.38)$$

This can be diagonalized by introduction of the canonical transformations [29] described earlier in Eq. 2.1.2, which gave us operators $\gamma_{k\uparrow}^\dagger$ which described the creation of a quasiparticle with momentum k and spin up. In introducing this form, one finds that the Hamiltonian will contain a gap in the now diagonalized energy spectra for quasiparticles, derived by tracing out the pairing interactions with respect to the momenta l

$$\Delta_k = - \sum_l V_{kl} \langle c_{-l\downarrow} c_{l\uparrow} \rangle. \quad (2.39)$$

Here, the brackets refer to the mean value, which must be determined self consistently from the wavefunctions of the quasiparticles. As we will see, this is a recurring theme in that the superconducting gap is a self consistently achieved property of the quasiparticle spectra that sets the energy scale for thermodynamic properties of the superconductor and so on. The quantity Δ_k is complex,

and turns out to be related to the coherence factors u_k and v_k by

$$\Delta_k^* \frac{v_k}{u_k} = \sqrt{\xi_k^2 + |\Delta_k|^2} - \xi_k \equiv E_k - \xi_k, \quad (2.40)$$

From this one arrives at the expression used in §2.1.2. This feature also leads to the concept that E_k is an excitation energy, which will later appear as the actual spectral energy involved for the formation of quasiparticles with wave-vector k . If one likes, $|\Delta|$ can be thought of as the rest mass energy of the quasiparticle, with the ξ_k component serving as its kinetic energy in the lab frame, being something like $\hbar^2 k^2 / 2m_e$ depending on the effective mass m_e of the electrons in the system. As an aside, we can take this dispersion relation to give the quasiparticles an energy dependent group velocity, as

$$\frac{dE_k}{dk} = \frac{\xi_k \frac{d\xi_k}{dk}}{E_k} = v_f \frac{\sqrt{E_k^2 - \Delta^2}}{E_k}. \quad (2.41)$$

I.e., the group velocity of the quasiparticles is re-normalized from that of the electrons v_f (the Fermi-velocity), and goes to zero for $E_k = \Delta$. This is a somewhat unique property of the BCS dispersion of quasiparticles which can be easily overlooked, but has been observed experimentally [63].

With this established, the diagonalized Hamiltonian (in the notation of Tinkham) will be

$$H_{BCS} = \sum_k (\xi_k - E_k + \Delta_k \langle c_{-k\downarrow} c_{k\uparrow} \rangle^*) + \sum_k E_k (\gamma_{k0}^\dagger \gamma_{k0} + \gamma_{k1}^\dagger \gamma_{k1}) \quad (2.42)$$

$$\equiv \sum_k \left(\xi_k - E_k + \frac{|\Delta_k|^2}{2E_k} \right) + \sum_k E_k (\gamma_{k0}^\dagger \gamma_{k0} + \gamma_{k1}^\dagger \gamma_{k1}) \quad (2.43)$$

In the last step we have concatenated things to more clearly show the role of the gap Δ_k , by

observing that

$$\Delta_k = - \sum_l V_{kl} u_l^* v_l \langle 1 - \gamma_{l0}^\dagger \gamma_{l0} - \gamma_{l1}^\dagger \gamma_{l1} \rangle \quad (2.44)$$

Note that Tinkham uses the subscripts 0 and 1 to denote the following spin directed quasiparticles

$$\gamma_{k0}^\dagger = u_k^* c_{k\uparrow}^\dagger - v_k^* c_{-k\downarrow}, \quad (2.45)$$

$$\gamma_{k1}^\dagger = u_k^* c_{-k\downarrow}^\dagger + v_k^* c_{k\uparrow}. \quad (2.46)$$

As these are composite fermions with half integer angular momenta, we can generally adopt the notation that $\gamma_{k0}^\dagger \equiv \gamma_{k\uparrow}^\dagger$ and so on as before. In this form, we can clearly see that the creation of a Bogliobov quasiparticle of this type has both an electron and hole like character, denoted by u_k and v_k . As such, the expectation value of the charge of these quasiparticles or quasi-holes is a continuous function of ξ_k ,

$$q/e = |u_k|^2 - |v_k|^2 = \frac{\xi_k}{E_K}, \quad (2.47)$$

which is strictly less than or equal to the $1e$ charge of an electron (or $-1e$ for a hole).

With this, we have arrived at the complete *excitation* description of quasiparticle states, with a dispersion relation E_k shown in Fig. 2.4. One must be careful to note that, from now on, we will mostly be referring to the *particle* description based on E_k . This choice is somewhat subtle, as in the excitation description E_k is always positive in energy while ξ_k extends to positive and negative energies (about the Fermi surface), but in the discussion to follow the particle picture permits negative values of E_k which form as a filled Fermi sea. This tends to be more useful in

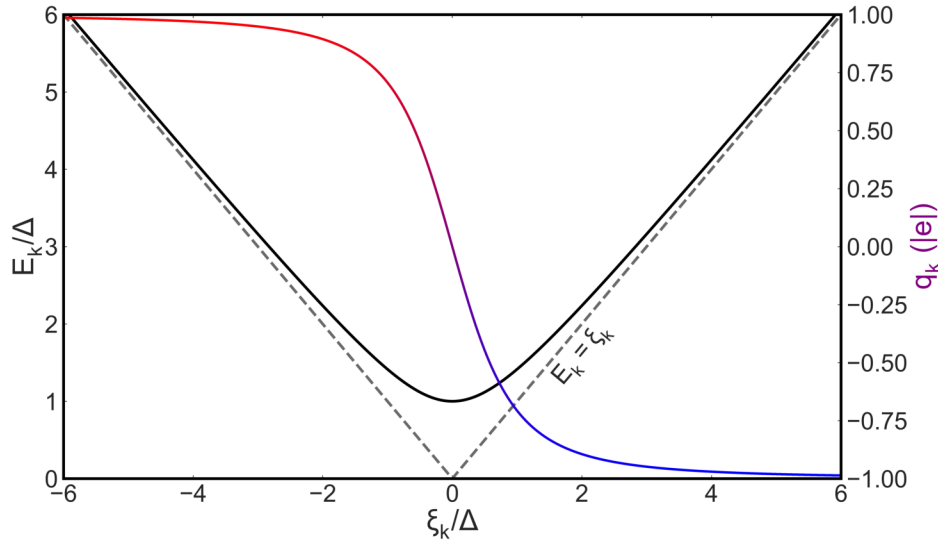


Figure 2.4: Left axis: Relationship between the single particle and excitation energies ξ_k and E_k which yield the BCS dispersion relationship for quasiparticles. Right axis: the corresponding quasiparticle charge of the excitation for a given ξ_k . The color map indicates the range between the full electron charge (negative, blue) and full hole charge (positive, red).

practice as most experiments excite quasiparticles with a definite value E_k . When necessary, we will refer to one or the other description going forward.

On a final note, the notion of how “real” the quasi-charge is on the basis of describing individual quasiparticles as having a definite observable charge is somewhat mixed. As we discussed earlier, *tunneling* of individual quasiparticles between superconductors actually corresponds to the manipulation of superpositions of electrons and Cooper-pairs. When a quasiparticle tunnels to/from a charged superconducting island, the corresponding operators found in the expansion of Eq. 2.20 are always associated with an exchange of $\pm 1e$ of charge, and thus one does not observe charge jumps corresponding to this partial quasiparticle charge (it is of course always possible to induce a continuous polarization charge via electrostatic fields, which is not a property of the quasiparticles directly). As a result there has been some discussion about whether or not the quasiparticle charge is actually carried by the condensate instead. For instance, it is claimed that Coulomb interactions

lead to neutral, spin-half particles regardless of energy, causing a so called ‘spin-charge decoupling’ of the system where quasiparticles only participate in spin and heat flow [64, 65, 66]. This is distinct from the effect which is sometimes invoked in discussion of spin-currents of *de facto* charge neutral Bogliobov quasiparticles at $\xi_k = 0$, where spintronic applications have been considered extensively [67, 68, 69]. The essence of the former concept is that actually constructing a wave-packet for quasiparticles is nontrivial due to the expected screening of the condensate [66]. There are few experimental probes of the charge of an individual quasiparticle which might settle these debates. One work by Y. Ronen et al. in 2016 used a proximity effect nanowire to form a Josephson Junction in which a bound state was formed with a conductance determined by the energy dependence of the quasiparticle charge [70]. Their findings agreed well with the continuous charge of quasiparticles described by simple BCS theory. However attempts to perform Aharonov-Bohm type interference experiments using quasiparticles, which should be sensitive to the quasiparticle charge as it interacts with the a vector potential, have so far been inconclusive in both their results [71, 72] and their interpretations [73]. These have not shown much evidence of partial charge, and are instead dominated by $2e$ signals. Nevertheless, for this thesis we will continue to take the BCS approach for understanding transport experiments involving the quasiparticle charge.

2.2.2 Quasiparticles at Finite Temperature

As quasiparticle excitations will serve as the basis for the experiments to come, we need to first understand their spectrum and equilibrium description. Because of the correspondence between the density of electrons N_n and of quasiparticles N_s , the total number of states will be equal such

that, in the excitation description, we will have

$$N_s(E_k)dE_k = N_n(\xi_k)d\xi_k \quad \Rightarrow \quad \frac{N_s(E)}{N_0} = \frac{d\xi_k}{dE_k} \quad (2.48)$$

$$\Rightarrow \quad N_s(E_k) = N_0 \times \begin{cases} \frac{E_k}{\sqrt{E_k^2 - \Delta^2}} & (E \geq \Delta) \\ 0 & (E < \Delta) \end{cases} \quad (2.49)$$

In this notation N_s is the superconducting density of states for quasiparticles, and N_0 is the ordinary (spectral) density of states for the electrons at the Fermi energy. The divergence in the superconducting density of states occurs for $\xi_k = 0$ quasiparticles at the gap edge, where the particles have equal electron and hole components giving them zero charge, and is thus for all intents and purposes, infinite.

We can represent this pictorially as shown in Fig. 2.5, now in the particle description where E_k can be either positive or negative. The density of states for quasiparticles is equal to that of the normal state electrons far away from the gap, but near the gap edge the density becomes quite high. The positive and negative energy states can be seen to have opposite electron and hole components, but at $E_k = \pm\Delta$ they have equal values. As we will discuss in §2.2.4 it is useful to make the analogy to semiconductors, where 2Δ takes the place of the bandgap between valence and conduction electrons. For this reason, Tinkham defines an additional set of “quasi-electron” and “quasi-hole” creation operators γ_e^\dagger and γ_h^\dagger , where γ_e^\dagger works just as defined before, and $\gamma_h^\dagger = S\gamma_e^\dagger$ to account for the difference between the two bands. This essentially gives two copies of the excitation description to worry about. Care must be taken to not stretch this analogy too far, as states at $E_k = \pm\Delta$ are still indistinguishable and can be in either momentum or spin state.

To build the model up slightly more for use in later calculations and fits in this thesis, we must

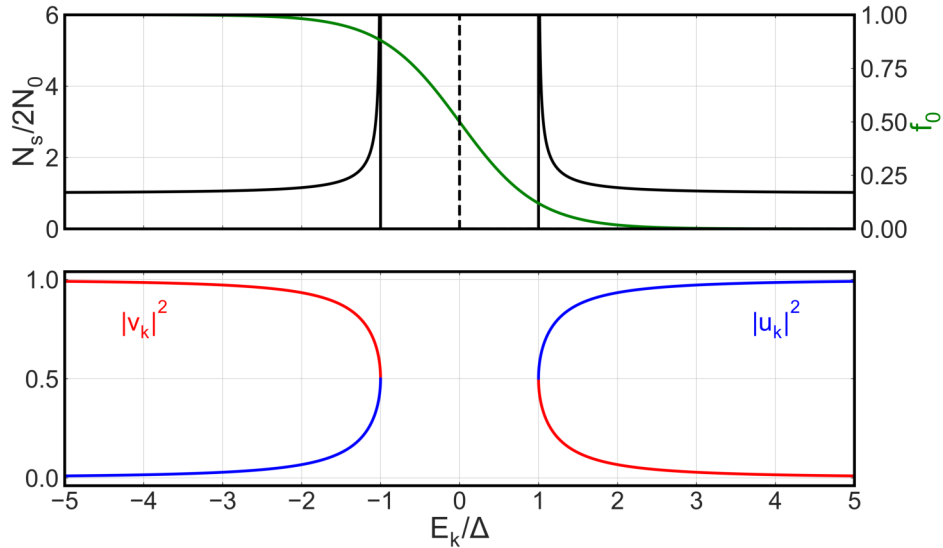


Figure 2.5: Top Panel: Relative density of states (black) and equilibrium occupation probability f_0 (green) for the case where $k_B T \approx \Delta_0/2$. Bottom Panel: Magnitudes u_k^2 (blue) and v_k^2 (red) representing the electron and hole components of the quasiparticle at an energy E_k . All axes are dimensionless.

briefly also remark that the singularities at $E_k = \Delta$ pose a challenge for numerical methods. Similarly, inhomogeneity in materials or experimental factors can cause broadening, making it a practical issue to observe this divergence in measurements. To account for this, a pair-breaking parameter must be introduced in some forms. The simplest choice, and the one used for later calculations and fitting, is to take a density of states of the type used by Meservey and Tedrow [74], where the energy includes a negative complex component

$$N_s = 2N_0 \mathbf{Re} \left[\frac{E_k - i\Gamma}{\sqrt{(E_k - i\Gamma)^2 - \Delta^2}} \right]. \quad (2.50)$$

Conceptually this is sometimes considered an actual parameter accounting for a finite quasiparticle lifetime, as was done by Dynes [75] (as such, this factor is colloquially known as the Dynes Γ). For a Dynes $\Gamma \ll \Delta$, this choice has the effect of both broadening N_s and lifting the condition on

energies $E_k < \Delta$ by approximately $2N_0\Gamma/\Delta$, as shown in Fig. 2.6. As this is not of fundamental significance, we will ignore the microscopic implications of this term going forward, and use it as necessary in calculations.

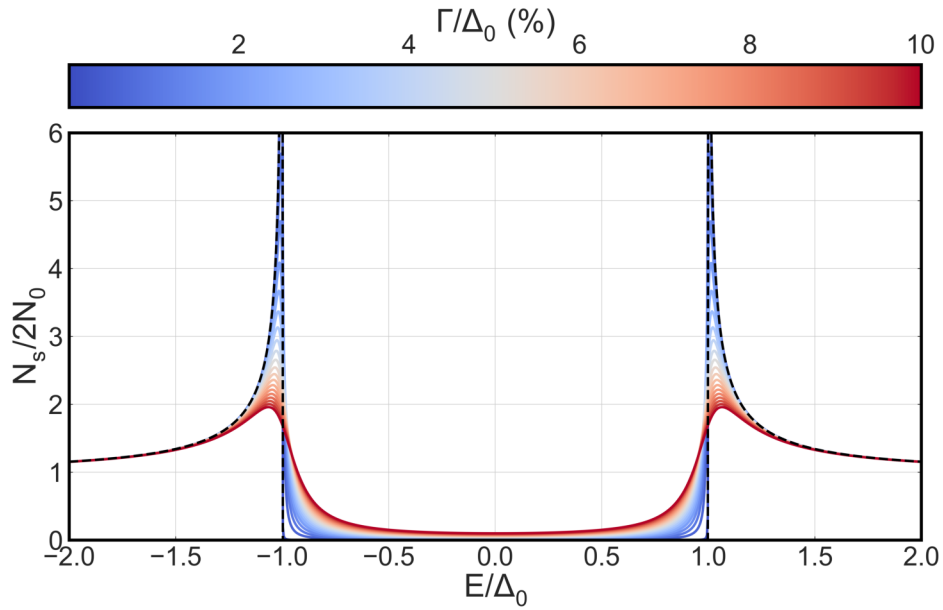


Figure 2.6: Quasiparticle density of states N_s for a superconductor with a finite pair lifetime introduced by a small Γ term. The black curve indicates the BCS calculated value where $\Gamma \rightarrow 0$.

Assuming that quasiparticles follow a thermal spectrum at equilibrium, governed by that of the bath/phonon temperature of the system, then they should obey a Fermi distribution as

$$f_0 = \frac{1}{1 + e^{(E_k - \mu)/k_B T}} \equiv \frac{1}{2} \left[1 - \tanh \left(\frac{E_k - \mu}{k_B T} \right) \right] \quad (2.51)$$

where μ is the chemical potential of the metal, which will become either applied voltage or Fermi energy depending on what we want to consider. This is shown schematically in Fig. 2.5, for a fairly high temperature where the tails of the distribution significantly overlap with the peaks in the density of states. This again lends to the semiconductor description well, as one can intuitively

picture unoccupied quasi-electrons states for $E_k \ll 0$ (or occupied positive quasi-holes) and occupied states for $E_k \gg 0$. At more realistic temperatures, this would simply appear as a step function about $E_k = 0$ on this scale.

Using this, we can now calculate the self consistent value of the gap, as we can set

$$\langle 1 - \gamma_{k0}^\dagger \gamma_{k0} - \gamma_{k1}^\dagger \gamma_{k1} \rangle \equiv 1 - 2f_0(E_k). \quad (2.52)$$

This gives the summation form of the BCS self consistency equation

$$\Delta_k = - \sum_l V_{kl} \frac{\Delta_l}{2E_k} (1 - 2f_0(E_l)) \equiv - \sum_l V_{kl} \frac{\Delta_l}{2E_k} \tanh\left(\frac{E_l}{k_B T}\right). \quad (2.53)$$

Which for $V_{kl} \rightarrow V$ can be converted to the more familiar form of an integral expression

$$\frac{1}{N_0 V} = \int_0^{\hbar\omega_D} \frac{1 - 2f_0(E_k, T)}{\sqrt{\xi_k^2 + \Delta^2}} d\xi_k \equiv \int_0^{\hbar\omega_D} \frac{\tanh(\sqrt{\xi_k^2 + \Delta^2}/(2k_B T))}{\sqrt{\xi_k^2 + \Delta^2}} d\xi_k. \quad (2.54)$$

The upper limit of integration is not particularly important as the integrand is primarily weighted very close to zero, and in various texts is taken either as an arbitrary value or as the Debye frequency ω_D (the frequency of the highest available phonons). At zero temperature, the numerator of this integrand goes to unity and evaluations yields that $(N_0 V)^{-1} = \sinh^{-1}(\hbar\omega_D/\Delta_0)$ where Δ_0 is the zero temperature BCS gap magnitude (i.e. the total absence of quasiparticles). The quantity $N_0 V \equiv \lambda_{BCS} < 1$ defines what is generally called the weak coupling limit in the BCS theory. Taking the other limit where $\Delta \rightarrow 0$, there will not be a closed form solution, but as $\hbar\omega_D$ is large it has an approximation involving constants (including Eulers constant $\gamma = .5772\dots$). Relating everything together we get the precise relationship between the BCS coupling constant, the zero

temperature gap and the transition temperature

$$\int_0^{\hbar\omega_D} \frac{\tanh(\xi_k/(2k_B T))}{\xi_k} d\xi_k \approx \ln\left(\frac{2e^\gamma}{\pi} \frac{\hbar\omega_D}{k_B T_c}\right) \Leftrightarrow \frac{1}{N_0 V} \Leftrightarrow \sinh^{-1}(\hbar\omega_D/\Delta_0). \quad (2.55)$$

Linearizing these expressions to first order in $\hbar\omega_D$, under the assumption that $N_0 V \ll 1$, and taking the ratio gives the well known estimate that $\Delta_0 = 1.764k_B T_c$, but the precise ratio depends on the value of the BCS coupling strength [76]. Taking this ratio as a given, the expression can be used to model the equilibrium temperature dependence of a weak coupling BCS superconductor $\Delta(T)$, by recasting these equations as a minimization problem for the function

$$F(T, \Delta) = -\sinh^{-1}(\hbar\omega_D/\Delta_0) + \int_0^{\hbar\omega_D} \frac{\tanh(\sqrt{\xi_k^2 + \Delta^2}/(2k_B T))}{\sqrt{\xi_k^2 + \Delta^2}} d\xi_k \quad (2.56)$$

Given the highly non-linear integral expression, this can only really be done numerically, and in doing so one typically finds that the exact ratio used for $\hbar\omega_D/k_B T_c$ to be almost immaterial to the solution obtained. Taking the example of Al, and using a $T_c = 1.2\text{ K}$ and $\hbar\omega_D = k_B \theta_D = k_B \times 428\text{ K}$ as an example, we plot this in Fig. 2.7.

Quasiparticle excitations will naturally occur by pair-breaking due to thermal phonons (or recombination and the emission of a-thermal phonons with $\hbar\omega = 2\Delta$) until their equilibrium population reaches $f_0(E_k, T)$, however at mK temperatures the width of this distribution is much smaller than $\Delta(T)$ when $T \ll T_c$, and thus few actual quasiparticles will be expected away from the transition. The excitation probability, and thus the density of quasiparticles will go as $\exp(-\Delta(T)/k_B T)$ which can be extremely small for mK temperatures. The rapid drop of this exponential factor is shown on the right axis of Fig. 2.7, which serves to explain the previous assertions that quasiparticles are not expected to exist at all in superconducting qubits. The precise magnitude of the

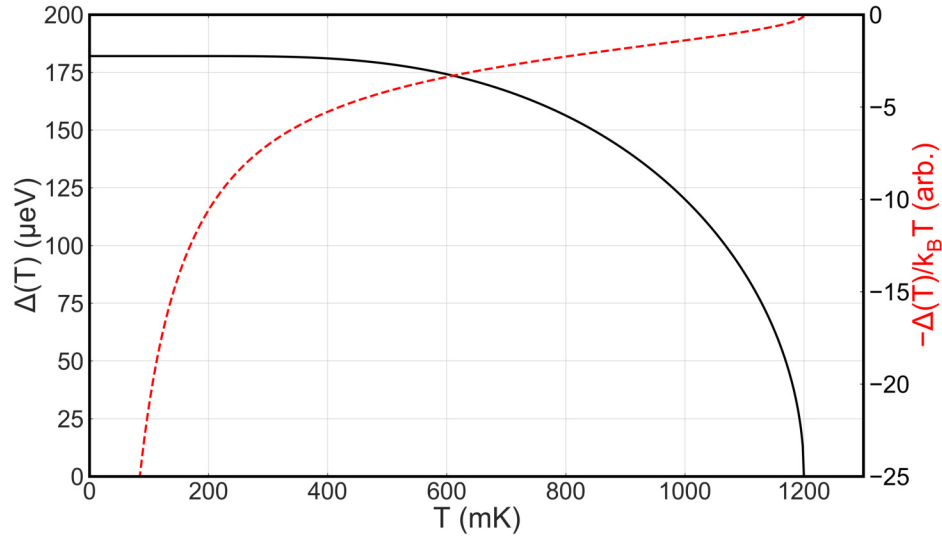


Figure 2.7: Left axis: BCS prediction for the temperature dependent gap of Al, assuming that $T_c = 1.2$ K and $\theta_D = 428$ K [76], and that $\Delta_0 = 1.764k_B T_c$. Right axis: The exponential factor related to the probability of thermal excitations of quasiparticles above the temperature dependent gap of Al. A large negative value indicates an exponentially small probability of quasiparticle excitation at a given temperature.

gap is also not particularly significant compared to the general bath temperature for most qubits of around 10 mK, so long as the superconductor remains well gapped.

2.2.2.1 Quasiparticle Excitation from Athermal Sources

The fact that quasiparticles are seen in superconducting qubits and other experiments at low temperatures thus points to an a different source of pair-breaking, mostly likely some form of radiation. Quasiparticles can be excited by photons or phonons with $\hbar\omega \geq 2\Delta$, which cause pairbreaking and the formation of quasiparticles with opposite values of ξ_k . The momentum q of the incident boson will be transferred in approximately opposite amounts to oppositely charged quasiparticles to put them into these energy states. This is explored diagrammatically in more modern works on superfluids [77], but is taken as an assumption here as we know that the original Cooper-pair is

constructed of opposite momentum quasiparticles. This process maintains charge conservation of the condensate, and recombination of that pair will then release a phonon/photon back to the bath. The electron-phonon coupling in superconducting materials is usually such that phonons mediate this recombination into pairs [78]. Further, as generally superconducting devices are constructed onto large substrates, its typically more likely that phonons participate in pair-breaking than other sources of radiation, at least via direct interactions with the superconductor.

Many recent experiments have hunted for potential sources of pair-breaking radiation, such as infrared-light leaks, resonant coupling to microwave signals [79, 80, 81, 82], stress induced phonon bursts [83], or cosmic radiation [84]. These types of extrinsic sources are a major concern, as sources like cosmic rays can extend to energies above 100 keV, which will be deposited into many phonons which spread throughout the substrate generating quasiparticles [85]. This would then lead to correlated errors across a device which cannot be mitigated via improved circuit design or by quantum error correction [86].

There is also the possibility of pair-breaking due to magnetic defects [87, 88] or by non-magnetic defects in the presence of intrinsic gap-anisotropy [89, 90, 91]. This is source is more of the type considered earlier in the Dynes model discussed in §2.2.1.

2.2.3 Quasiparticle Non-equilibrium

At thermal equilibrium, we have seen that quasiparticles are populated following a Fermi distribution set by the temperature of the phonons, where electron- and hole-like quasiparticles are generated above the gap in equal quantities at high temperatures. Experimentally, we also now understand that this is not the case in many devices, such that we must consider the non-equilibrium behavior of this distribution. A conceptual this can be formed by considering general deviations

of the distribution function f_k from the equilibrium distribution f_0 by their symmetry with respect to E_k , as was originally done in works by J. Clarke and M. Tinkham [92, 93], C.J. Pethick and H. Smith [31]. We can define the deviation from the equilibrium distribution as simply

$$\delta f_k = f_k - f_0(E_k/k_B T) \quad (2.57)$$

such that δf_k quantifies only the non-equilibrium component [30]. Based on the symmetry of δf_k with respect to the quasiparticle *excitation* energy E_k , there are two general cases.

The first, is that δf_k is totally anti-symmetric with respect to E_k , yielding an equal excess/shortage of both quasiparticles and quasi-holes. This follows from the particle description, as the probability $f_0(E_k)$ for energies $E_k > 0$ corresponds to the excitation of quasiparticles, and thus that $1 - f_0(E_k)$ for $E_k < 0$ corresponds to the probability of excitation of quasi-holes, and thus an anti-symmetric $\delta f_k(E_k)$ leads to equal contributions in both branches. This is the basis of energy-mode non-equilibrium, called so as the resulting quasiparticles have the same symmetry as a thermal distribution. The second case occurs when δf_k is symmetric, and thus an imbalance between the populated quasiparticles of opposite charge occurs. This charge-mode imbalance gives the quasiparticle distribution a net charge and allows for charge current flow due to quasiparticles and pairs in the system. This motivates the ‘‘Two Fluid Model’’, which explains charge (and heat) transport of superconductors is coming from two, weakly interacting contributions. Often, the energy mode-case can be simplified as a change in the effective temperature of the distribution f_k such that $T \rightarrow T^*$, and the charge mode as a change in the chemical potential $\mu = 0 \rightarrow \mu_{Q^*}$.

To see this, we can first consider the consequences of non-equilibrium on the self consistency condition for the gap from Eq. 2.2.2. As the gap depends on the non-equilibrium distribution, it is natural to expect a deviation $\Delta \rightarrow \Delta_0 - \delta\Delta$ due to a non-equilibrium contribution δf_k , which

Pethick and Smith derive [31] to be:

$$\delta\Delta \sum_k \frac{\partial}{\partial\Delta} \left[\frac{1 - 2f_0(E_k/k_B T)}{2E_k} \right] = \sum_k \frac{\delta f_k}{E_k}. \quad (2.58)$$

Assuming that $\delta f_k \neq 0$, when summing over all values E_k the righthand side of this expression is finite only if δf_k is anti-symmetric with respect to E_k .

At sufficiently low temperatures, the gap variation of E_k is such that

$$\delta\Delta \approx -\frac{\sum_k (\Delta/E_k) \delta f_k}{N_0}. \quad (2.59)$$

Perhaps unsurprisingly, $\delta\Delta$ must still be found self-consistently from Δ . As $|E_k|$ is always at least Δ , the largest reductions in Δ occurs via quasiparticles at or very near the gap edge, where the density of states is also very high. One can further describe this in terms of the effective temperature T^* of an equilibrium distribution which yields the same magnitude of Δ , being

$$\frac{T^*}{T} \approx \frac{1}{N_0} \sum_k \frac{\delta f_k}{E_k} = \int \frac{\delta f_k}{E_k} d\xi_k. \quad (2.60)$$

This is considered a valid approach so far as the deviation from equilibrium is sufficiently small, as is typically the case near T_c where many quasiparticles are present. It is not hard to come up with circumstances where this would fail, such as in cases where the gap is enhanced *above* its equilibrium value by removing quasiparticles such that $\sum \delta f_k/E_k$ is negative, which can happen in some experiments [94].

Next we consider the charge imbalance, which shifts the chemical potential of the distribution. To

see this, one can define a quantity Q^* to be the total charge carried by the quasiparticles

$$Q^* \equiv 2N_0 \int_{-\infty}^{\infty} q_k(\xi_k) f_k(\xi_k) d\xi_k \equiv 2N_0 \int_{-\infty}^{\infty} \frac{\xi_k}{E_k} \delta f_k d\xi_k. \quad (2.61)$$

At equilibrium this is zero, based on the prior arguments, and by charge neutrality, a finite Q^* implies that the charge of the condensate must be reduced, leading to fewer pairs. Thus, a change in Q^* can be associated with a shift in the chemical potential between the quasiparticles and the condensate by an amount.

$$\mu_{Q^*} = -\frac{Q^*}{2eN_0}. \quad (2.62)$$

This is again under the assumption that the distribution is not driven too far out of equilibrium.

Putting this together, the energy and charge modes can be loosely related to an equivalent non-equilibrium *thermal* distribution function

$$f^*(E_k, \mu_{Q^*}, T^*) = \frac{1}{2} \left[1 - \tanh \left(\frac{\sqrt{\xi_k^2 + \Delta(T^*)} - \mu_{Q^*}}{k_B T^*} \right) \right]. \quad (2.63)$$

This should be taken as a sort of lowest order model for a non-equilibrium superconductor, with the assumptions that go into being mostly reasonable near $T \lesssim T_c$ such that a highly non-equilibrium *a-thermal* distribution f_k relaxes to a non-equilibrium *thermal* distribution f^* fairly quickly. At mK temperatures relevant for more modern work on the topic, this will turn out to be a poor approximation.

2.2.4 Quasiparticle Tunneling from a Normal Metal

Next we explain how these types of non-equilibrium distributions can be generated and observed via tunneling. Many of the original measurements of quasiparticle non-equilibrium, and the experiments we will discuss in this thesis, use a tunneling current of electrons to generate energy and charge imbalance within a superconductor. This occurs as the electrons transfer charge to the quasiparticles and the condensate, and in doing so probe the actual non-equilibrium distribution of quasiparticles. Construction of a Normal-metal/insulator/superconductor (NIS) junction, allows for only tunneling of quasiparticles in combinations which add or subtract a single electron at a time, allowing for such a spectroscopic examination. For our purposes, we will take this normal metal to be a “reservoir”, such that it is always at thermal equilibrium and all current therein is carried by electrons (or equivalently “normal-state quasiparticles” where $\Delta = 0$ such that $\xi_k = E_k$, although this nomenclature is often more confusing). In general, this approximation only holds for sufficiently low transparency interfaces, and can fail completely for clean NS contacts often used in mesoscopic transport [95].

We first consider the case for the (conventional) current I across an NIS junction subject to a voltage bias V , which we find by Fermi’s golden rule [74]:

$$I = \int dE_k |M|^2 \left[N_n(E_k - eV) N_s(E_k) f_n(E_k - eV) [1 - f_k(E_k)] \right] \quad (2.64)$$

$$- N_n(E_k - eV) N_s(E_k) [1 - f_n(E_k - eV)] f_k(E_k) \right]. \quad (2.65)$$

Here N_n is the density of states in the normal metal, which for simple cases such as Cu etc. will be taken as a constant N_{n0} over the range of energies we are considering (several Δ about the Fermi energy), and f_n the equilibrium distribution function of the normal metal. N_s is the

superconducting density of states, and f_k will be the non-equilibrium distribution function in the superconductor. Finally, $|M|^2$ is the magnitude of the tunneling matrix element determining the overall rate of charge transfer, which we also take to be independent of energy. Under these assumptions, this reduces to

$$I = |M|^2 N_{n0} \int_{-\infty}^{\infty} N_s(E_k) \left[f_n(E_k - eV) - f_k(E_k) \right] dE_k. \quad (2.66)$$

Note that now E_k is defined to run freely over all energies, as we will be using the particle description for the majority of such calculations. Taking again the fully equilibrium case where both metals are described by f_0 , it becomes convenient to instead express the differential conductance of this junction as

$$\frac{dI}{dV} = |M|^2 N_{n0} \int N_s(E_k) \left[\frac{df_0(E_k - eV)}{dV} - f_0(E_k) \right] dE_k \quad (2.67)$$

$$\equiv \frac{G_N}{N_0} \int \frac{N_s(E_k)}{k_B T} \frac{e^{(E_k - eV)/k_B T}}{(1 + e^{(E_k - eV)/k_B T})^2} dE_k. \quad (2.68)$$

The integrand here is the product of the ordinary superconducting density of states and a temperature dependent function which is peaked about $E_k = eV$ when $k_B T \ll \Delta$. At $T = 0$, this becomes a δ -distribution, such that

$$G(V) = G_N \int N_s(E_k) \frac{\delta(E_k - eV)}{N_0} dE_k = G_N \times \frac{N_s(eV)}{N_0} \quad (2.69)$$

and thus the conductance of the tunnel junction exactly traces out the superconducting density of states. As one sweeps the bias voltage, the singularity in the density of states leads to a discontinuity in the current as electrons above the gap edge begin to flow. At finite temperature, the equilibrium conductance is broadened, and takes on a temperature dependent coherence peak at

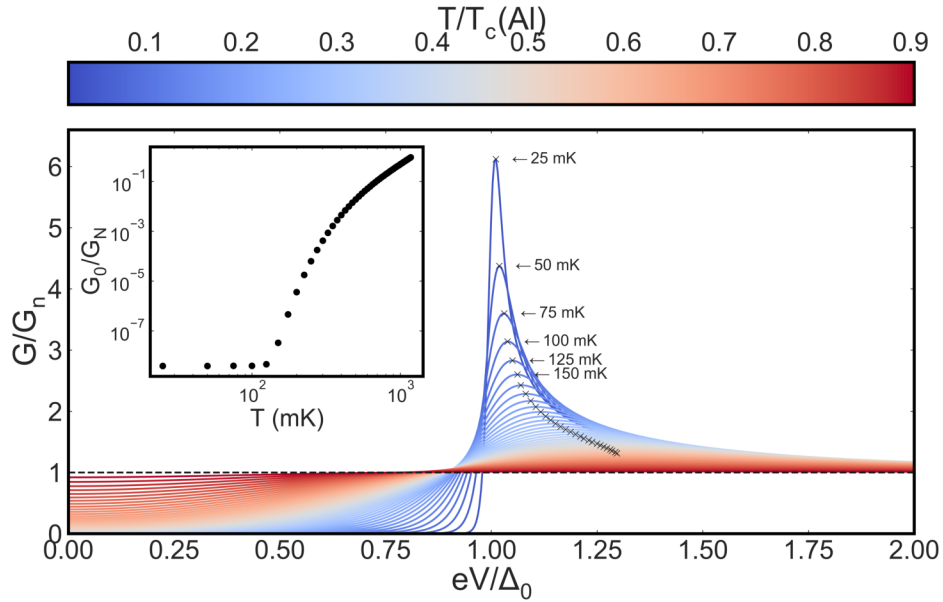


Figure 2.8: Normalized conductance spectra calculated for an Al based NIS tunnel junction as a function of voltage from Eq. 2.68 at various temperatures. $T_c = 1.2$ K and $\Delta_0 = 1.764k_B T_c$, with $\Delta(T)$ calculated as in Fig. 2.7. N_s is determined via a Dynes type fit, but for $\Gamma = 1 \times 10^{-6}$ μeV to approximate the BCS result. Black 'x' markers indicate the position of the coherence peak maxima for a subset of the temperature range. For reference, the lowest few temperatures are indicated to highlight the strong temperature dependence of the coherence peak height/position at mK temperatures. The inset panel shows the zero bias conductance $G_0 = dI/dV|_{V=0}$ as a function of temperature on a log-log scale. The saturation is the result of the small finite Γ term used for calculation, which does not effect the shape/location of the coherence peak maxima.

an energy just above $eV = \Delta(T = 0)$. The conductance below the gap edge is exponentially diminished at zero temperature as the Fermi distributions sharpen. We show this via calculations of conductance spectra using typical parameters for an Al based device in Fig. 2.8. This strong temperature sensitivity for NIS tunneling is one mechanism for experiments in high precision mK range thermometry [96, 97].

By tunneling electrons into a superconductor, non-equilibrium quasiparticles are naturally excited. However, as the operators determining the quasiparticle charge are energy dependent, a natural question arises as to where the electron's charge actually ends up. This problem was originally

Probability	Electrons Added	Excitations Added	Quasiparticle Charge Added	Condensate Charge Added
$ u_k ^2(1 - f_k)f_n(E_k - eV)$	1	1	q_k	$1 - q_k$
$ v_k ^2f_k[1 - f_n(E_k + eV)]$	1	-1	$-q_k$	$1 + q_k$
$ u_k ^2f_k[1 - f_n(E_k - eV)]$	-1	-1	$-q_k$	$-1 + q_k$
$ v_k ^2(1 - f_k)f_n(E_k + eV)$	-1	1	q_k	$-1 - q_k$

Table 2.1: Reproduced from Ref. [31]. Probability and possible outcomes due to electron tunneling across an NIS junction.

considered by Tinkham [98]. In this work, the process of tunneling an electron in our out is broken into two cases with energy dependent probabilities related to the coherence factors and the non-equilibrium distribution of quasiparticles in the superconductor, as outlined in Tab. 2.1. Generally speaking when $|u_k|^2 = |v_k|^2$ at the gap edge, tunneling electrons excites quasiparticles but transfers the full charge to the condensate, and the opposite occurs at the limit where $|E_k| \gg \Delta$. Using these probabilities, we can follow again the work of Pethick and Smith to account for evolution of the distribution f_k due to tunneling as

$$\left(\frac{df_k}{dt}\right)_{tun.} = \frac{2\pi}{\hbar}|M|^2N_{n0} \left[|u_k|^2(1 - f_k)f_n(E_k - eV) - |v_k|^2f_k(1 - f_n(E_k + eV)) \right] \quad (2.70)$$

$$+ |v_k|^2(1 - f_k)f_n(E_k + eV - |u_k|^2f_k(1 - f_n(E_k - eV))), \quad (2.71)$$

which can then be broken down into three contributions as

$$\left(\frac{df_k}{dt}\right)_{tun.} = \frac{2\pi}{\hbar}|M|^2N_{n0} \left[\frac{1}{2} \left((f_n(E_k + eV) + f_n(E_k - eV)) - 2f_n(E_k) \right) \right] \quad (2.72)$$

$$+ \frac{1}{2} \frac{q_k}{e} \left(f_n(E_k - eV) - f_n(E_k + eV) \right) - \delta f_k \Big]. \quad (2.73)$$

In this form, one again sees that df_k/dt evolves via components which are symmetric and antisymmetric in the applied voltage, as quasiparticles are transferred into energy states associated with the

distribution f_n of the normal metal. I.e., both the energy and charge modes are excited depending on the bias. The additional third term is associated with the loss of any existing non-equilibrium part of the distribution δf_k back out into the normal metal lead via tunneling. Considering the charge term, we can find that

$$\frac{dQ^*}{dt} = \sum_k \frac{q_k}{e} \left(\frac{df_k}{dt} \right)_{tun.} \quad (2.74)$$

$$= \frac{2\pi}{\hbar} |M|^2 N_{n0} \left[\frac{1}{2} \frac{q_k^2}{e} \left(f_n(E_k - eV) - f_n(E_k + eV) \right) - \sum_k \frac{q_k}{e} \delta f_k \right]. \quad (2.75)$$

Here, the summation over k has led us to pick out the parts associated with charge imbalance, and thus we are accounting for the net tunneling current associated with changes in Q^* . If we fix $|eV| \ll \Delta$ (for instance, by grounding that side of the device) only the anti-symmetric component of the non-equilibrium distribution contributes to the tunneling current as

$$\frac{dQ^*}{dt} \equiv I_{Q^*} = -\frac{2\pi}{\hbar} |M|^2 N_{n0} \sum_k \frac{q_k}{e} \delta f_k \quad (2.76)$$

$$= \frac{G_N}{2eN_0} Q^* \equiv G_N \times \mu_{Q^*}. \quad (2.77)$$

In this way, the NIS junction naturally allows charge imbalance to relax across the tunnel barrier by returning charge to the normal metal where it is carried away as a current. Knowing this, one can immediately see that NIS junctions are extremely useful for both generating non-equilibrium distributions, as well as detecting non-equilibrium charge imbalance.

2.2.5 Quasiparticle Transport in Superconductors

As we have seen, non-equilibrium excitations of superconductors can be discussed in terms of distinct imbalance modes. This allows us to begin to decompose these distributions and their ob-

servable consequences, and in doing so study how they return to equilibrium via relaxation of quasiparticles. Excited quasiparticles will tend to relax via inelastic collisions, thereby losing their quasi-charge and moving back towards a thermal distribution. At the same time, they also diffuse, and thus an excited non-equilibrium state must extend throughout the superconductor over time. By making measurements using different tunneling junctions spatially separated across a superconductor, most of the original experiments on this topic essentially relate the proportion of remaining charge or energy imbalance to the injected current, and estimate the lifetime of the relevant quasiparticle imbalance mode [99, 100, 92, 93, 98, 101, 102, 103]. In these early experiments, the largest quasiparticle imbalance signals are observed near T_c where the relaxation is slow and more quasiparticles are generally present. At those temperatures, electron-phonon interactions are responsible both for pairing and for inelastic relaxation of quasiparticles when $E_k \gg \Delta$ [78], and much of the topic is dominated by this description. Intuitively this behavior just below T_c is expected, as when $T \rightarrow T_c$ there is no longer a condensate into which the quasiparticles can relax.

As these interactions (and the dispersion of quasiparticles and so on) are all highly energy dependent, interpretation of those experiment required development of theories which could predict the length scale over which relevant observables would be relaxed. In early works, this was handled via Boltzmann transport equations which describe the flow/lifetime of the charge and energy mode distribution functions [31]. Considering the derivation of Pethick and Smith, we have already seen that a source term due to NIS tunneling can be expressed for $(df_k/dt)_{inj}$, which at steady state must be equal and opposite for a collision term by which quasiparticles are moved to lower energy

states and relaxed, giving us

$$\left(\frac{df_k}{dt}\right)_{inj} = -\left(\frac{df_k}{dt}\right)_{coll}. \quad (2.78)$$

In their analysis, this collision term is accounted for by terms responsible for scattering and recombination by phonons, which contribute to both charge or gap/energy relaxation as

$$\left(\frac{df_k}{dt}\right)_{coll} = -\sum_{k_2} \frac{2\pi}{\hbar} |g_{k_2-k_1}|^2 f(E_1)(1-f(E_2))N(\omega) \quad (2.79)$$

$$\times [\delta(E_1 - E_2 + \hbar\omega) + \delta(E_1 - E_2 - \hbar\omega)(1 + N(\omega))] \quad (2.80)$$

$$\times \begin{cases} \left(1 - \frac{\Delta^2}{E_1 E_2}\right) \psi_1 - \frac{\xi_1}{E_1} \frac{\xi_2}{E_2} \psi_2 & \text{charge} \\ \left(1 - \frac{\Delta^2}{E_1 E_2}\right) (\psi_1 - \psi_2) & \text{gap/energy} \end{cases} \quad (2.81)$$

In this notation $N(\omega)$ is the Bose distribution for phonons of frequency ω , $E_{1,2}$ are excitation energies for the incoming and outgoing quasiparticles, and $|g_{k_2-k_1}|$ is the electron-phonon coupling constant. The deviation functions $\psi_{1,2}$ are used to describe the variations of the distribution function from local equilibrium value f_0

$$f_k = f_0 + f(E)(1-f(E))\psi \quad (2.82)$$

as was done before to define the variation δf_k . Using this, one can relate the superconducting relaxation rates for charge and energy modes to the normal state inelastic relaxation rate $\tau_E(\xi, \hat{k})^{-1}$ by taking the correct limits associated with normal state quasiparticles. Working further with this analysis is quite complex, and only in the limit near T_c does this yield analytic expectations for the

charge and energy mode relaxation times, which are

$$\tau_{Q^*} = \frac{4}{\pi} \frac{k_B T_c}{\Delta(T)} \tau_E(\xi = 0) \quad (2.83)$$

$$\tau_{\Delta} = \frac{\pi^3}{7\zeta(3)} \frac{k_B T_c}{\Delta(T)} \tau_E(\xi = 0) \approx 3.7 \frac{k_B T_c}{\Delta(T)} \tau_E(\xi = 0) \quad (2.84)$$

where $\zeta(3) \approx 1.2$ is Apéry's constant (and ζ is the Reimann-zeta function). The first time τ_{Q^*} is that required for the chemical potential μ_Q to return to zero, while the second time τ_{Δ} is the lifetime for variations of the superconducting gap.

These expressions were found to agree to a similar treatment by A. Schmid [104], and replaced an early theory by Tinkham [93] in which the number imbalance of quasiparticles/holes, rather not their total charge, was thought to determine μ_{Q^*} . The actual choice of phonons as a mechanism for inelastic interactions and use of an approximation near T_c is mostly made as a matter of convenience in calculation and the available experimental evidence at the time. In several similar works these authors largely acknowledge that the Boltzmann approach is general to inelastic relaxation by other mechanisms including electron-electron interactions etc., but are not extensible outside of these limits without more complex calculations.

2.2.5.1 Quasiclassical Description

A more generalized formulation of this approach was developed by A. Schmid and G. Schön [105], derived from the quasiclassical Eilenberger equations [106]. In the diffusive limit, this has evolved into a description of non-equilibrium superconductivity via a many-body Green's function formalism to describe the equations of motion of the system beyond the simple 1D Boltzmann model. This has been outlined extensively in works by our group [107], and as we will not directly apply it for calculations in the present work, we will only sketch the outline of the approach here as it

applies to this topic.

In the Keldysh formalism, one describes the equation of motion of the superconducting Green's function

$$\hat{g} = \begin{bmatrix} \tilde{g}^R & \tilde{g}^K \\ 0 & \tilde{g}^A \end{bmatrix}, \quad (2.85)$$

whose components are the 2×2 retarded (R), advanced (A) and Keldysh (K) Green's functions respectively. The retarded/advanced components in this formalism essentially contain the equilibrium properties of the superconductor, and are related by the Keldysh term by

$$\tilde{g}^R \tilde{g}^K + \tilde{g}^K \tilde{g}^A = 0. \quad (2.86)$$

In this notation, one then introduces a non-equilibrium distribution function \tilde{h} to solve for the Keldysh component as

$$\tilde{g}^K = \tilde{g}^R \tilde{h} - \tilde{h} \tilde{g}^A. \quad (2.87)$$

In this way, the Keldysh Green's function contains all of the non-equilibrium properties of the superconductor, and is thus of the most importance for this discussion. The distribution function \tilde{h} can be further broken down into components which are diagonal in particle-hole space, such that

$$\tilde{h} = h_L \tau^0 + h_T \tau^3 \quad (2.88)$$

where the subscripts denote longitudinal and transverse components, and τ^i are the usual 2×2 Pauli

matrices. As we will see more clearly in a moment, this description is convenient as it pertains to the same particle-hole symmetry discussed earlier for non-equilibrium distributions f_k in that picture. Scattering and relaxation are accounted for by a similarly constructed self energy $\hat{\Sigma}$, which can include contributions from electron-phonon scattering, electron-impurity scattering, or other desired contributions which will dictate the evolution of \hat{g} in various ways. Generally, these will contain a scattering rate term and operators associated with the particular scattering mechanism which are obtained in the first Born approximation.

Now, in terms of the Keldysh Green's functions, one can define the same observables considered before,

$$Q^* = -\frac{eN_0}{4} \int dE \int \frac{d\Omega_p}{4\pi} \text{Tr} \{ \tilde{g}^K \}, \quad (2.89)$$

$$\Delta = \frac{N_0 \lambda_{BCS}}{8} \int dE \int \frac{d\Omega_p}{4\pi} \text{Tr} \{ (\tau^1 - i\tau^2) \tilde{g}^K \}, \quad (2.90)$$

as well as the associated charge and thermal currents

$$J_q = -\frac{N_0}{4} \int dE \int \frac{d\Omega_p}{4\pi} v_f \text{Tr} \{ \tau^3 \tilde{g}^K \}, \quad (2.91)$$

$$J_{th} = -\frac{N_0}{4} \int dE \int \frac{d\Omega_p}{4\pi} E v_f \text{Tr} \{ \tilde{g}^K \}. \quad (2.92)$$

Here the integral over $d\Omega_p$ is taken over all momenta on the full Fermi sphere, while the factor of λ_{BCS} which appears in Δ again accounts for the strength of the BCS pairing interaction.

Expansion of \hat{g} as it appears in the Eilenberger equations, under certain assumptions for strongly

diffusive transport, leads to the well known Usadel equation [108]:

$$[\hat{\tau}^3 E + \hat{\Delta} - \hat{\Sigma}, \hat{g}] - iD \nabla (\hat{g} \nabla \hat{g}) = 0, \quad (2.93)$$

where we consider only the s -wave terms of \hat{g} for conciseness. The derivative operator ∇ is associated with center of mass coordinate R , and thus accounts for the “long-wavelength” changes of \hat{g} only. The square brackets denote the ordinary commutator. Also defined are a set of 4×4 Keldysh matrices in terms of the Nambu-space Pauli matrices τ , where $\hat{\tau}^i = \tau^i \oplus I$ (i.e. they are placed along the diagonal of a 2×2 identity matrix). The matrix corresponding to the pair potential $\hat{\Delta}$ is similarly $\tilde{\Delta} \oplus I$, where

$$\tilde{\Delta} = \begin{bmatrix} 0 & \Delta \\ -\Delta^* & 0 \end{bmatrix}. \quad (2.94)$$

Ignoring self-energy contributions, this can be separated into the following three equations and used to find the three matrices $\tilde{g}^{A,R,K}$:

$$[\tau^3 E + \tilde{\Delta}, \tilde{g}^R] = iD \nabla (\tilde{g}^R \nabla \tilde{g}^R), \quad (2.95)$$

$$[\tau^3 E + \tilde{\Delta}, \tilde{g}^A] = iD \nabla (\tilde{g}^A \nabla \tilde{g}^A), \quad (2.96)$$

$$[\tau^3 E + \tilde{\Delta}, \tilde{g}^K] = iD \nabla [\tilde{g}^R \nabla \tilde{g}^K + \tilde{g}^K \nabla \tilde{g}^A]. \quad (2.97)$$

This first two equations essentially contain the same information, as in this construction $\hat{g}^A = -\tilde{\tau}^3 \hat{g}^{R\dagger} \hat{\tau}^3$, and therefore can only be used to solve for the equilibrium properties of the system. The third equation is the “kinetic equation” for the non-equilibrium distribution function which we

are more interested in. Using Eq. 2.87 and taking the trace of both sides this becomes

$$0 = iD \nabla \text{Tr} \left\{ \nabla \tilde{h} + \tilde{g}^R (\nabla \tilde{g}^R) \tilde{h} - \tilde{h} \tilde{g}^A (\nabla \tilde{g}^A) - \tilde{g}^R (\partial \tilde{h}) \tilde{g}^A \right\}. \quad (2.98)$$

Then, by expansion of \tilde{h} by Eq. 2.88, one finds a set of coupled differential equations for h_L and h_T

$$D \nabla \left[(\nabla h_L) \text{Tr} \{1 - \tilde{g}^R \tilde{g}^A\} + h_T \text{Tr} \{ \tau^3 (\tilde{g}^R (\nabla \tilde{g}^R) - \tilde{g}^A (\nabla \tilde{g}^A)) \} \right] \quad (2.99)$$

$$- (\nabla h_T) \text{Tr} \{ \tilde{g}^R \tau^3 \tilde{g}^A \} \Big] = 0, \quad (2.100)$$

and

$$D \nabla \left[(\nabla h_T) \text{Tr} \{1 - \tilde{g}^R \tau^3 \tilde{g}^A \tau^3\} + h_L \text{Tr} \{ \tau^3 (\tilde{g}^R (\nabla \tilde{g}^R) - \tilde{g}^A (\nabla \tilde{g}^A)) \} \right] \quad (2.101)$$

$$- (\nabla h_L) \text{Tr} \{ \tilde{g}^R \tilde{g}^A \tau^3 \} = i [h_L \text{Tr} \{ \tau^3 [\tilde{g}^R - \tilde{g}^A, \tilde{\Delta}] \} - 2h_T \text{Tr} \{ \tilde{\Delta} (\tilde{g}^R + \tilde{g}^A) \}]. \quad (2.102)$$

Pausing for a moment, the fact that the longitudinal and transverse components of the non-equilibrium distribution function respect *coupled* differential equations immediately tells us that quasiparticle non-equilibrium modes are much more closely related than the simpler Boltzmann picture would imply, and can be mixed. To see this more clearly, we can define the spectral supercurrent Q

$$Q = \frac{1}{4} \text{Tr} \{ \tau^3 (\tilde{g}^R (\nabla \tilde{g}^R) - \tilde{g}^A (\nabla \tilde{g}^A)) \} \quad (2.103)$$

as well as diffusion coefficients $D \times M_{ij}$

$$D \times M_{ij} = \frac{D}{4} \text{Tr} \{ \delta_{ij} \tau^0 - \tilde{g}^R \tau^i \tilde{g}^A \tau^j \} \quad (2.104)$$

to find a more compact set of kinetic equations:

$$\nabla \left[M_{00} \nabla h_L + Q h_T + M_{30} \nabla h_T \right] = 0 \quad (2.105)$$

and

$$\nabla \left[M_{33} \nabla h_T + Q h_L + M_{03} \nabla h_L \right] \quad (2.106)$$

$$= \frac{i}{4D} \left[h_L \text{Tr} \left\{ \tau^3 [\tilde{g}^R - \tilde{g}^A, \tilde{\Delta}] - 2h_T \text{Tr} \left\{ \tilde{\Delta} (\tilde{g}^R + \tilde{g}^A) \right\} \right\} \right]. \quad (2.107)$$

Re-expressing the charge and thermal currents defined before, we have

$$J_q = e N_0 D \int dE (M_{33} \nabla h_T + Q h_L + M_{03} \nabla h_L) \quad (2.108)$$

$$J_{th} = N_0 D \int dE E [M_{00} (\nabla h_L) + Q h_T + M_{30} (\nabla h_T)]. \quad (2.109)$$

Similarly, one can find that the observables Q^* and Δ reduce in the same manner by this choice for \tilde{h}

$$Q^* = - e N_0 \int dE h_T N(E) \quad (2.110)$$

$$\Delta = \frac{N_0 \lambda}{4} \int dE \left[h_L (\tilde{g}^R - \tilde{g}^A) + h_T (\tilde{g}^R \tau^3 - \tau^3 \tilde{g}^A) \right]_{12}. \quad (2.111)$$

Here, the subscript ‘12’ refers to the upper left component of the integrand, and

$$N(E) = \text{Tr} \left\{ \tau^3 (\tilde{g}^R - \tilde{g}^A) \right\} / 4 \quad (2.112)$$

is the superconducting density of states in this notation. We can see clearly that only the transverse

component of the non-equilibrium quasiparticle distribution function is associated with charge imbalance, while both elements of the transverse and longitudinal components can combine to determine the gap. Both charge and thermal currents are generated (in differing amounts which depend on M_{ij}) by gradients in the longitudinal or transverse distributions. This is the simplest form of coupling between imbalance modes, and accounts for interconversion of the orthogonal parts of the distribution. Because the integrand in J_q appears in the second kinetic equation, the terms on the right-hand side there account for interaction between the quasiparticles' charge and the condensate.

As is almost always the case, these equations are only tractable numerically. For the type of devices commonly studied in our group, this is typically done by treating an entire device as a system of 1D wires with boundary conditions appropriate for the device construction, and working within certain parameterizations of the Green's functions to simplify calculations. Solutions are found by iteratively solving for the retarded/advanced Green's functions to determine equilibrium properties and then then applying the kinetic equations to determine the non-equilibrium distributions (which in turn, inform the boundary conditions). In the ordinary case of clean normal-superconductor interfaces, one usually uses Kurpianov-Lukichev boundary conditions [109]. However for the tunneling interfaces we will be studying here, we have yet to find a satisfactory approach for calculating boundary conditions for NIS tunneling which works within our existing code-base.

In order to describe relaxation of quasiparticles, we would also need to somehow re-introduce the self energy contributions responsible for elastic and inelastic scattering. In practice the application of specific relaxation mechanisms is quite tricky, but amounts to re-introduction of collision terms to the right hand side of the kinetic equations which traces over the Keldysh component of $[\hat{\Sigma}, \hat{g}]$. One can also include a spin-splitting energy $\vec{h} \cdot \vec{\sigma}$ in the same manner, and in doing so split the

problem further into four sets of kinetic equations which govern the spin-imbalance and spin-energy-imbalance of quasiparticles. These re-castings of the Usadel equation are described in length in works by F.S. Bergeret et al. and T.T. Heikkilä et al. [110, 111].

With this, we have seen that quasiparticle imbalance modes can be robustly separated by their symmetry in quasi-particle/hole space, where h_T results in charge imbalance alone. The presence of a finite super-current causes the phase of the order parameter to evolve as a function of position, while mixing the h_T and h_L distributions via the kinetic equations. Relaxation, while not as easy to bake into the problem as before for the simple Boltzmann picture, can be accounted for by considering inelastic and elastic self energy contributions which will occur at energy/temperature dependent rates depending on the precise mechanism at play. Thermal and charge currents can also be generated by gradients in these distributions, which will naturally result during relaxation, giving a sort of continuity equation for charge and energy flow between the quasiparticles and the condensate.

2.3 Superconducting Phenomenology

So far, we have only considering microscopic factors important for understanding quasiparticles for an ideal BCS system. As the results in Ch. 4 will chiefly pertain to bulk equilibrium properties of superconducting Nb films, here we will describe some of the relevant background to those experiments with an eye towards transport properties. Then, we will sketch the analysis for transport in a superconducting wire which is of relevance to results in §5.3.3.

2.3.1 Ginzburg-Landau Phase Boundary

The Ginzburg-Landau (GL) theory of superconductivity serves as a macroscopic or phenomenological model for the superconducting phase. To discuss this, we will again follow the presentation

of Tinkham [30] to arrive at the useful pieces of this theory for analysis. In its original description, GL theory was based on the postulate of a free energy functional

$$f = f_0 + \alpha|\psi|^2 + \frac{\beta}{2}|\psi|^4 + \frac{1}{4m_e} \left| \left(\frac{\hbar}{i} \nabla - \frac{2e}{c} \vec{A} \right) \psi \right|^2 + \frac{H^2}{8\pi} \quad (2.113)$$

where again ψ is the magnitude of the order parameter, and α, β are parameters which determine the shape of the free energy functional. The charge and mass values used are those for individual electrons. The fourth term is the canonical kinetic energy of the system subject to a vector potential \vec{A} , and the fourth is the energy of the H field associated with the vector potential. This form is chosen as the values α and β determine if and of what value the finite order parameter should be, as the minima of the free energy will jump discontinuously just as it would during a phase transition, resulting in a spontaneously broken symmetry due to the finite order parameter. The value of the order parameter for $\alpha < 0$ with $\vec{A} = 0$ will be $|\psi_{\text{inf}}|^2 = -\alpha/\beta$. This is equivalent to the (fractional) superfluid density of paired electrons. The magnitude of the free energy reduction $f_s - f_n$ in this case can be associated to a thermodynamic critical field H_c , such that $H_c^2/8\pi = -\alpha^2/2\beta$. Finally, an energy analysis of the canonical kinetic energy term gives an effective penetration length for the GL model,

$$\lambda_{eff}^2 = \frac{mc^2}{8\pi e^2 |\psi|^2}, \quad (2.114)$$

which differs from the historically used London penetration depth [112]

$$\lambda_L(T) = \frac{\lambda_L(0)}{\sqrt{2(1 - T/T_c)}} \quad (2.115)$$

which is defined solely by its zero temperature value

$$\lambda_L(0) = \sqrt{\frac{mc^2}{4\pi ne^2}}, \quad (2.116)$$

which will be useful later.

The model is solved at a given temperature by insertion of the thermodynamic critical field $H_c(T)$ and one finds that

$$|\psi_{\text{inf}}|^2 = \frac{mc^2}{8\pi e^2 \lambda_{eff}^2(T)}, \quad (2.117)$$

$$\alpha = -\frac{2e^2}{mc^2} H_c^2(T) \lambda_{eff}^2(T), \quad (2.118)$$

$$\beta = \frac{16\pi e^4}{m^2 c^4} H_c^2(T) \lambda_{eff}^4(T). \quad (2.119)$$

Treating ψ as a complex scalar field, $|\psi(r)|e^{i\phi(r)}$, variation of the free energy about its minima yields the GL differential equations

$$\alpha\psi + \beta|\psi|^2 + \frac{1}{4m} \left(\frac{\hbar}{i} \nabla - \frac{2e}{c} \vec{A} \right)^2 \psi = 0 \quad (2.120)$$

$$\vec{J} = \frac{e\hbar}{2mi} (\psi^* \nabla \psi - \psi \nabla \psi^*) - \frac{2e}{mc} \psi^* \psi \quad (2.121)$$

$$\equiv \frac{e}{m} |\psi|^2 \left(\hbar \nabla \psi(\vec{r}) - \frac{2e}{c} \vec{A} \right) \quad (2.122)$$

such that $\nabla \times \vec{H} = 4\pi \vec{J}/c$. Again taking $\vec{A} = 0$, Eq. 2.120 can be dimensionalized by a coherence length

$$\xi(T) = \sqrt{\frac{\hbar^2}{4m|\alpha(T)|}} \equiv \frac{\Phi_0}{2\sqrt{2}\pi H_c(T) \lambda_{eff}(T)}, \quad (2.123)$$

which describes the characteristic length-scale for small variations of the order parameter. At zero temperature, this is related to the zero temperature BCS gap as

$$\xi_0 = \frac{\hbar v_f}{\pi \Delta(T=0)}, \quad (2.124)$$

and can be expressed back as

$$\frac{\xi(T)}{\xi(0)} = \frac{\pi}{2\sqrt{3}} \frac{H_c(0)}{H_c(T)} \frac{\lambda_L(0)}{\lambda_{eff}(T)}. \quad (2.125)$$

For many materials, the coherence length can be comparable to the elastic mean free path $l = v_f \tau$ for electrons in the normal metal. Recalling the Drude model, in a bulk material this is related to the diffusion constant $D = v_f l / 3$, but can also be calculated from known values of v_f and m_e^* and resistivity for a given material, as $\rho_0 l$ is typically a constant depending on the material. For instance, in Al $\rho_0 l = 39.4 \mu\Omega \text{cm} \times \text{nm}$ but for Nb $\rho_0 l = 86.7 \mu\Omega \text{cm} \times \text{nm}$ [113]. The electromagnetic response of the dirty superconductor turns out to depend on both l and ξ_0 , as dephasing of the pair wave-packet does not occur over a length $v_f \times \hbar / \Delta$, but instead a length $\sqrt{D \hbar / \Delta} \propto \sqrt{l \xi_0}$ (the geometric mean of the mean free path and the coherence length) due to the velocity being slower in the diffusive limit [114, 115]. If $l \ll \xi_0$, then the material is said to be in the dirty limit, while in the opposite case it is in the clean limit. This appears in many calculations both for the BCS and GL models as being a critical limit, as for $l \ll \xi_0$ it is argued that l sets the actual length-scale for changes of the order parameter. For instance, near T_c Tinkham provides the following two limiting

cases for a bulk 3D superconductor

$$\xi(T) = \begin{cases} 0.74 \frac{\xi_0}{\sqrt{1-T/T_c}} & \text{clean-limit} \\ 0.855 \sqrt{\frac{\xi_0 l}{1-T/T_c}} & \text{dirty-limit.} \end{cases} \quad (2.126)$$

In a similar sense, one can invoke the electrodynamic response from BCS theory to find the effective penetration depth for the extreme dirty limit near T_c , and relate that back to the London model per

$$\lambda_{eff} \approx \lambda_L \sqrt{\frac{\xi_0}{1.33 l}}. \quad (2.127)$$

In practice, the crossover between the clean and dirty limit is not always clear, as BCS superconductors are typically insensitive to disorder [116], and generalizations of are typically made based on which limit appears to agree with experiments.

From this point, one can derive many thermodynamic properties of the GL model and take limits for the behavior near T_c which are useful for a wide variety of characterization methods. In the context of dc-transport however, one can only easily measure the space of $R(T, H)$ where superconductivity fully breaks down and a finite resistance is observed everywhere in the sample. Upon linearizing the GL differential equation into

$$\left(\frac{\Delta}{i} - \frac{2\pi \vec{A}}{\Phi_0} \right)^2 \psi = \frac{\psi}{\xi^2(T)} \quad (2.128)$$

and introducing a magnetic field along the z -axis, one finds by solution of this wave equation that there is such a maximal field for maintaining superconductivity in the bulk, where the zero

resistance state will become fully suppressed

$$H_{c2} = \frac{\Phi_0}{2\pi\xi^2(T)} \quad (2.129)$$

This upper critical field is related to the thermodynamic critical field by

$$H_{c2}(T) = \frac{4\pi\lambda_{eff}(T)H_c^2(T)}{\Phi_0} = \sqrt{2}\frac{\lambda_{eff}(T)}{\xi(T)}H_c(T) \equiv \sqrt{2}\kappa(T)H_c(T). \quad (2.130)$$

Critically, this GL ratio for the material $\kappa(T)$ is, by the same reasoning as before for ξ , different in the dirty and clean limits. At T_c for a totally bulk superconductor, this ratio is

$$\kappa = \begin{cases} 0.96 \frac{\lambda_L(T=0)}{\xi_0} & \text{clean-limit} \\ 0.72 \frac{\lambda_L(T=0)}{l} & \text{dirty-limit,} \end{cases} \quad (2.131)$$

where λ_{eff} has been rewritten in terms of the zero temperature London length which appears in the dirty case via Eq. 2.127 or from the clean case via Eq. 2.116. In the dirty case, there is a cancellation of terms with those of the dirty limit penetration length. This parameter κ is a key classification for the behavior of the superconductor into either Type-I (where $H_{c2} < H_c$) in which the magnetic field is fully expelled or Type-II where flux penetrates the superconductor in vortices. As we will not discuss vortex matter in any detail, and will be focusing almost exclusively on thin films where the penetration depth becomes large due to the sample geometry, we will assume $\kappa \gg 1/\sqrt{2}$ for the samples considered in the following chapters, but its exact value remains a matter of material purity.

Finally, at zero temperature, we arrive at the relation that $H_{c2}(0) = \Phi_0/2\pi\xi_0^2$, while at higher

temperatures near the zero field transition temperature $T_c(0)$, one can find that

$$T_c(H) = T_c(0) \left(1 - \frac{2\pi\xi_0^2}{\Phi_0} H_\perp \right). \quad (2.132)$$

Thus, measurements of the phase boundary itself, even performed via a resistive method, can be used to back out the underlying zero temperature properties of the material, and with additional assumptions, can be used to estimate many further thermodynamic properties as well. This can be especially useful in cases where the resistance of a sample is dominated by grain boundaries or an impurity phase, which will tend to make the bulk resistivity appear quite large even if the superconductivity is not suppressed within those grains by any particular amount of disorder.

2.3.1.1 Notes on Superconductivity in Nb

With the GL and BCS descriptions briefly described, it is worth pointing out that some of the assumptions for those models fail for the kinds of Nb films used in various capacitors, waveguides and resonator elements of qubits.

On the material side, Nb is a refractory metal with a particularly high melting temperature (2741 K) at which it also has a relatively low vapor pressure (4×10^{-4} Torr) [117], making deposition somewhat challenging. It is also a fairly reactive metal, forming oxides, nitrides and carbides [118, 119, 120, 121], thus gettering any contaminants present during physical vapor deposition. Because of this, deposited films of pure Nb can vary chemically with extreme sensitivity to the conditions of the deposition chamber which complicates process development of Nb devices. After deposition, it continues to have unusual kinetics even at low temperatures. For instance, aggregates of Nb hydrides are seen to form during cooling [122], creating isolated non-superconducting grains within the film around liquid nitrogen temperatures. Even under ideal conditions, Nb readily forms a

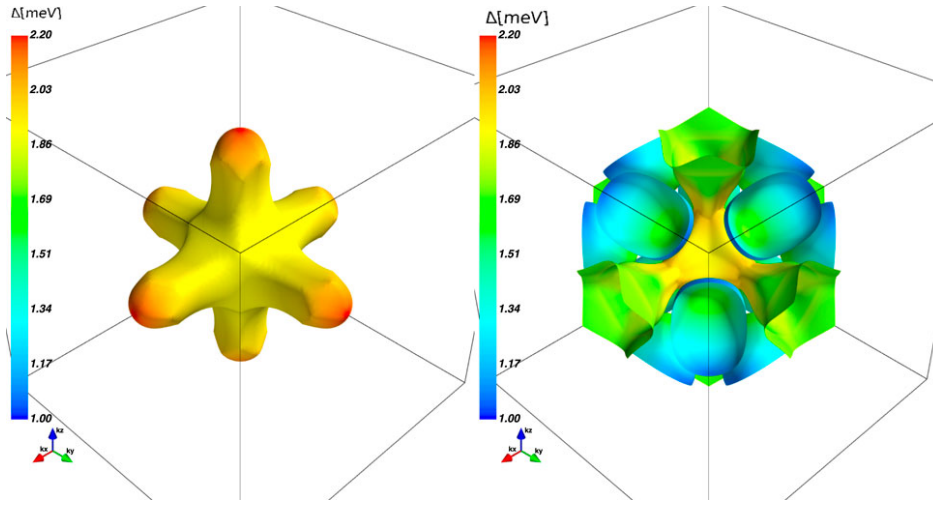


Figure 2.9: Dual-band gap structures for Nb, reproduced from Ref [91]. “The value of $\Delta(p)$ at $T = 3.0$ K at each point of the Fermi surface for the two sheets. The box spans $[\pi/2a, \pi/2a]$ in k -space along each direction for the first sheet (left panel) and $[\pi/a, \pi/a]$ for the second sheet (right panel).”

relatively thick ≈ 5 nm native surface oxide NbO_x ($x=1-2$) [119]. These surface oxides complicate the phenomenology of Nb based superconducting devices, especially when films are thin. They similarly inhibit the formation of tunnel junctions via metallic shorts in native NbO_x and provide a poor quality surface for tunneling spectroscopy based measurements in general, concealing the clean superconducting behavior of the bulk [123, 124]. These Nb surface oxides are thought to have very poor dielectric response at microwave frequencies, due to their amorphous and metallic nature [125, 126, 127, 12, 13, 8], as well as local magnetism [128], and thus in real experiments one might consider Nb to always be in proximity to metallic/magnetic surfaces. In terms of superconductivity, Nb is a BCS superconductor with transition temperature of 9.25 K and zero temperature $H_c(T = 0)$ of 2 kOe [129]. However, it has long been pointed out that Nb should have a slightly anisotropic gap consisting of two bands (as may Ta, V, Al etc.) [130, 131, 90, 132, 91] due to the highly distorted nature of its Fermi surfaces. A visualization of Fermi-surface and the resulting gap structures is shown in Fig. 2.9. The resulting anisotropy of the superconducting gap

is thought to be fairly weak, but as anisotropic superconductors are susceptible to pair-breaking by non-magnetic disorder (unlike isotropic superconductors) [116], this may begin to explain the failure of the BCS predictions for quasiparticle density. Similarly, gap anisotropy is known to enhance branch-mixing of quasiparticles [101, 102], and therefore it is possible that simple models for quasiparticle non-equilibrium will not be sufficient to understand their dynamics in Nb devices.

The presence of a potential second gap (which is strongly suppressed by disorder) violates most of the basic assumptions made in the BCS theory. To complicate things further (although the subject of a long-standing experiment-theory divide) Nb is said to be an intermediate to strong-coupling superconductor with $\lambda_{BCS} \approx 0.5 - 1.3$ [133, 134, 135, 136, 137, 91, 138] depending on which Fermi surface is considered. This further subverts the usual BCS calculations for the gap for the weak coupling case where $\lambda_{BCS} \ll 1$, and makes first principles theories of superconductivity in Nb quite complex. As Nb tends to form into tightly granular structures, one does not typically see corresponding transport anisotropy in bulk crystals or thin films produced via sputtering, as the gap will be averaged out over countless grains with random orientations. However, for annealed films or films deposited at high temperature, a large degree of epitaxy is likely, and control of the overall orientation of an entire film becomes possible. In that case, anisotropy could become relevant for applications.

As a final important note, Nb is known to tend rapidly to type-II behavior for many types of disorder [139, 129, 140, 141], including non-magnetic scattering, a fact which was extensively studied and attributed very early on to anisotropy of the superconducting gap [131]. Mostly significantly, the superconductivity in Nb is found to be highly sensitive to oxidation of the bulk, with T_c dropping by 1 K for every $\approx 1\%_{at.}$ O_2 and H_{c2} rapidly increasing due to shifts of the Fermi-level via

doping which modify λ_{BCS} and N_0 [142]. As such, observing changes in the superconducting properties of Nb films can be an extremely sensitive means for understanding the bulk oxidation of a device. Conversely, this also means that one must be quite careful to first understand the disorder, doping, and crystal structure of Nb when making strong claims about the microscopic factors associated with device performance.

2.3.2 Current and Phase in Superconducting Wires

As a final theoretical point, we must describe the effects of a large applied current across a superconductor, as this will turn out to pertain to the GL properties of the material and to its quasiparticles as we will see in §2.3.2. A thin, effectively 1D superconducting wire will have a critical current at which the order parameter is minimized at zero and the device becomes normal. This can be found via the GL free energy as

$$J_c = \frac{cH_c(T)}{3\sqrt{6}\pi\lambda_{eff}(T)}. \quad (2.133)$$

At large supercurrent, there is a corresponding superfluid velocity $\vec{v}_s = \vec{J}_s/2e|\psi|^2$, which upon reaching a critical value

$$|v_{s,c}| = \frac{\Delta(0)}{\hbar k_f} = \frac{\hbar}{\pi m \xi_0} \quad (2.134)$$

leads to a shift in the energies of quasiparticles of wave-vector \vec{k} by $\hbar\vec{k} \cdot \vec{v}_s$ which causes de-pairing and the formation of non-equilibrium quasiparticles [143]. At large currents, this yields a reduction of the gap and thus the critical current drops sharply and the wire runs away into the normal state. At low enough temperatures the occupation of equilibrium quasiparticles is very small, and the drop in Δ can occur more slowly than the corresponding drop in the excitation energy of the

quasiparticles, which then goes as:

$$E_K \rightarrow E_k^0 + \hbar \vec{v}_k \cdot \vec{v}_s. \quad (2.135)$$

such that the minimum excitation energy of a quasiparticle is lowered *below* Δ [143].

This is sometimes referred to as an effective ‘‘Doppler effect’’ for the quasiparticle spectrum, and for currents just below J_c could lead to a (nearly) gapless excitation spectrum. This has interesting implications, especially for the critical state of a superconductor in an applied magnetic field where the onset of this gapless state has come to be known as the ‘‘Volovik Effect’’, named so for a prediction of G.E. Volovik for the density of states of quasiparticles near vortex cores [144]. This has thermodynamic considerations for unconventional superconductors [145], but for the purposes of this work the Volovik effect has been shown to lead to depairing consistent with a finite Dynes parameter

$$\Gamma/\Delta_0 = \frac{\hbar}{2D} \langle \vec{v}_s^2 \rangle \quad (2.136)$$

via tunneling density of state measurements in the presence of a large supercurrent [146].

As J_s is increased from zero, a phase difference is built up across the wire, leading to a gradient $\Delta\phi(x)$ and an overall complex order parameter. When considered quasiclassically, this can lead to mixing of the charge and energy mode non-equilibrium types. For instance, it is well known that a temperature gradient ΔT (a gradient in the energy imbalance temperature T^*) can couple to $\vec{v}_s \cdot \nabla T$ to yield an excess charge imbalance [147, 148]. More recently, this has been discussed in the context of mixing all non-equilibrium modes including spin-imbalance due to the coupling terms of the Usadel (kinetic) equations [149]. The exact magnitude of the phase gradient is somewhat

sample specific. For short superconducting weak links this will typically be sinusoidal as was the case for a Josephson junction, but for longer superconducting wires attached to superconducting reservoirs this need not be the case, and non-sinusoidal current-phase relations are possible.

CHAPTER 3

METHODS

In this chapter, we will first outline the methods used for the preparation of samples and devices studied in the following two chapters. As our lab has a long history in lithography and superconducting film preparation, we will focus mostly on the novel processes and recipes developed specifically for this work. Then, we will discuss nuances of the cryogenic measurements themselves, with a focus on particularly unique experimental techniques. There, we will primarily discuss methods required for non-local conductance measurements, as these experiments involved the development of a bespoke set of amplifiers with their own set of additional experimental considerations.

3.1 Lithography and Fabrication

Production and measurement of transport devices with reliable behaviors requires a degree of diligence be taken at every step of the process, starting from substrate preparation all the way through to the end of the experiment. This begins at the first stage of fabrication, where choices must be made about material selection and handling that can ultimately determine the yield of devices and the outcome of one's experiments. For the projects described in the following chapters, two paths were chosen. To study superconductors used *for* quantum devices, samples were obtained from collaborators via SQMS and processed in our lab. However, for more demanding devices required to study non-equilibrium transport in superconductors, we construct devices entirely "in house" to have full control of the sample design.

3.1.1 Physical Vapor Deposition

As a starting point for all of the devices in this work, physical vapor deposition is performed to deposit high quality metals for the purpose of wafer-scale or nano-fabrication of superconducting films and electrical contacts. The choice of growth conditions ultimately determines which of two paths can be taken during device fabrication.

For wafer-scale processes, or for growth conditions which require that the substrate be heated to yield the correct material phase or substrate-film epitaxy, dc- or rf-magnetron sputtering are typically performed, often from a 2" or larger high purity target in ultra-high vacuum. This method can produce extremely high quality films, but is not typically used to directly produce patterned structures as sputtering is not a "line of sight" process due to large diameters of the targets and generally shorter throw distance between the source and the sample. Thus, sputtering is more appropriate for fast deposition of high purity, large area films in ultra-high vacuum. As our lab does not specialize in sputtering techniques, and we wished to consider only materials known for their use in quantum devices, we have instead used "full-coverage" or "blanket" films provided by several sources in much of the work to follow, which we pattern using Ar ion milling (§3.1.2.1) or reactive ion etching (§3.1.3.3). As this work was largely performed at other labs, we will only remark on these techniques as necessary for comparison of results in the following chapter.

For devices defined at the time of deposition using photo- or electron-beam lithography, wherein a polymer resist mask is present during the deposition and used to lift-off the unwanted metal layers afterwards, it is typical to use electron-beam vapor deposition. For this, we have used our lab's "JoeTek" electron-beam evaporator, which was extensively rebuilt between 2023 and 2024 to restore high vacuum performance. In this system, an electron beam (≈ 30 to 120 mA) is generated from a high-voltage filament (≈ 5 kV) and focused into a small point upon a metal filled crucible,

	Crucible Type	Source Purity	Approx. Power (W)	Deposition Rate ($\text{\AA}/\text{s}$)	Active Pressure (Torr)
Al	IM (BN-TiB ₂)	5N	425-450	1.0-3.0	4×10^{-7}
	<i>Wetted IM crucibles should carefully cleaned of excess metal on the rim/outside.</i>				
Ti	C	4N	375-400	0.5-1.0	2×10^{-7}
	<i>Ti should be deposited at the lowest possible pressure, at no less than 0.5$\text{\AA}/\text{s}$.</i>				
Cu	C	5N	250	3.0-5.0	$5-8 \times 10^{-7}$
	<i>Cu must be thoroughly pre-evaporated to prevent deposition of CuO₂.</i>				
Au	Mo, Vitreous C	3N	275-425	2.0-3.0	$0.9-1.2 \times 10^{-6}$
	<i>Au spitting is commonly observed, use slow heating.</i>				

Table 3.1: Typical deposition conditions for metals used in this work, as prepared in the “JoeTek” evaporator. Active pressure refers to the recorded pressure of the chamber during deposition at the listed rate, and is typically higher than the ultimate base pressure due to heating of the chamber.

which heats it and produces a vapor. We make use of the point-like nature of the source and a long separation between source and the sample to both preserve the quality of the polymer resist mask and to ensure good pattern rendition across the device (i.e., the material to be deposited is essentially collimated when it reaches the substrate). While this limits the selection of materials to those with a finite vapor pressure at the temperatures achievable by the source, electron-beam deposition is the best means for direct patterning of many mesoscopic devices, especially when using angled evaporation (§3.1.3.2).

In electron-beam deposition, careful control of the crucible quality and conditions in the chamber must be exerted to obtain consistent results. Unless otherwise stated, devices patterned in this fashion are typically deposited via parameters found in Tab. 3.1 using the “JoeTek”. This system uses a watercooled UHV Telemark 308 emitter and 1.5cc crucible liners from SCM-Inc (15° taper, 0.700” diameter, 0.515” tall, 0.093” wall thickness), and reaches a pressure of 4×10^{-7} Torr in less than 3 hours, with a ultimate base pressure of about 1.5×10^{-7} Torr being obtained after 5-6 hours at the time of writing. The system is also equipped with a high-voltage source for plasma etching, consisting of a 2 kV step up transformer and a high voltage rated 500 k Ω ballast

resistor, which biases the rotatable sample stage to produce a very low power (<1 W) plasma etch which aids the adhesion of the metal to the substrate. Unless otherwise stated, films were deposited after application of a 30-90s, 40 mTorr O_2 plasma etch using this arrangement. For devices which require controlled formation of a thermal oxide to act as a tunnel barrier, oxidation can be performed in situ with the O_2 pressure read out by a Terra-nova convectron gauge tube controller. Best results seem to be obtained with dynamic oxidation, in which a controlled flow of gas is introduced into the chamber and the pressure monitored to achieve a constant dynamic pressure of ≈ 100 mTorr for 15m. Attempts at static oxidation under similar conditions have been less successful, possibly due to excessive gettering of the process gas by the inside panels of the chamber.

On a final note, we have recently adopted the use of inter-metallic (IM) crucible liners for deposition of Al metal, which is not susceptible to degradation due to the Al melt, unlike graphite. These crucibles also happen to wet Al, requiring diligent use and occasionally mechanical removal of an Al film from the outside of the liner which will form fairly quickly (even at low deposition rates). If properly maintained, these allow for high quality Al evaporation from a single liner over many cycles without much issue. Thus was found to be especially important in attempts to deposit non-superconducting 2% Mn doped Al films (Goodfellow AJ18-LP $Al_{98}Mn_{02}$ alloy), which were found to rapidly degrade graphite crucibles after only 1-2 uses, typically cracking during the evaporation itself (not during warming/cooling). We posit that the Mn doping or other impurities may contribute to accelerating a reaction between the melt and the liner at high temperatures, forming a powdery carbide. These alloys were also found to outgas during deposition, and extreme caution should be taken as this can lead to spitting of metal out of the crucible of the Joetek, leading to shorting of the emitter. For similar reasons, electrically insulating hBN crucibles should be avoided, as buildup of charge can lead to erratic beam deflections, and at the small scale of the

crucibles used in this chamber, can even cause ejection of the melt from the liner entirely.

3.1.2 Photolithography and Ion Milling

Photolithography is generally the most efficient means to prepare large samples via metalization, as a physical mask is used to transfer the exposure pattern from a flood-style UV source. Thus the exposure time is essentially independent of the pattern area and large structures can be prepared rapidly. To define these structures onto an existing film, it is easiest to use negative tone photolithography to produce resist masks for etching. By convention, negative tone indicates that only the exposed region of the pattern remains after development, as is the case in film photographic negatives. A smaller exposure area is used than in positive tone lithography, allowing for the entire wafer to be cleared of metal except for the desired device while keeping the mask area relatively compact. For this type of patterning, AZ-nLOF 2035 photo-resist was used, as it is a simple to use single layer negative tone resist. This can then be followed by either reactive ion etching (RIE) or Ar ion milling with the nLOF layer serving as a soft-mask, as was used for fabrication of the devices detailed in §4.1. A basic recipe for this resist preparation can be found in Tab. 3.2. In some cases, a single layer of positive tone S1815 resist was prepared instead via the conventional recipe for our lab, which was spun to be slightly thicker than usual at a spin-speed of 2000 rpm.

3.1.2.1 *Recipe for Soft Masked Ar Ion Milling*

Large area patterning of our Hall-bar devices and large area leads was performed by Ar ion-milling to minimize the risk of significantly altering the film itself. Our lab's ion-mill was originally constructed for the purpose of etch patterning the highly charge/vacancy sensitive surfaces of complex oxide perovskites such as SrTiO₃ [150]. Given the success in this and other tasks, we do not expect this process to substantially heat the sample or penetrate the resist layer, and it is used whenever

AZ-nLOF

1. Spin AZ-nLOF 2035 at 2000 rpm on a solvent cleaned metalized wafer, typically ≤ 150 nm of Nb on Al_2O_3 .
 2. Bake on a hotplate covered with a glass dish at at 130°C for 3m. Note that, due to the poor thermal conductivity of Al_2O_3 compared to typical p-doped Si substrates, the relevant hotplate bake temperatures will be higher than expected from the datasheet.
 3. Expose at 75 mJ cm^{-2} on the NUFAB Suss MJB4 Mask Aligner.
 4. Post-exposure bake on a hotplate covered with a glass dish at at 130°C for 1m (This step is required to cross-link the exposed resist and sets the final pattern).
 5. Develop immediately in a 2 path process consisting of:
 - (a) MF319 at room temperature for 60s with gentle stirring to obtain a straight sidewall. To introduce undercut, extend this time to 80s.
 - (b) DI water soak for 5-10 seconds followed by immediate N_2 blow dry.
 6. Metalize or etch as needed. Liftoff in 65°C Remover PG for at least 10 minutes, followed by an isopropanol soak/spray and N_2 blowdry. **Do not use acetone**, as this can cause nLOF to harden/congeal and makes the process much harder. If films of residual nLOF are visible under the microscope (typically the result of hard baking during etching), ultrasonicate in alternating baths of Remover PG and isopropanol for several minutes until the unetched surface returns to its pristine appearance.
-

Table 3.2: Recipe for photolithography of Nb devices on Al_2O_3 substrates with AZ-nLOF based negative tone resists.

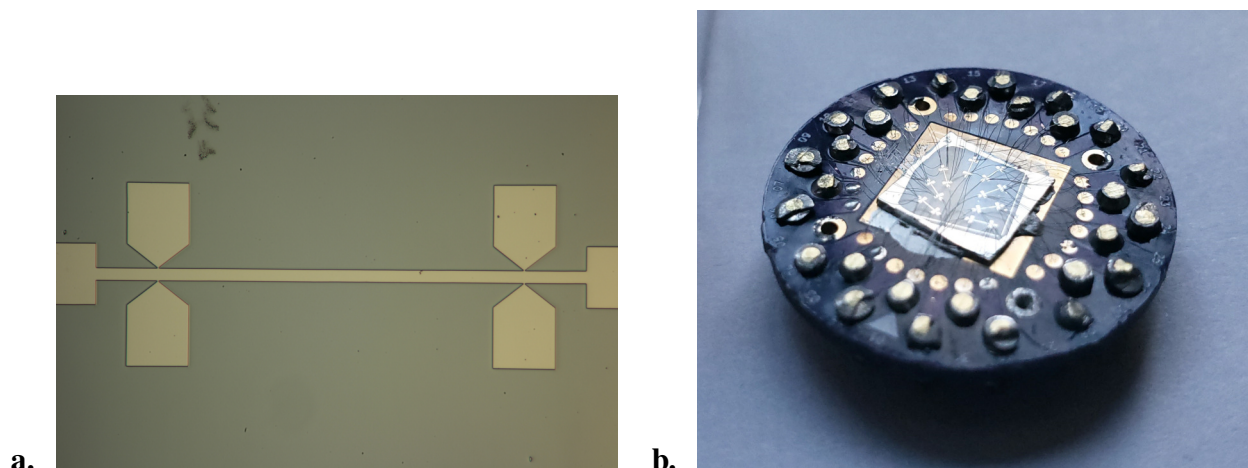


Figure 3.1: a.) Example Hall bar produced via photolithography of a Nb on Al_2O_3 film. b.) Angular array of Hall bars defined at various angles with respect to the substrate crystal directions, for the study in 4.1.1, mounted to customized sample holders for cryogenic measurements.

possible to preserve film quality. Examples of samples formed by this method are shown in Fig. 3.1

The etching rate obtained during ion-milling is predominantly a function of the beam-energy, which is set by the beam voltage of the Kaufman source installed on our chamber. The landing energy is set by the controller's beam energy setpoint, for instance at a beam energy of 600 V a plasma of Ar^+ ions are produced and accelerated to a kinetic energy of 600 eV when they arrive at the sample. The controller produces a specified Ar plasma density to reach the desired beam power. The mill then neutralizes the resulting Ar^+ fluence via the injection of electrons from a secondary high voltage filament towards the sample. High voltage beam optics ensure that the resulting neutrally charged beam towards the sample remains collimated and uniform over the beams ≈ 4 cm diameter. This allows for highly uniform etching rates across even a moderately sized substrate.

Multiple tests were performed to determine the effective etching rate of Nb under our standard pro-

Standard Etch	Cath. V	Cath. A	Dist. V	Dist. A	Beam V	Beam mA	Accl. V	Accl. mA	Emis. mA	Ntrl. V	Ntrl. A
Setpoint Value	—	8.00	40.0	0.80	600	44.0	120	5.0	44.0	—	10.5
Run Value (\approx)	7.4	6.7	40.0	0.8	600	44	120	6.3	44	8.2	9.2

Slower Etch	Cath. V	Cath. A	Dist. V	Dist. A	Beam V	Beam mA	Accl. V	Accl. mA	Emis. mA	Ntrl. V	Ntrl. A
Setpoint Value	—	8.00	40.0	0.8	400	18.0	80	5.0	18.0	—	10.5
Run Value (\approx)	6.3	5.8	40.0	0.26	400	18.1	80	3.1	18.0	7.6	8.7

Table 3.3: Process parameters for etching Nb films via our Ar Ion Mill, when using a flowing Ar gas pressure of 1.6 mTorr. Setpoint values are those programmed on the Kaufmann source controller before operation. The run values indicate the approximate steady state values measured with the beam enabled.

cess conditions, and the removed film thickness was determined to be approximately 15 nm/min. The corresponding etch rate of the nLOF resist mask is presumably low, surviving etches of over 15 minutes in duration. Consequently, our milled Nb films are typically slightly over-etched deliberately to ensure total isolation of neighboring contacts or devices, by 1-2 minutes (15-30 nm). Process parameters are included in Tab. 3.3 for Nb etching via our ‘standard’ process, as well as for a slower etching recipe at about half of the total beam power which has been tested and shown to be suitable for more sensitive applications including etching of metallic nanoparticles. In other experiments our standard process has also been successful in milling Au films, including epitaxial Au on Nb films prepared via molecular beam epitaxy via the Bedzyk group at Northwestern, as well as films which are instead hard-masked via SiO₂. This is especially useful as the F-based etching processes currently available via clean rooms at the Northwestern University Micro/Nano Fabrication Facility (NUFAB) cannot pattern Au or Au encapsulated Nb, and thus our technique could be applied to patterning Au/Nb microwave resonators or qubit devices in the future.

3.1.3 Electron Beam Lithography and Deposition

To define structures which contain feature sizes $< 1 \mu\text{m}$, electron-beam lithography (EBL) is used due to the lower diffraction limit of a Scanning Electron Microscope (SEM) and the high resolution

of electron-beam resists. As the general case of this technique has been explored extensively by our group, we will focus on specific developments of our lab's EBL process which enable the devices described in the following chapter.

3.1.3.1 SEM Interface Buffers

In 2022, our lab installed an updated Tescan Mira 4 SEM for general specimen imaging and EBL. Interfacing this instrument with the Analog-Digital-Converter (ADC) of our existing E-scribe system required the construction of a new buffer unit for control of the scan coils and beam blanker during EBL and readout of the image signal. With exception of the blanker, this is achieved with AD624 unity gain amplifiers with a bandwidth of 1 MHz powered by an encapsulated supply in a unit which sits beside the SEM as shown in Fig. 3.2.b. The buffers can be output offset tuned to correct for issues with pattern rendition or image contrast. An additional non-inverting buffer is

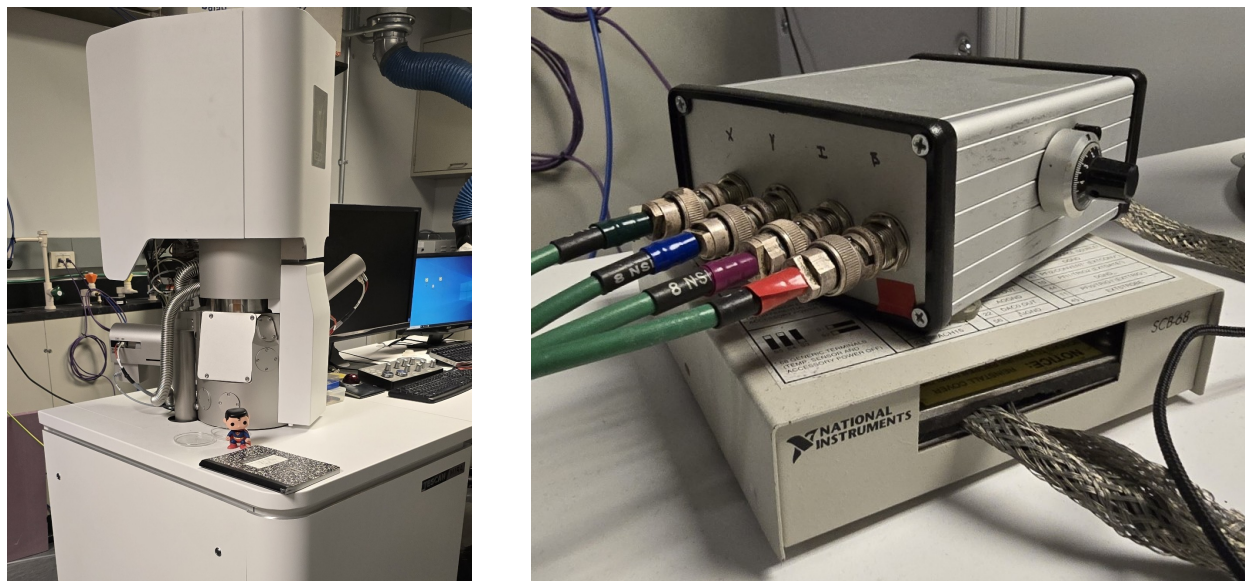


Figure 3.2: Images of the new Tescan SEM for EBL. Left: Tescan Mira 4 SEM Right: Interface buffer for EBL writing.

provided for beam blanking using an LF356 op-amp with a bandwidth of 5 MHz. To adjust the contrast/black-level of the image read out from the SEM during alignment operation in E-scribe, an additional offset signal is sent to the ADC board sourced from a voltage divider/potentiometer added to the buffer unit. This allows for the image signal from the SEM's selected detector to be brought up so that a normal image contrast is obtainable near ± 1 V and is fed into the inverting input of the ADC. At the time of writing, this has been tuned manually so that approximately equal contrast is obtained between the SEM live window and what appears in single scan mode for alignment of the E-scribe software, however for finer alignment this may benefit from more precise optimization.

3.1.3.2 Recipes for Electron Beam Lithography and Deposition

In EBL, a polymer resist mask such as PMMA is used as an image layer for subsequent patterning via deposition or etching. The process for achieving < 100 nm features using EBL has been extensively documented by our lab in the past. Here we will focus just on those techniques were are essential for the fabrication of the tunnel junction based devices reported in Ch. 5 which require angled evaporation. For this, we employ a bilayer resist of PMGI/PMMA to obtain a large under-cut region with extended, free-hanging resist features. The recipe used is outlined in Tab. 3.4.

For angled evaporation of Al tunnel junctions, it is best practice to use relatively small angles to prevent significant warping of mask features due to edge variations in the exposed pattern. By carefully tuning the PMGI undercut, it is possible to selectively deposit material on the resist sidewall and prevent parasitic device components from being retained in the final pattern, as shown in 3.3. This however requires that the total undercut be just slightly more than is necessary to link opposite sides of bridged features, and the development method must be carefully controlled. Further,

PMGI/PMMA

1. Cleave 1um SiOx on highly doped p-type Si substrates into 1 cm square chips and clean using standard 3-bath water/acetone/isopropanol process.
 2. Using a standard PMMA/MMA bilayer, fabricate Ti/Au focusing/alignment makers in a 4x4 grid. This can be performed via dead-reckoning the working distance and using stage movements to repeatedly expose the chip without re-focusing. Liftoff as standard
 3. Spin PMGI SF8 (Kayaku brand) at 2.5krpm for 60s. Bake on a hotplate covered with a glass dish at 175C for 30m. Such high temperatures and longer bake times help to set the developer rate in step 6.c.
 4. Spin PMMA 940K A4 (Kayaku brand) at 4krpm for 60s. Bake on a hotplate covered with a glass dish at 170-175C for 3-5m.
 5. Mount samples for EBL using silver paint and clips in the SEM. Base dose for patterning > 400 nm features is $260 \mu\text{C cm}^{-2}$, to be increased to $\approx 500 \mu\text{C cm}^{-2}$ for < 100 nm features. Inner structures are written at 300 pA at 500X to 4000X magnification, while wirebonding pads are written at 3 nA at minimum magnification. Z is kept as short as possible while achieving a 2 mm FOV for wirebonding layer, typically 8 mm.
 6. Develop immediately in a 4 path process consisting of:
 - (a) 1:3 MIBK:IPA at 25 °C for 60s with gentle stirring.
 - (b) Room temperature IPA plunge for 1-2s followed by immediate N₂ blow dry.
 - (c) MF319 at room temperature for 17.5s with gentle stirring.
 - (d) DI water soak for 5-10 seconds followed by immediate N₂ blow dry.
 Longer times in MF319 provides additional undercut at a rate of $\approx 15 \text{ nm s}^{-1}$.
 7. Load immediately for deposition. Samples should not be stored before evaporation.
 8. Evaporate metals as needed. Liftoff in a three bath process of 45 °C acetone for 5m followed by acetone spray from a syringe, 65 °C Remover PG for 10m, and room temperature acetone for 5m, followed by 30s each of ultrasonication in acetone and isopropanol.
-

Table 3.4: Recipe for EBL defined samples using a PMMA/PMGI process.

by patterning the entire device in a single lithographic layer, the wirebonding pads remain galvanically connected to both materials which form the junction, preventing parasitic junctions from being formed in the measurement leads. This process was carefully refined to produce superconducting wires with no parallel current paths across their length, such that a true single grounding point for the wire can be obtained in the experiments detailed in §5.1.1. In practice, this leads to extremely stringent procedures regarding the development of the PMGI layer, with just 1-2 second variations seeming to have an effect on sample yield. In future work requiring selective liftoff on the PMGI sidewall, it is highly recommended to either dilute the MF-319 developer in deionized water to slow the rate for undercut development, or refrigerate the developer to drop the reaction speed (or both). Dilution of similar developer chemistry to that used here has been reported as being successful with PMMA/PMGI bilayers [152] even when large undercuts are required.

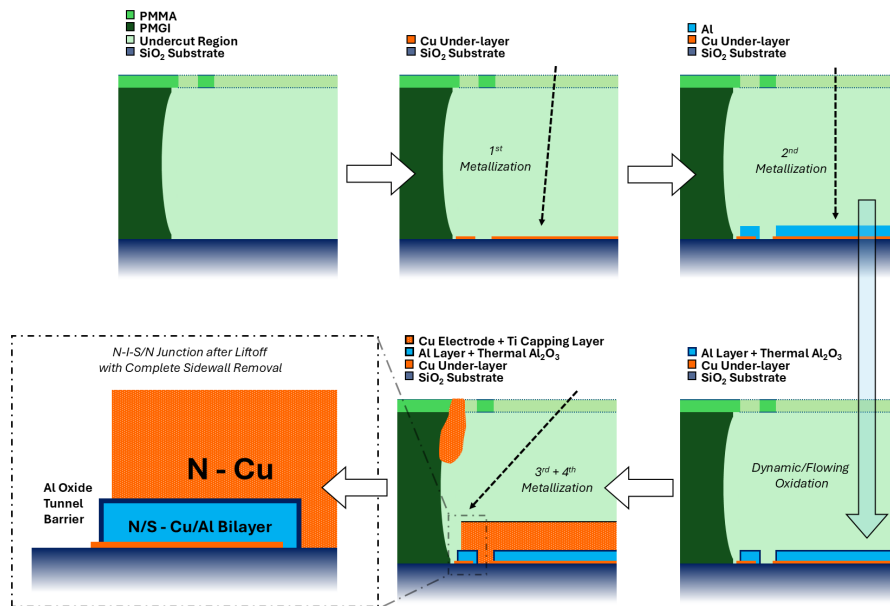


Figure 3.3: Fabrication process used to produce Cu/Al bilayers with normal metal Ti capped Cu tunnel junctions for non-local conductance measurements of a proximity effect bilayer, projected along the lateral cross section of the horizontal wires depicted in Fig. 5.1. Figure reproduced from the supplementary material of Ref. [151].

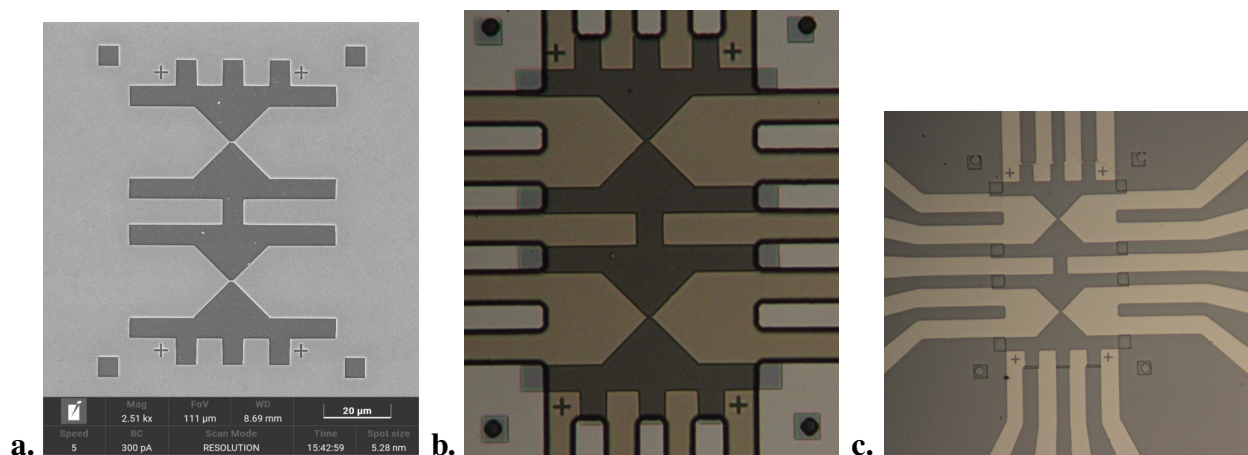


Figure 3.4: Process for fabrication of RIE defined devices with EBL patterning a.) Nanobridges after first etch. b.) Negative tone lithography soft-mask, using visual alignment to the corner squares. c.) Same device after a second etching to define the measurement leads.

3.1.3.3 Recipes for Electron Beam Lithography and Reactive Ion Etching

For devices where such feature sizes are transferred to an existing blanket film, EBL can be used in conjunction with an etching or milling process to obtain the desired resolution. Ar ion milling is typically not useful with electron-beam resists, as despite the neutral Ar beam, the soft-mask still becomes cross-linked to the degree it is rendered insoluble by ordinary liftoff chemicals. We can instead use reactive ion etching (RIE), in which the PMMA resist layer serves as a partially sacrificial mask to pattern a device. As this is positive-tone lithography however, the area to be written (and then removed via etching) can be excessively large, and must be performed in conjunction with a photo-lithographic method. The process is outlined in Fig. 3.4. As it turned out to be extremely difficult to perform alignment in EBL to etched features on Nb films, these devices were typically written in EBL first and then aligned for subsequent photolithography with the mask-aligner.

To perform the RIE, the SAMCO-10NR system available via NUFAB was used with a CH_4 etch

	CF ₄ Pressure (Pa)	CF ₄ Flow Rate (sccm)	Plasma Power (W)	Etch Time (s)
PMMA	30	89	200	75
S1813/nLOF	30	89	200	120

Table 3.5: Parameters for etching Nb films via the SAMCO RIE system using resist-masks spin-coated at 2krpm.

chemistry. In this process, PMMA was spun at 2krpm and prepared using the ordinary hot-plate procedure to serve as a sacrificial soft mask. For 40 nm Nb films on intrinsic/undoped Si substrates (as were provided by Rigetti Computing), the central region can be written at a low dose of $130 \mu\text{C cm}^{-2}$ due to the impact of the conducting Nb substrate. For larger features or features that are to be written on the bare etched Si of the substrate, a dose of $150 \mu\text{C cm}^{-2}$ is used. The resist is then developed in 1:3 MIBK:IPA developer for 60 s as usual.

Due to the poor etch selectivity of SF₆ for PMMA vs. Nb, only thin films of Nb can be patterned in this way before the PMMA resist mask is completely removed [153]. The selectivity can be improved by etching at higher pressures, allowing for etching of thicker films [154]. Parameters of the etching are presented in Tab. 3.5. Before and after running the chamber, it is cleaned by strong RIE etching using O₂ and SF₆ to prevent cross contamination from other users.

At 75s etching, more than 40 nm of Nb will be removed, with as much as a 20 nm over-etch into the Si substrate. The PMMA layer is still be present, albeit greatly thinned. Critically, the remaining Nb pattern is not reacted with the fluoride ions as it remains entirely protected by the resist softmask. Some lateral etching does seem to occur as the PMMA is thinned however, with thin wires losing approximately 100 nm in width over the 75 s etch. As a result, the original design must be compensated by 100 nm or more. Samples with extremely narrow feature sizes can also be formed due to this, down to the 10 nm scale. Removal of the residual resist can be performed by alternating soaks in heated PG Remover and Acetone, followed by ultrasonication, as was

formerly described. In future work, it may be interesting to consider alternating etches of O_2 and CF_4/SF_6 plasmas, as recent works have demonstrated that Nb removal predominantly takes place via reaction of the oxidized Nb_2O_5 [155].

3.2 Measurement and Control

As completed samples in this work have typically been imaged via optical and SEM microscopy before (and occasionally after) mounting onto specially designed sample holders used by our lab. For devices that are particularly sensitive to electrostatic discharge, care must be taken at all steps to work in a high humidity environment when handling completed samples, and to avoid static discharge via grounding wristbands and proper attire. With diligence, samples typically will not degrade or be lost due to shocks etc. from the experimental apparatus or its operator.

In this section, we explain further details of the experimental methods used to explore the results presented in the next two chapters of this work.

3.2.1 Sample Mounting

For samples produced on Si substrates, generally the best devices are selected by SEM imaging for tests and must be separated from sub-par/defective devices on the same chip. To do so, one can spin a thick layer of PMMA resist onto the wafer (without baking), and cleave it face up by nicking an edge of the chip with a razor blade to divide the wafer into smaller parts. The sample can then be cleared of debris by rinsing in acetone. With some practice, this is an efficient means for reducing the chip size without causing scratches due to removed pieces of the Si wafer.

With samples of the desired size obtained, devices are then mounted to our lab's custom 1" diameter printed circuit board (PCB) sample holders for wirebonding using Au-paint as can be seen in Fig.

3.1. These were designed to simplify the process of producing and bonding to sample mount, via use of non-magnetic pins/sockets produced by Cambion electronics. In practice, we have employed PCBs from OshPark (Au plated) and PCBWay (unplated, bare Cu). Plated PCBs appear to be preferable for stability and wirebonding, however we are uncertain as to their magnetic properties at low temperature. Wirebonding is performed via an Al wedge-bonding process using 5 mil Al wire via a refurbished Hybond manual wire-bonder. As the parameters of this system drift considerably over time, it must be calibrated between batches of samples to ensure consistent bonding. In general, bonding of Al to Nb is easiest, followed by bonding to Au and then to thick films of Al. Problems begin when attempting to bond to Cu films or devices consisting of Cu and Al. In those cases, the surface oxide growth limits the performance of the wedge-bonding process regardless of settings or operator skill, and the samples must be bonded within a few hours of exposure to air after deposition. A similar issue was found with Ag. Once bonded, Cu films remain fairly stable however, and the bonds hold for many days as the Cu-Al interface does not seem to degrade.

3.2.2 Conductance Measurements

In most transport studies performed by our group, a differential resistance measurement of dV/dI is performed via lock-in amplifier (LIA) techniques and 4-terminal resistance measurements. This is of course because, when using ohmic contacts, the local or non-local resistance of a sample is either finite or zero. For a superconductor specifically, most of the “action” in a resistance measurement is associated with a voltage on the order of Δ or larger, making it difficult to extract low energy spectroscopy of transport modes in the device due to the extremely small source currents required. To circumvent this, a tunneling barrier must be used, as this allows one to bias parts of the device at well defined voltages within a small current compliance. Practically, the biggest

limitation of this approach is that in tunnel junctions the resistance can become infinite, causing issues for voltage compliance among other challenges. As such, one performs instead a differential conductance measurement of dI/dV where true 4-terminal techniques are not possible. Typically the conductance of a tunnel junction is measured by just 2-terminals, one held at a fixed voltage and the other at ground, with the current flowing into ground measured by a sense resistance and voltmeter. Assuming that the lead resistance is considerably smaller than the junction resistance, this is acceptable as the voltage drop between the sample and the measurement apparatus is negligible compared to the voltage drop across the sample. In cases where voltage bias is applied to a low resistance sample, alternative techniques to those we describe here, such as using cold wire-wound series resistors or inductively coupled SQUIDS [156] should be used instead to precisely determine currents/conductances.

In past work by our group, low-noise current measurements using room-temperature electronics have generally been performed via AD549 electrometer op-amp based trans-impedance amplifiers (TIAs) with discrete off-board resistors. In this configuration, typically the TIA acts as a “virtual ground” point, used to drain current from a device generated by an applied voltage at an opposing lead. For non-local conductance measurements, or simultaneously biased local conductance measurements, a single virtual ground cannot always be used, and instead the TIA must be biased against the direct circuit ground. In this configuration, a bias is sourced from the TIA itself, and currents are measured across a sense resistor as a voltage offset with respect to the bias.

To perform our conductance measurements, we initially modified a set of AD549 based TIAs to allow for voltage biased operation. Bias voltages were generated by discrete summing circuits to combine a dc offset from a function generator with an ac modulation sourced by the oscillator output of a LIA, followed by a voltage divider to reduce the amplitude by 10,000:1 to a value

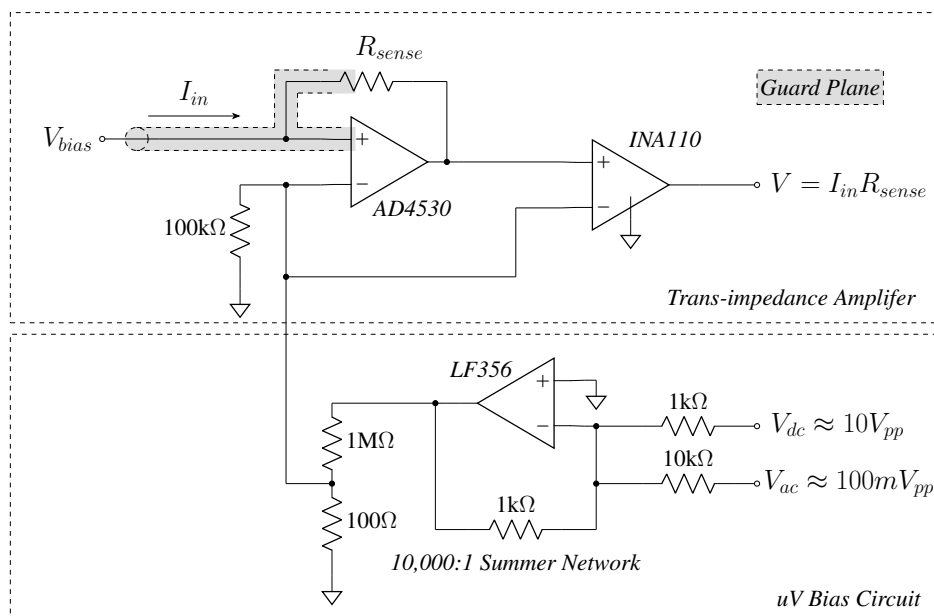


Figure 3.5: Circuit schematic for a voltage-biased transimpedance pre-amplifier for conductance measurements. A bias voltage is generated by a summing network which is applied to the non-inverting input of the AD4530 op-amp. This biases the current input which can be used to apply voltage across a junction with respect to the circuit ground. A guard plane, held at the same potential, is included on the circuit to prevent leakage currents from flowing away from the sense resistor.

suitable for spectroscopy of the superconducting gap of Al. To address the floating voltage of the sense resistor, a separate unity gain instrument amplifier was used, making the overall bias circuit slightly complex to setup and mechanically unstable in operation. All amplifiers are battery powered from within the shielded enclosure.

Based on these logistical and stability issues, and as the AD549 is no longer readily available from most vendors, we have constructed additional amplifiers for this purpose based on the “AD4530 Femtoampere Input Bias Current Electrometer Amplifier” from Analog Devices, which is available only in a surface mound device (SMD) package. In addition, a purpose built summing circuit for generating μV voltage biases within our μ -metal shielded enclosure was constructed for these

experiments. These circuits, schematically presented in Fig. 3.5, operates from $1 \times 10^3 \text{ V A}^{-1}$ up to a nominal gain of $1 \times 10^9 \text{ V A}^{-1}$ ($1 \text{ G}\Omega$ or 1 mV pA^{-1}), enabling local conductance measurements of Al based samples with 1 nS sensitivity. To prevent leakage current through/around the SMD based amplifier input, an integrated guard plane surrounds the op-amp and sense resistor at the same potential as is applied to the sample. Optionally, this can be extended to the input BNC connector by adjusting an internal jumper (not used in this work due to the present design of our break-out panels). The voltage offset is accounted for by an on-board INA110 instrument amplifier. As the AD4530 operates at a $\pm 5 \text{ V}$ rail to rail supply, there is a practical limit on the maximum measured current range from 5 mA at the lowest sensitivity and 5 nA at the highest. Considering only the dc response, following this circuit with a standard 6 1/2 digit ADC (HP 34401A etc.) at 100 mV scale, this performance enables measurements of currents down to $\approx 5 \text{ fA}$ precision.

One further consideration in operation/design of high-gain TIAs is that the bandwidth when using a large sense resistance becomes significantly degraded. Even worse, the exact cutoff frequency is determined by both the sense resistance and the sum of all parasitic capacitance across it, which can be hard to control. In the design used here, at a gain of $1 \times 10^9 \text{ V A}^{-1}$ the bandwidth is less than 50 Hz , and thus it appears that the parasitic capacitance may be larger than expected, on the order of 100 pF . For practical lock-in measurements, this limits the available frequency space for measurements at the highest gains.

Last, we should consider the types of 2-terminal measurements these devices enable. In lock-in conductance measurements, one must pick an experimentally relevant ac excitation to determine the total sensitivity. In most cases of interest for our lab this is determined by a known energy gap (which for Al we can take to be around $200 \mu\text{eV}$) or a known temperature depending broadening (recall that $23 \text{ mK} \Leftrightarrow 2 \mu\text{eV}$). Consider applying a $5 \mu\text{V}$ excitation to a device with a normal

state conductance comparable to the resistance quanta $G_0 = 2e^2/h \approx 38.7 \mu\text{S}$. This yields an ac current on the order of 200 pA. We can readily measure this at a gain of $1 \times 10^8 \text{ V A}^{-1}$ to obtain an LIA input signal on the scale of 20 mV (on low-noise the referred to input gain will be 25 for an SR124 at 20 mV scale). This will correspond to a $4 \mu\text{S/V}$ output to a 6 1/2 digit digital multi-meter, which gives a precision of better than 40 pS, or about one part per million of the normal state conductance. This sensitivity turns out to be essential for extracting weak conductance signals. For instance, the numbers above would allow us to confidently bound Γ for an Al device to just $10^{-6}\Delta$ or 20 neV. In practice however, one still ends up limited by thermal noise of the room temperature electronics eventually, but with sufficient averaging this can be avoided, making it possible to see small sub-gap or gap-edge features such as those caused by photon-assisted tunneling [97].

3.2.2.1 2+1 Terminal Quasiparticle Conductance Measurements

In Ch. 5 we will consider a variety of multi-junction measurements using two TIAs, which we will describe as either a 2+1 terminal measurement, or a current “injector-detector” experiment. Essentially, a single device can be biased to maintain fixed voltages across more than one probe lead, and multiple simultaneous conductance measurements made using LIAs to study both local and non-local effects. This is possible by using multiple dc+ac excitations with differing frequencies to “tag” the voltages. A schematic of the rack used in such a setup is shown in Fig. 3.6.

To explain the process concisely, one simultaneously applies voltages V_A and V_B modulated at frequencies f_A and f_B , using a pair of voltage sources, LIAs, summers, and TIAs. The resulting current is read by the TIA, and will be, for example:

$$I_B = \frac{dI_B}{dV_B} V_B + \frac{dI_A}{dV_B} V_A \equiv G_B V_B + G_{BA} V_A \quad (3.1)$$

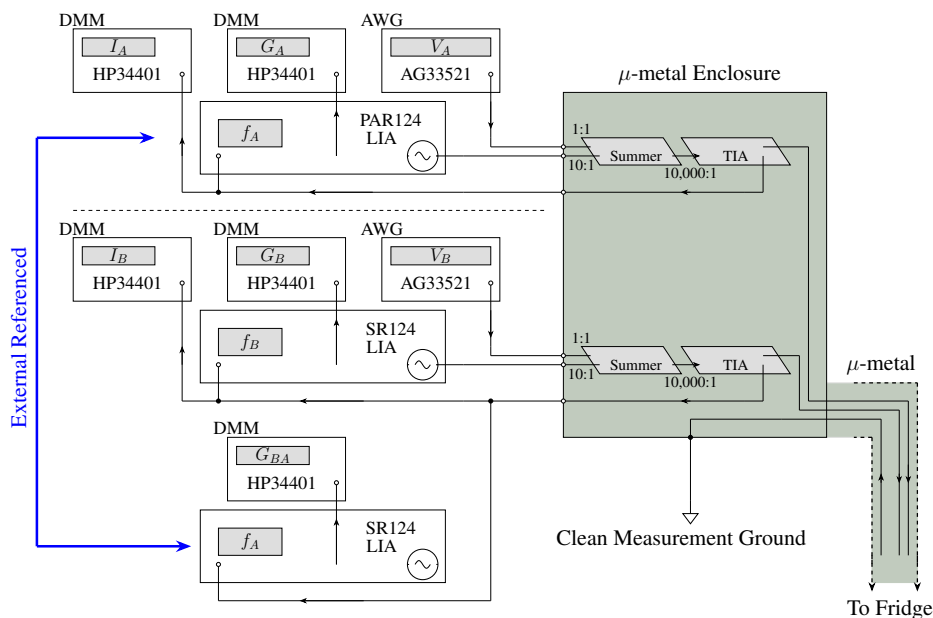


Figure 3.6: Equipment layout for a 2+1 terminal conductance measurement using three lock-ins with dual biases.

and vice versa. G_{BA} is thus taken from the component of the current I_B at the frequency f_B , and typically $G_{BA} \ll G_B$ for the experiments here. Thus we use a third LIA externally referenced f_A to find this additional conductance. Due to the aforementioned bandwidth limitations, it is best to choose these frequencies to be small and well spaced in the lower frequency register of the LIAs, typically ≤ 20 Hz. Phasing is performed against the voltage bias on the output of the TIA, as usually there is a small phase shift associated with the combination of summer and TIA circuits. This layout seems to have the additional benefit of protecting the ungrounded inputs of the sample from noise (and potentially even static shock) due to the large source resistance between the sample and the control electronics. One can, in principle, extend this to as many voltage probes as desired. However the phase space of the measurement becomes extremely large when doing this, and at large gains where the bandwidth and currents are small these experiments can become extremely time consuming. For the dual bias measurements reported in 5.2, the acquisition time was almost

2 days to obtain an understandable conductance heatmaps with nS precision.

3.2.2.2 $2+1(+1)$ Terminal Quasiparticle Chemical Potential Measurements

In principle, a similar technique can be used to measure the chemical potential directly, by allowing one of the NIS junctions to equilibrate with the quasiparticle chemical potential at zero net current. However, the type of voltage pre-amplifier used for voltage detection across an NIS junction is non-trivial. As the NIS junctions we will be considering for experiments are on the order of $10\text{ k}\Omega$ of normal state resistance or more, they can have critical currents in the pA range, which is considerably less than than the input-bias currents of any of our battery powered instrumentation amplifiers. A JFET preamplifier (such as the input pre-amplifier on an SR124 or SR2124) can be used successfully for such a voltage method, however the excess line-noise generated by using an unshielded pre-amplifier limits the usefulness for detecting small shifts in the chemical potential across a junction.

As a compromise, one can instead use ac-coupling and a low input bias current instrumentation amplifier such as the INA110 to measure the differential voltage change across a junction in response to a voltage bias elsewhere in the device. This is a slightly unusual arrangement, as what one measures is then dV_B/dV_A , i.e. a differential *gain/attenuation*. Assuming that that eV_B for an NIS junction does properly equilibrate to μ_{Q^*} , this can also be thought of as a differential measurement of the efficiency of non-equilibrium quasiparticle charge-generation. As we will see later, such measurements are sensitive to currently unexplained voltage contributions which break the expected symmetries of charge imbalance.

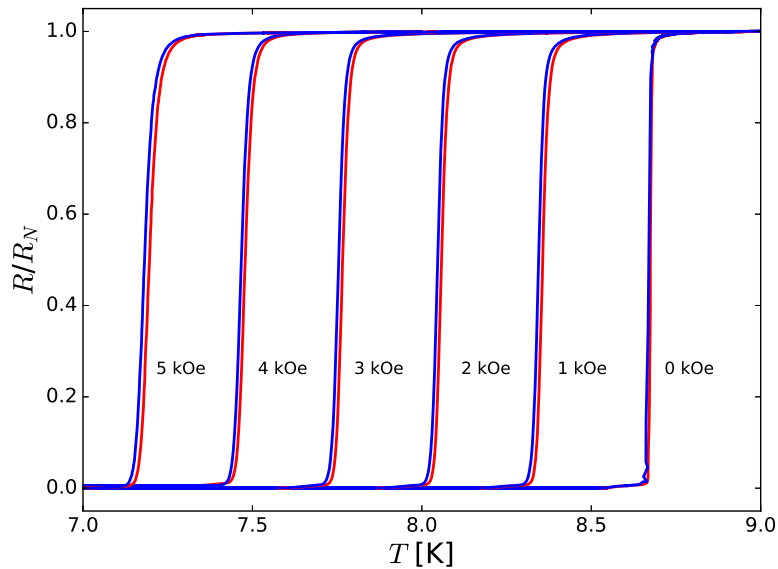


Figure 3.7: $R(T)$ for a 40 nm Nb film on a a- Al_2O_3 substrate, normalized to the normal state resistance R^N measured at various externally applied perpendicular fields obtained at a temperature sweep rate of $< 5\text{K/hr}$, demonstrating $\sim 20\text{ mK}$ of thermal hysteresis. Red/blue curves indicate data taken during warming/cooling. Figure reproduced from Ref. [157].

3.2.3 Feedback Controlled Measurements

In the studies described later in §4.1, we employ a feedback based resistance measurement which we will explain in detail here. When qualifying the resistive superconducting transition of a material, it is typical to measure $R(T)$ using a very slow sweep about T_c to capture the shape/width of the transition, as this informs on the quality of the material. To do this, the power to the sample heater of the fridge or probe must be ramped slowly such that the sample temperature changes at an approximately constant rate. As our probes are typically designed with a weak thermal link to 4K, there is a considerable time constant associated with this measurement. Fig. 3.7 shows examples of a superconducting transition measured on a 40 nm thick film on an a- Al_2O_3 substrate ramping both up and down in temperature at various magnetic fields at a rate of just 5 K/hr, there remains a

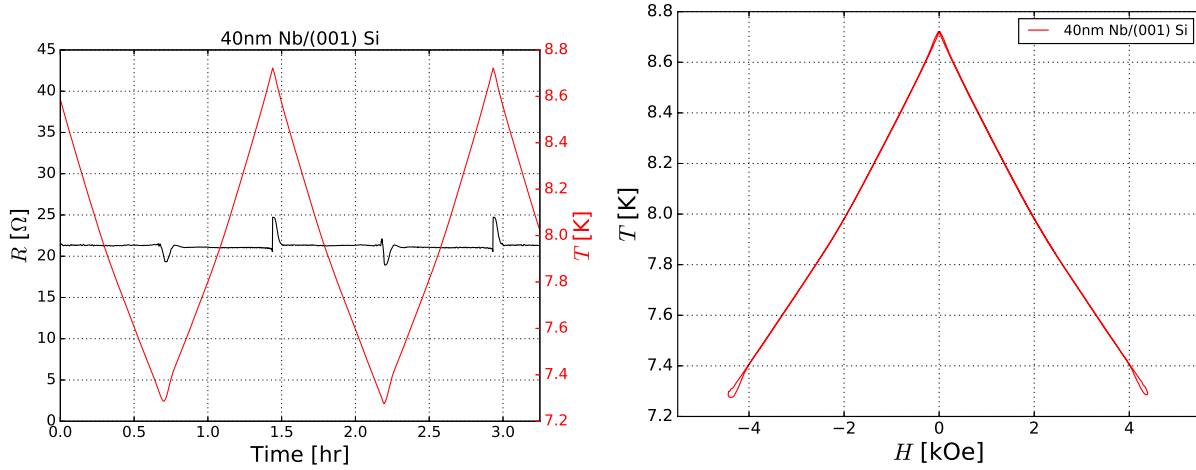


Figure 3.8: Left: Measured R and T_c for a 40 nm Nb film on (001) Si over two full traces over the field range presented in Fig. 3 of the main text. Right: Raw $T - H$ data for the same 40 nm Nb film. Figure reproduced from the supplementary material of Ref. [157].

thermal hysteresis similar in size to the transition width.

Instead, it often is better to perform the measurement at fixed resistance, using feedback. Using an Adler-Jackson ac resistance bridge [158] and lock-in amplifier techniques one can produce an analog signal suitable for a PID controller. This is possible as in a bridge configuration, one measures the deviation from a known resistance value, which can run positive or negative to serve as the error signal ΔR . To track the $T_c - H_{c2}$ phase boundary, one simply sets the bridge resistance to the midpoint of the resistance transition, and sweeps the field under feedback. This is demonstrated in Fig. 3.8, where the resistance of the sample is maintained to within 1% or better of the normal state resistance of that device over a range of ≈ 1.4 K. Although some hysteresis occurs in the raw measurement when dT_c/dt reverses direction, this data can be excluded by recording the error signal ΔR alongside the temperature. Ignoring this, T_c can be stabilized to within a few mK at temperatures around 10 K, of relevance for the study of Nb.

With an appropriately sensitive and field-independent thermometer, such feedback allows one to

track very small changes such as those due to the Little-Parks effect [159] or hysteretic transitions in magnetic superconductors [160]. Biasing to other points along the $R(T)$ curve, such as the top or bottom of the transition can then also reveal transition width broadening due to an applied magnetic field [161], and the method can be extended readily to other types of bias, such as recent measurements performed in our group by Max Wisne to track the critical current of multi-terminal devices. In the work presented in 4, an analog PID controller with a long, fixed integration time was used for feedback, however a digital Arduino based version continues to be developed by Prof. Chandrasekhar based on precision ADC/DAC chips we have attempted to implement, which might be preferable for improving the flexibility of the technique.

In Ch. 4, we will further interpret these measurements in terms of an effective zero temperature coherence length, defined as:

$$\xi_0 \equiv \sqrt{\left| \frac{dT_c}{dH} \frac{\Phi_0}{2\pi T_{c0}} \right|}. \quad (3.2)$$

This form follows from the expressions described earlier in §2.3.1, and can be calculated via numeric differentiation of the phase boundary. This has been done in the following studies via a second order Savitzky-Golay filter, which makes use of a boxcar averaging window to smooth the data somewhat, and is a highly useful visualization for cases where subtle curvature or transitions of the phase boundary are present. It is however also important that the thermometer used for the measurement is read via a smooth calibration, as even small jumps which occur as the result of linear interpolation can cause kinks in the phase boundary which are observable as acute jumps in the effective coherence length, occurring when $T_c(H)$ passes between interpolation points. Ideally, the resistance of the thermometer should be fit to a polynomial function with a large number of terms, such that interpolation errors are avoided. For the studies presented here, this was done via careful recalibration of our RuOx resistance thermometers to a known good thermometer.

CHAPTER 4

NIBIUM FILMS FOR SUPERCONDUCTIVITY DEVICES

4.1 Superconducting Phase Boundary Studies of Niobium Films used in Qubits

In this section, we consider a number of transport experiments taken during the investigation of differently prepared Nb films, which reveal the considerable differences that arise due to deposition conditions and substrate selection. As Nb films are typically sputtered, these samples were sourced from various labs within the SQMS collaboration. Primarily, we have examined films from Rigetti Computing prepared via High Power Impulse Magnetron Sputtering (HiPIMS) both with and without post annealing, as well as a set of samples produced at NIST by dc sputtering and some which have been grown at Northwestern University via pulsed laser deposition. An additional experimental survey was performed in collaboration with Carlos Torres of the Hersam group at Northwestern University, in which samples were fabricated from differently grown NIST sourced Nb films and wirebonded for measurements at the Northwestern Physical Property Measurement System (PPMS) facility. These are included for completeness.

These Nb films were processed into variously sized Hall bars, using the photolithography techniques explained in §3.1.2, and measured via our labs 1K probe inserted into a He dewar with a 3T superconducting magnet oriented perpendicular to the sample plane. The accuracy of the thermometer was verified both by calibration against a known good thermometer, and by measurements of a 99.99% pure Nb wire. For resistance measurements, ac-excitations of ≈ 100 nA were used at frequencies ≤ 200 Hz, and the lock-in set appropriate to minimize phase deflection through

the resistance transition of the samples.

4.1.1 Results on HiPIMS Nb Films

Substrate	d [nm]	T_{c0} [K]	ΔT_c [mK]	RRR
Si (001)	155	9.054	5	4.91
Si (001)	40	8.720	8	3.96
H:Si (111)	155	8.906	42	3.88
H:Si (111)	40	8.189	15	2.86
a-Al ₂ O ₃	40	8.789	11	5.23
c-Al ₂ O ₃	40	8.672	12	3.29
UHV a-Al ₂ O ₃	40	7.010 [†]	39 [†]	2.59 [†]

Table 4.1: Zero field transition properties of HiPIMS deposited films presented in this work. Values are reported under feedback. d is the film thickness of the film; T_{c0} is defined to be the temperature where $R = 50\%R^N$ at zero field; ΔT_c corresponds to the difference in temperature between the points with $R = 95\%R^N$ and $R = 5\%R^N$; and RRR is the ratio of the resistance at 300K and 10K. [†]Values reported along the $[1\bar{1}0]$ direction, see Fig. 4.5. Table modified from Ref. [157] to include H:Si (111) data.

First we will focus on the results for Nb films grown by Rigetti computing for SQMS, most of which are reported in our manuscript in Ref. [157]. Table 4.1 summarizes details of the transitions of the films included in that study, whose purpose was to explore the relationships between film preparation, substrate selection, and superconducting properties for films made using otherwise conventional preparation techniques optimized for high coherence time qubits.

4.1.1.1 HiPIMS Nb on Si

In the case of Si substrates, Nb films were prepared both on intrinsically doped (001) oriented Si and hydrogen-passivated (111) oriented Si (hereby labeled ‘H:Si (111)’), the latter of which were not included in Ref. [157] but will be considered here. While (001) oriented Si is commonly used in fabrication of qubits due to its compatibility with semiconductor technology, the H:Si (111)

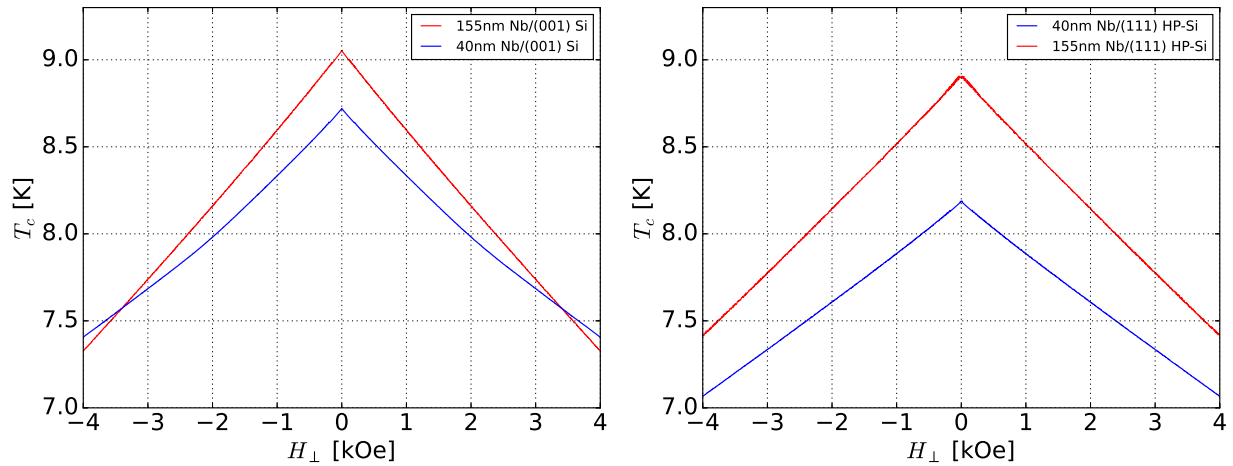


Figure 4.1: $H - T$ Phase boundaries of Nb on Si films demonstrating both T_c suppression and modified positive curvature of the phase boundary. The left panel corresponds to HiPIMS deposited Nb on untreated (001) oriented Si substrates, and the right panel corresponds to HiPIMS deposited Nb on Hydrogen passivated 111 oriented Si substrates (denoted H:Si (111)). Figure partially reproduced from Ref. [157] for the Nb/(001) data only.

treated silicon substrates were considered as a means of producing atomically flat Si substrates onto which it was hoped Nb could be grown epitaxially.

In Fig. 4.1, differences in the phase boundary due to film thickness are shown for both the 155 and 40 nm Nb films grown on both of the Si substrate types. The positive curvature seen in the phase boundaries of these devices, which is most evident in the 40 nm Nb on Si (001) trace, was unexpected via GL theory which predicts a linear suppression of T_c near zero field, but as will be seen in subsequent results, turns out to be common feature for as-deposited Nb films. The overall magnitude of T_{c0} is suppressed by both film thickness and in correspondence with reduction of RRR, as expected from similar reports related to the dimensional crossover of the properties of ultrathin Nb films [162]. As a result, films grown on H:Si (111) substrates exhibit a much larger thickness dependent suppression of T_c of 717 mK, along with an overall suppression of T_c likely due to different conditions during the deposition which produced excessive contamination of these

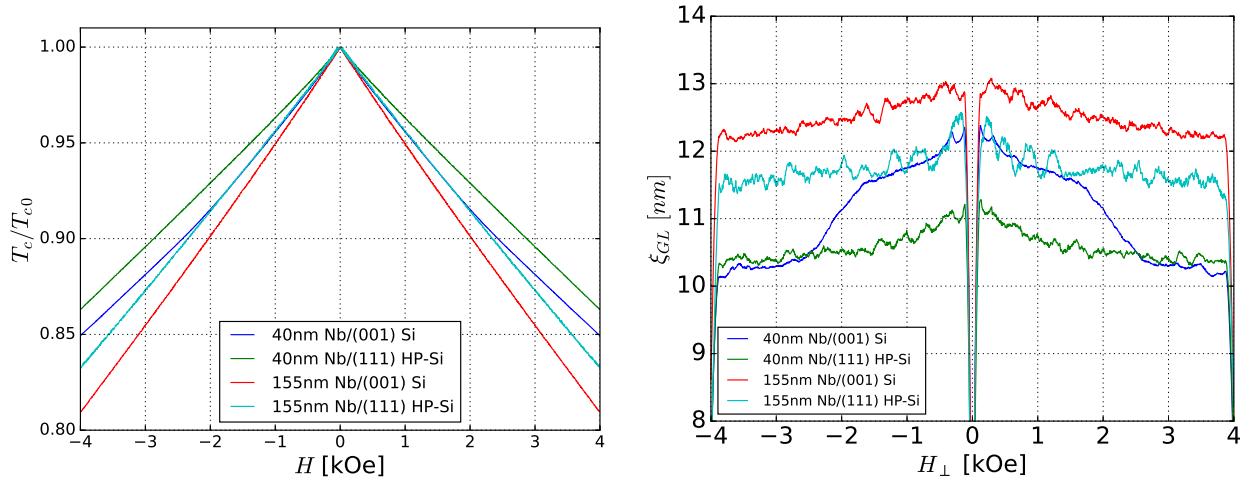


Figure 4.2: Left: $T_c(H)$ normalized by $T_c(0)$ for four differently prepared Nb films on Si substrates. The magnitude of the slope is proportional to ξ^2 , allowing a visual identification of the variation in coherence lengths of the films. Right: Numerically extracted coherence lengths as a function of field. Note that the variation in noise is largely relevant to the quality of the PID control used for each run, which is sensitive to gain and other experimental parameters, and only appears under numerical differentiation but cannot be seen in the primary dataset. The Nb (001) data also appears in the supplementary material of Ref. [157].

films. Conversely, a much smaller curvature is seen in the phase boundary of the H:Si (111) films than in Si (001) grown films.

To isolate individual changes of ξ and T_c , both a normalized plotting of the phase boundary of these four samples, as well as a numerically calculated values of the coherence length of the films as a function of field, are shown in Fig. 4.2. For both representations, there is a clear correspondence in slope between the 40nm (001) film and the 40nm H:Si (111) film in the regime above 2.5kG. Interestingly the suppression in $T_c(H = 0)$ and of ξ do not directly track with one another, with ξ being generally larger in the 40 nm (001) grown films than in the 155nm H:SI (111) films. It is also noteworthy that the reduction in ξ for the H:Si (111) films is of a similar overall magnitude to that of the (001) grown films, despite having substantially lower T_c values. Interpreting these results in the context of disorder is also difficult, as the magnitude of ξ (or of T_c) and the positive

curvature of these measurements do not track well with RRR, nor does RRR track well with the transition width ΔT_c . In fact, we see that RRR in particular is a poor method for sorting Nb films prepared by these methods. This leads naturally to the suspicion that the bulk transport properties of the film in the normal state are dictated by resistance at the grain boundaries which do not play into determining the superconducting properties within Nb grains.

4.1.1.2 *HiPIMS Nb on Sapphire*

To understand the role of grain structure and epitaxy better, 40 nm thick films of Nb were also grown via HiPIMS on both a-plane sapphire (denoted Al_2O_3) with (110) crystal orientation; and c-plane Al_2O_3 with (006) orientation. These substrates have become the preferred choice for high quality resonators and qubits due to their low dielectric losses [163] and ability to form epitaxial films with Nb [164]. In addition, separate 40 nm thick films deposited on a- Al_2O_3 substrates were ultra-high vacuum (UHV) post-annealed at Northwestern. This UHV anneal was performed at $\approx 2 \times 10^{-10}$ Torr and 1000 °C for 30 minutes, and the resulting grain structures studied via Atomic Force Microscopy (AFM) by Carlos Torres as shown in Fig. 4.3.

Both the as-deposited and annealed samples show significant grain structure under AFM, with a pronounced enhancement in the grain size being seen under UHV annealing, especially for a- Al_2O_3 . This was initially hoped to yield epitaxial Nb with bulk-type properties. In a similar vein, X-ray characterization performed by Carlos Torres and Dr. Dominic Goronzy on films prepared from this batch showed a strong enhancement of film-substrate epitaxy and greatly reduced lattice expansion and film roughness [157]. These structural characterizations were thus all consistent with the production of highly crystalline Nb films with columnar grains extending vertically throughout the material from substrate to surface.

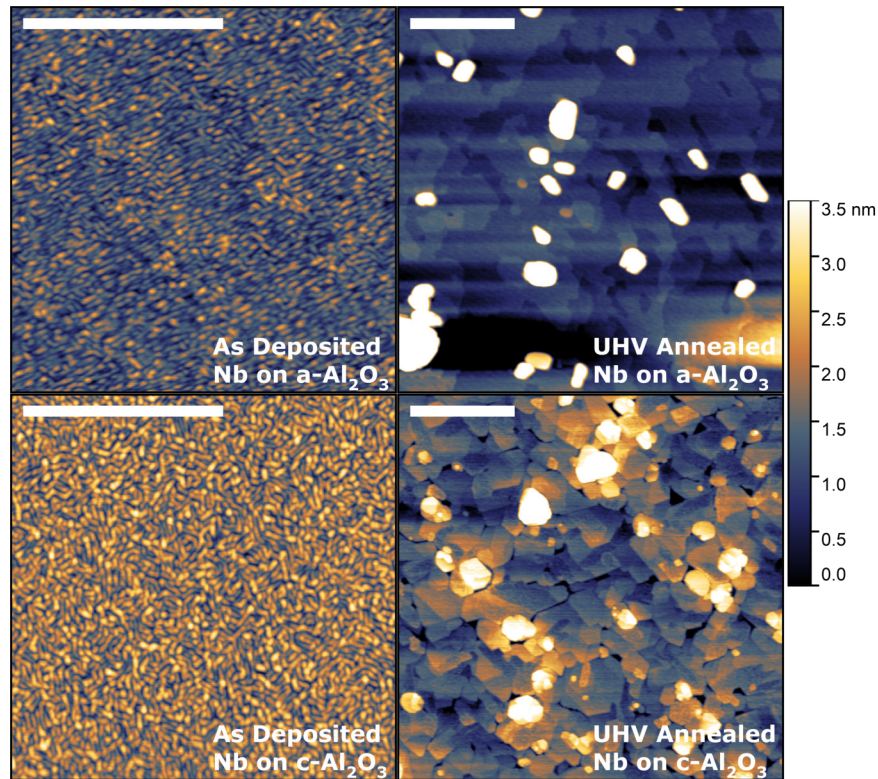


Figure 4.3: AFM micrographs of as deposited and UHV annealed 40 nm Nb films on a- and c- Al_2O_3 substrates. All scale bars are 500 nm. Figure reproduced from Ref. [157], with data courtesy of Carlos Torres.

Despite these positive indications, the as-deposited 40 nm films were found to be extremely similar to the corresponding Rigetti standard Si (001) grown film in terms of RRR, T_{c0} and ΔT_c , with Nb on c- Al_2O_3 being slightly *worse* on all accounts. The effective coherence length in a- Al_2O_3 is demonstrably higher than on c- Al_2O_3 , while the transition width broadening is considerably larger. The combination of these findings seems to suggest a difference in structural uniformity between the two, with a- Al_2O_3 grown films being generally cleaner (and hence, a larger ξ_0 and lower RRR) but with poorer uniformity such that the transition broadens under an applied field.

The annealing process performed on a- Al_2O_3 in this work unfortunately led to a precipitous drop in T_c and a large increase in the transition width, similar to what was seen on H:Si (111). Conversely,

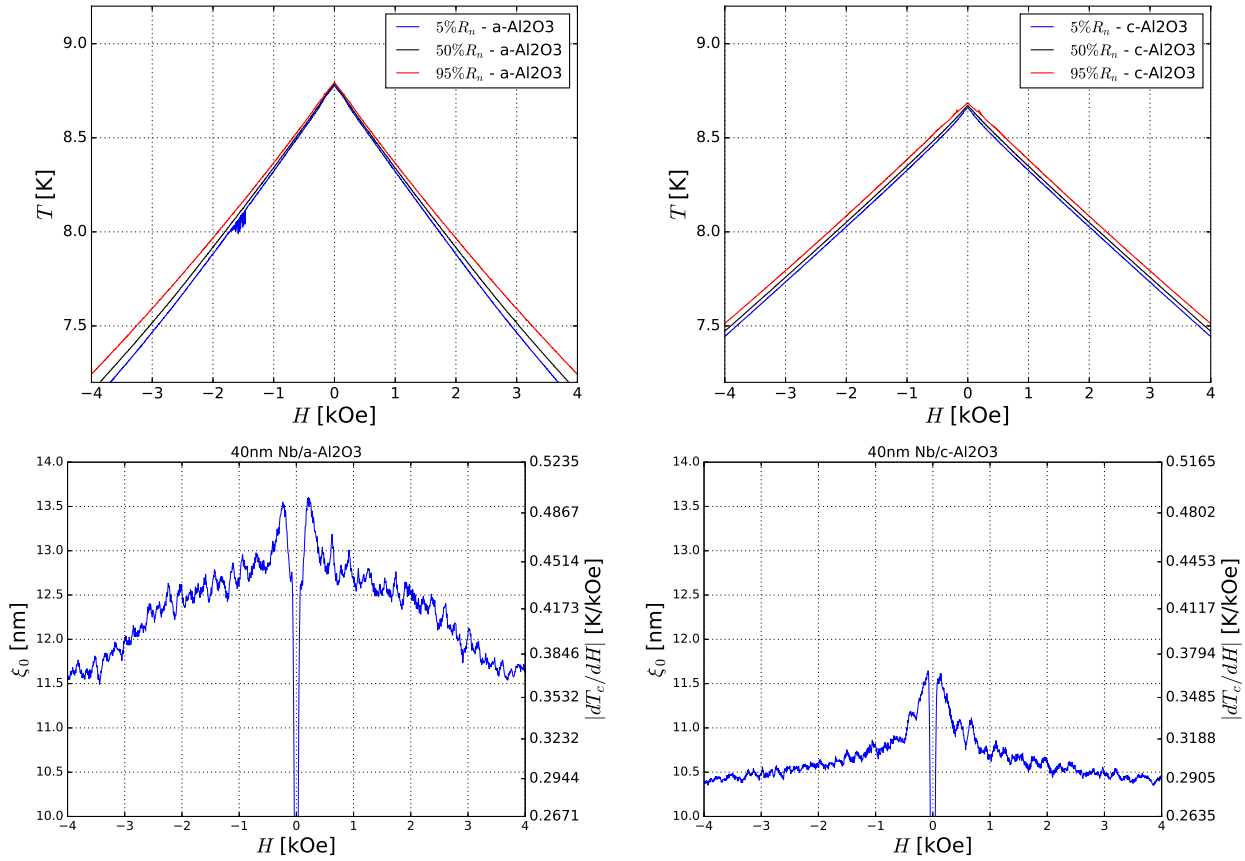


Figure 4.4: Top Left/Right: Temperature measured at fixed resistance values of 5%, 50%, and 95% of the normal state resistance for as deposited 40 nm Nb films on a-Al₂O₃ and c-Al₂O₃ substrates. Bottom Left/Right: Numerically extracted effective coherence lengths and their equivalent slopes $|dT_c/dH|$ for both devices calculated from the 50% R^N data. Figure reproduced from Ref. [157] and its supplementary material.

the increase in the uniformity and the removal of grain boundaries in that sample seems to have been associated with more GL type behavior, as analyzed in Fig. 4.5. The most likely explanation for this is the dissolution of the Nb native surface oxide into the recrystallized bulk of the film, rather than it being baked off into the UHV environment during annealing. Contamination of Nb with dissolved O is a well known issue, leading to increased type-II behavior and reduced T_c in bulk samples [165, 166]. The relaxation of the films could also indicate a high density of crystalline

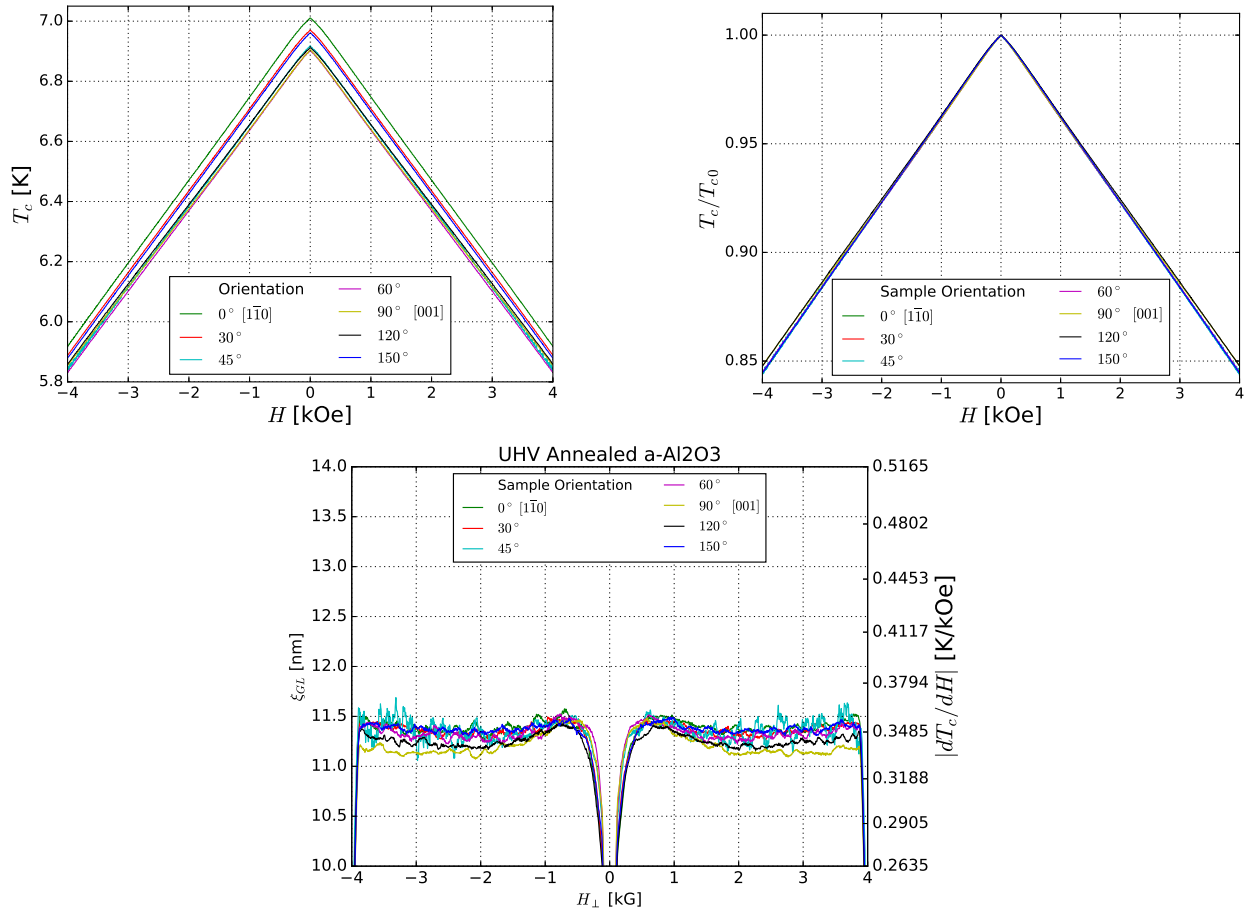


Figure 4.5: Raw (Top Left) and normalized (Top Right) T_c-H phase boundaries for UHV annealed 40 nm thick Nb films on a-Al₂O₃ substrates. Bottom: Numerically extracted effective coherence lengths and their equivalent slopes $|dT_c/dH|$ for all directions measured. Figure reproduced from Ref. [157] and its supplementary material.

dislocations, which are also thought to impact the superconducting properties of Nb [167].

As the annealed film was known to be largely epitaxial at the time of fabrication, we patterned it into a series of Hall-bars with well specified angles with respect to the crystalline axes. This was done using the same photolithography method as before, but with the mask carefully aligned to a known crystal orientation determined by XRD before fabrication. In this study, the only variation found was a small but systematic change in T_c , which when accounted for yielded nearly identical

values of ξ_0 for all orientations. As we will see later, this approach of subdividing a sputtered film into well oriented Hall bars tends to reveal similar macroscopic variations in even very clean samples, although the exact source is unknown. Based on this finding, we were able to propose that the curvature of the GL phase boundary itself is related to variations in properties of the grains of the film, while T_c and the magnitude of ξ_0 are most strongly impacted by diffuse impurities (such as O) or dislocations. In this model, $T_c(H)$ as determined by our method traces out a continuously changing distribution of superconducting grains. These will vary in ξ_0 and thus have different behaviors with respect to H leading to a general curvature of the phase boundary unless the film is highly uniform over the size of the device (regardless of its average cleanliness).

4.1.2 Results on DC Sputtered Nb Films on Si

In addition to the prior results studied on Rigetti deposited HiPIMS grown films, a pair of 40 nm thick dc-sputtered samples were prepared by labs at NIST for analysis by various groups at Northwestern. These films were grown on both 001 and H:Si (111) Si substrates at ambient temperatures. As dc-sputtering typically yields slower deposition rates and deposits material at lower ionization energies, it was thought this approach might better prevent the formation of a $\text{Nb}_x\text{Si}_{1-x}$ inter-metallic layer within the films. In Fig. 4.6 we present both the phase boundaries and extracted coherence lengths for these samples using the same procedures outlined for the HiPIMS devices and comparable sample geometry. For dc-sputtered films, we observe the highest T_c values of any 40 nm thick Nb films tested of 8.904 K and 8.858 K for H:Si (111) and Si (001) substrates respectively. There continues to be a general correspondence between T_c and ξ_0 between the samples, however ξ_0 here is not significantly greater than is seen in lower T_c films prepared by HiPIMS, suggesting this may be dimensionally limited for thinner films.

Similarly to the 001-Si grown film via HiPIMS, a distinct kink can be seen at low fields in the dc-

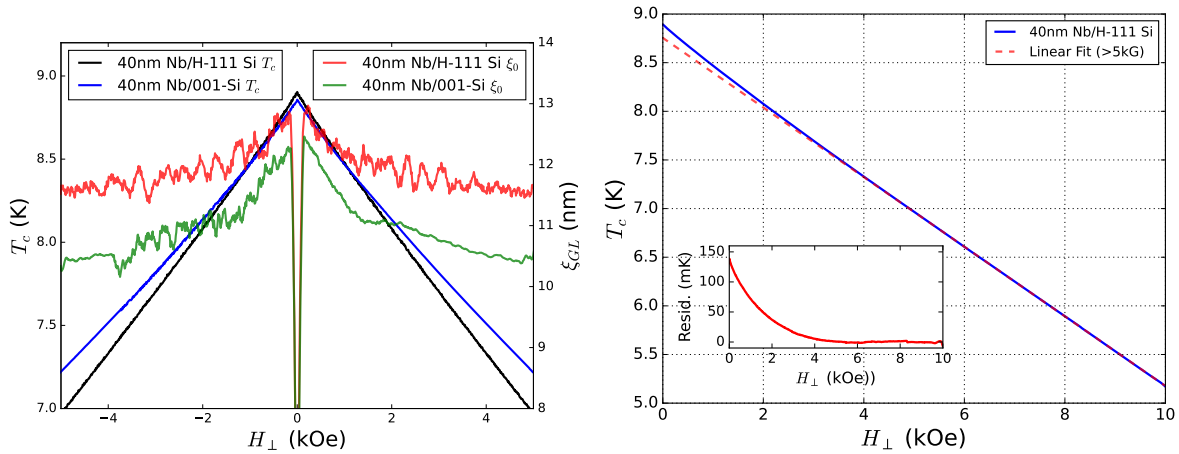


Figure 4.6: Left: Phase boundaries and extracted coherence lengths for dc-sputtered 40 nm Nb films on Si (001) and H:Si (111) substrates. Right: Extended phase boundary measurement of the H substrate to include data up to 10 kOe, showing high field linear behavior of the phase boundary. The inset panel shows a residual of a linear fit to the high field slope of the data.

sputtered film grown on Si (001), where the effective value of ξ_0 drops first near 1.5 kOe and then slowly follows a more ordinary downward trend to higher fields. Meanwhile in the H:Si (111) Si film, both the slope overall curvature of the phase boundary are very similar to the HiPIMS grown sample on α - Al_2O_3 , putting this sample among the highest quality films grown in this study. Given this, we attempted a further high-field measurement up to the limit of our magnet supply at 10 kOe to see if T_c could be traced down to its limit near $H_{c2}(T = 0)$, as is shown in the right panel of Fig. 4.6. Here, we find instead that the phase boundary is almost perfectly linear up to the limits of our measurement equipment.

Given these correspondences, especially the kinked behavior for the 001 device, it may be possible that the Si to Nb interface is contributing significantly to the transport at low fields, via a $\text{Nb}_x\text{Si}_{1-x}$ layer. On Si (001) grown devices this interface can be as thick as 8 nm [12], and thus may represent a large volume of the 40 nm film. Such inter-metallic layers are also seen on 111 grown Nb films [168], but were found to be only 1-2 nm thick. In both cases, gradients in the

concentration of Si across the interface are reported, with stoichiometric ranging from as low as NbSi_2 to as high as Nb_3Si . As Nb rich $\text{Nb}_x\text{Si}_{1-x}$ alloys are known to have transition temperatures as high as 17 K [169] (with some speculation that it could be as high as 25K under ideal conditions for the A15 stoichiometry Nb_3Si [170]) it may be possible that some of this effect is caused by the presence of a parallel higher T_c superconducting layer at the interface. Near the bulk Nb T_c , this layer might dominate the transport until a critical field range is reached, at which point the T_c of the alloy will drop below that of the bulk film and the resulting phase boundary switches from a low field to a high field trend. This reasoning is an extension to, rather than an alternative for, the contribution previously discussed in terms of granular disorder which is seen even in films on Al_2O_3 where such an inter-metallic region will not be present. Moreover, there may also be gradients in the impurity concentration (as is indeed thought to be the case, especially for O and H species which are commonly observed in the bulk of Nb superconducting films and devices [12]) which contribute similarly to the effect in small ways. In general the positive curvature of the phase boundary for a superconducting film may in fact be a universal property of clean but inhomogeneous polycrystalline superconducting films near zero field.

4.1.3 Results on PLD Grown Films on Al_2O_3

Substrate	Nb Orientation	d [nm]	T_{c0} [K]	ΔT_c [mK]	$R(T = 10K)[\Omega_{\square}]$	RRR
a- Al_2O_3	$[\bar{1}10]$	154	6.624	144	1.25	2.02
a- Al_2O_3	[001]	154	6.637	112	1.45	1.85

Table 4.2: Description and bulk transport properties of two studied directions for PLD grown Nb films.

In addition to sputtered films, several attempts were made to grow and measure Nb films grown via PLD by the Bedzyk group at Northwestern. This process is less well controlled than sputtering, but due to the elevated substrate temperatures it was hoped to be possible to obtain epitaxial Nb films

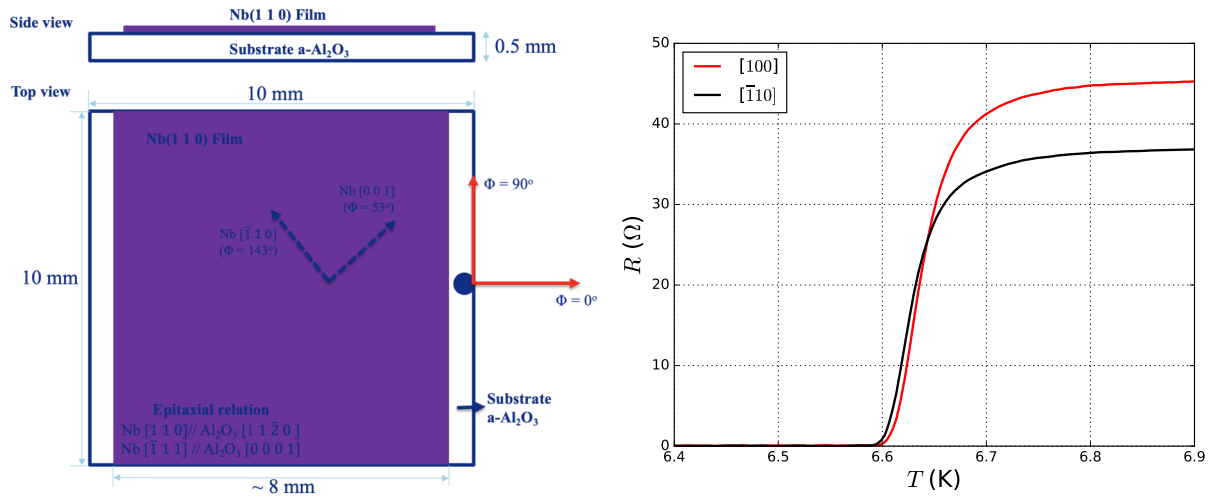


Figure 4.7: Left: Epitaxial relations for the studied low roughness PLD grown Nb on a-Al₂O₃. Diagram courtesy of Dr. K.V.L.V Narayanachari. Right: $R(T)$ traces for both studied directions along the Nb film.

via this method. However, after several rounds of experiment, the films studied via low temperature transport were consistently disordered, presumably by accidental oxygen incorporation during the high temperature growth. This may have been due to re-deposition of the surface oxides of the Nb target used for deposition, or another oxygen source within the growth chamber. Several of the early films tested were only loosely metallic, with at least one having a RRR < 1 and no superconductivity observed at 4 K. For comparison with the prior results, we will consider only the lowest overall surface roughness sample which was measured in this set of experiments, which was an oriented epitaxial film on a-Al₂O₃. The basic transport properties of these films are reported in Tab. 4.2, and the epitaxial relations are detailed in Fig. 4.7.

Several features are immediately evident from these properties. First, along the perpendicular directions of the film, there is $\approx 16\%$ higher resistivity along [100], but the transition is sharper and the T_c values are comparable. The degree of T_c suppression and low RRR corresponds to a

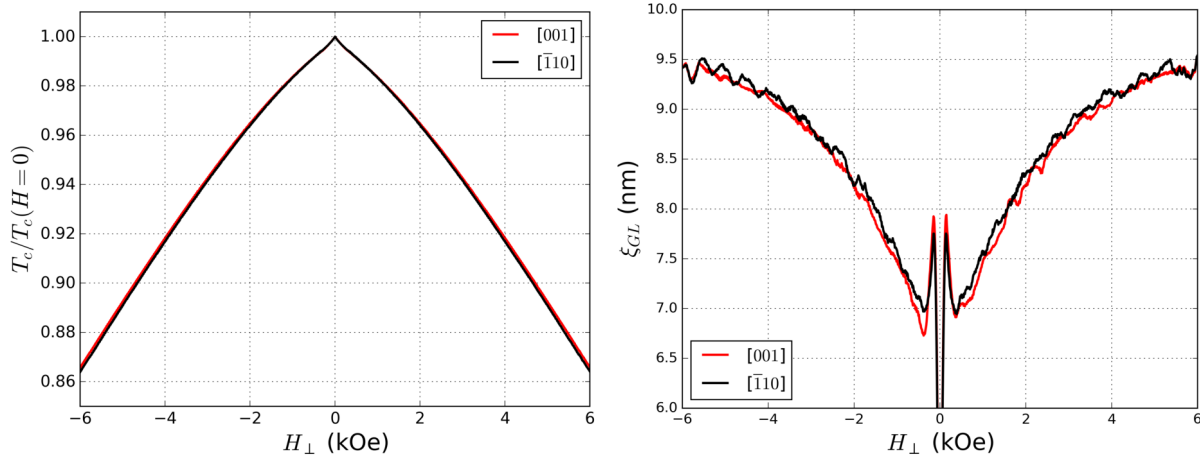


Figure 4.8: Left: $H - T$ phase boundary diagram for a PLD grown epitaxial Nb film along the principle crystallographic directions. Right: Corresponding effective coherence lengths extracted from the phase boundary.

very high oxygen content, on the order of 3 at.% [142]. The transitions in both Hall bars are also considerably broader than any other films studied, indicating strong disorder.

Under an applied field, the two devices behave remarkably similarly given the difference in resistivity between them. Fig. 4.8 shows the results of a feedback controlled phase boundary measurement. Surprisingly, there is a small region of positive curvature at very low fields, followed by a pronounced *negative* curvature for both devices which has not been seen in any other samples. Given the significant degree of oxygen induced disorder, it may be that these films are subject to considerable magnetic impurities which have been observed in the native surface oxides of Nb [171]. A possible explanation for the difference in resistivity between these orientations could be elongation of the grain boundaries along steps in the substrate due to the crystal miss-cut. A similarly prepared sample was measured via AFM before and after PLD of Nb is shown in Fig. 4.9 and showed such grain boundary alignment, along with a very large average grain size. Along the [100] direction, there will be a greater participation of grain boundaries to the resistance in the

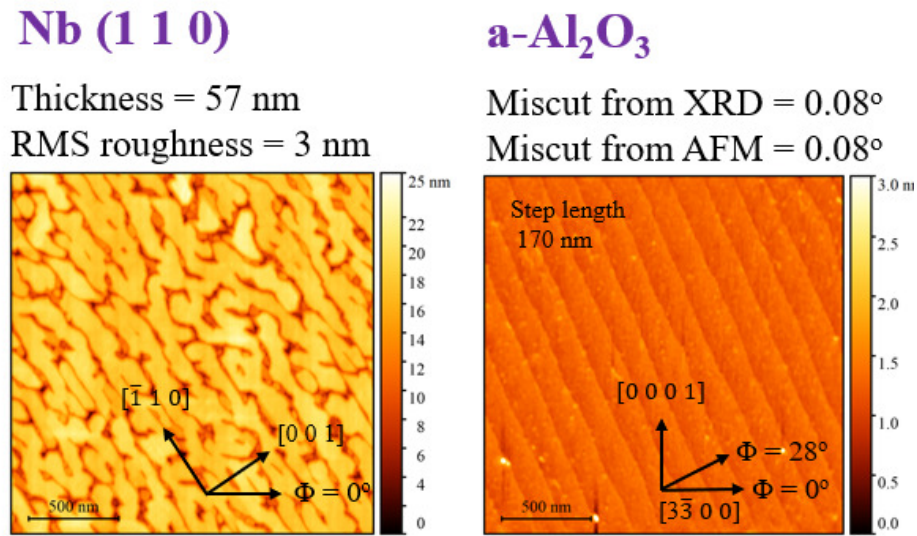


Figure 4.9: AFM Mapping of a PLD grown Nb film on a-Al₂O₃ and its underlying substrate. Figure courtesy of Dr. K.V.L.V Narayanachari.

normal state due to this structural anisotropy. This may not appear as an anisotropy in the superconductivity, as the bulk oxygen impurities are more isotropic and dominate the T_c suppression, and thus demonstrates that changes in RRR measured via transport in some cases do not meaningfully translate to changes in the behavior of the superconductivity.

4.2 PPMS Studies of High Temperature Nb Films Grown on Al₂O₃

Based on the result of our phase boundary measurements and other structural characterizations, additional 90 nm thick samples grown on a-Al₂O₃ substrates by DC sputtering at NIST at room/ambient temperature (abbreviated ‘RT’) or at a high temperature of 500 C (abbreviated ‘HT’). The as received wafers were cleaved and annealed to various temperatures by Carlos Torres in an ultra high vacuum chamber at Northwestern to re-crystallize the films and enhance the existing film-substrate epitaxy. Subsequently, the samples were patterned into angled Hall bar arrays as was done for the annealed HiPIMS grown sample examined in §4.1.1.2 using photolithography and

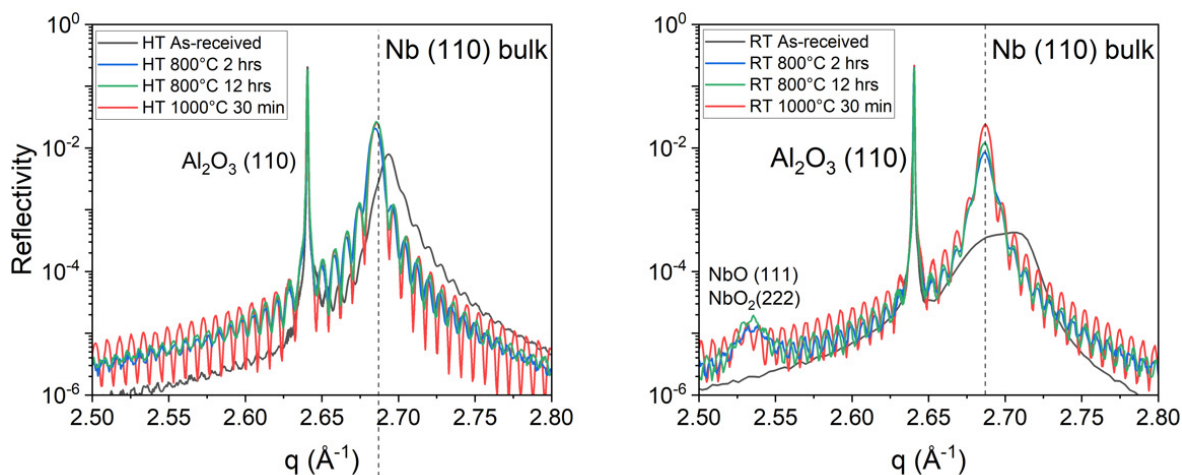


Figure 4.10: XRD measurements of HT and RT Nb samples on a- Al_2O_3 samples subject to various post-annealing conditions in UHV. Annealing of the films was seen to relax the position of the Nb (110) peak to its bulk value in both the HT and RT films, and improved strength of the fringes seen in the diffraction patterns. Figure courtesy of Dr. Dominic Goronzy.

Ar milling. Rather than perform a full phase boundary analysis for this large volume of samples, several of the treated samples were selected and wirebonded for measurements in the PPMS system via their automatic dc-transport. This included the as received RT and HT films, as well as HT deposited films which were annealed either for a long time at a lower temperature (800 °C for 12 hours) or a shorter time at a higher temperature (1000 °C for 0.5 hours).

Fig. 4.10 shows XRD measurements for the full set of films before patterning into Hall bars. The relaxation of the Nb (110) peak seen under all annealing processes was thought to be an indication of relaxed compressive strain in the films and improved film-substrate epitaxy. This was hoped to have a positive impact on the superconducting properties, however the issue of the NbO_x native oxide layer remained a concern. In principle, the surface oxide during annealing can either release into the chamber or become dissolved into the bulk of the Nb which will suppress superconductivity rapidly. Similarly, film relaxation could indicate the formation of additional dislocations within

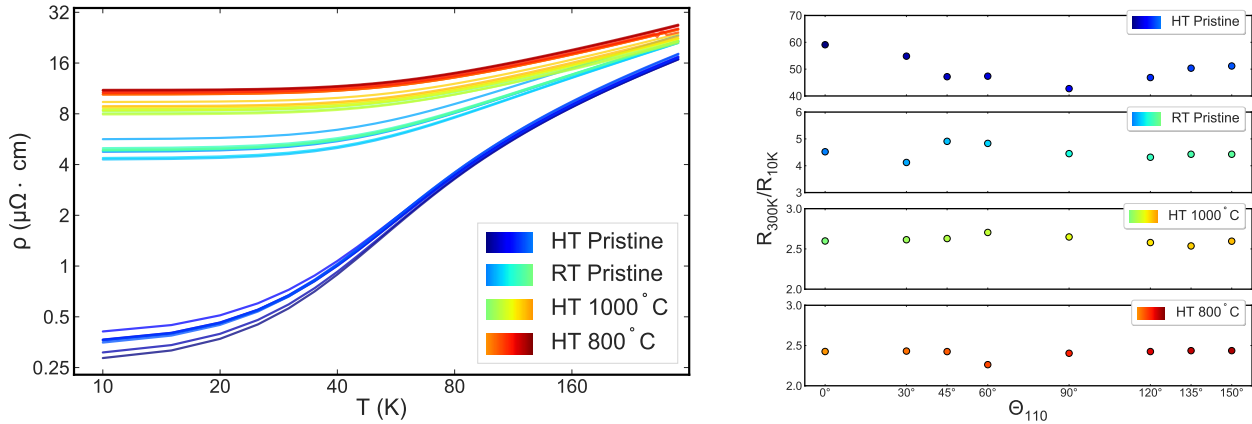


Figure 4.11: Left: Resistivity as a function of temperature measured for all devices. The color mapping for each traces corresponds to the sample type and angle θ_{110} with respect to the measured Nb [110] direction on the surface of the sample. Right: Resistance ratio between room temperature and the measured value at 10 K, obtained from the data in the left panel.

the Nb itself which will also impact the transport properties of the samples.

We first considered the effect of annealing and deposition temperature on the metallic quality of the films. Fig 4.11 shows the measured resistivity as a function of temperature for all directions along the 4 samples above T_c . Overall, the HT deposited sample in its pristine state is of the highest quality, with the RT deposited and annealed films having substantially higher resistance values at all temperatures. This discrepancy is enhanced by the large RRR (which we again take as the resistance ratio between room temperature and 10 K) seen only in the pristine high temperature deposited film, which takes values of between 40 and 60. No clear systematic dependence is seen in these resistivity or RRR values as a function of angle, which suggests that the films themselves contain sample specific disorder unrelated to the epitaxy of the film.

Superconducting transition temperatures were then determined via slower measurements of the resistance about T_c for all measured devices. These results are shown in Fig. 4.12. Between the pristine films, a relatively minor difference in the T_c values can be seen, while annealing causes

substantial degradation. Here it becomes clear that the 1000 °C for 0.5 h annealing condition is actually less detrimental to T_c than the longer 800 °C for 12 h condition despite having a much larger structural impact as seen by XRD. Conversely the transitions in the pristine samples are considerably broader than those in the annealed samples, with almost all pristine measurements showing a pronounced tail at the bottom of the transition. Additionally, if we consider the overall scatter of the transitions measured for each treatment, we see that the HT 1000C annealing process gives very inconsistent values for T_c while for the HT 800C process the T_c values are tightly centered.

Finally, the samples were measured under an applied perpendicular field H_{\perp} to obtain H_{c2} for each sample at 4.2 K, as shown in Fig. 4.13. This is, in principle, related to the slope of the phase boundary, but in taking the value at only a single point and at finite temperature one would not be able to cleanly ascertain a measurement for ξ_0 and so this comparison will be avoided. For these measurements, no field was applied during cooling, and then the field was swept slowly up to 30 kOe at fixed temperature. Again, the HT pristine treatment produces the lowest critical field value, corresponding to a cleaner film with a larger coherence length. The RT pristine film has both the broadest transitions and largest H_{c2} value, characteristic of a considerable suppression in the coherence length for this material compared to the HT film. The differences between the in field transitions for the annealed films are relatively minor, although a considerable “foot” is present in both which is not seen in the pristine HT film. Finally, one can clearly observe a degree of magnetoresistance is present in most of the data, especially in the HT Pristine sample where an unsaturated linear magnetoresistance is seen for in the normal state up to 30 kOe.

Taking these findings into consideration, it is possible to draw several addition conclusions about the various defects at play in sputtered Nb films on a- Al_2O_3 from those made in §4.1.1.2. Firstly,

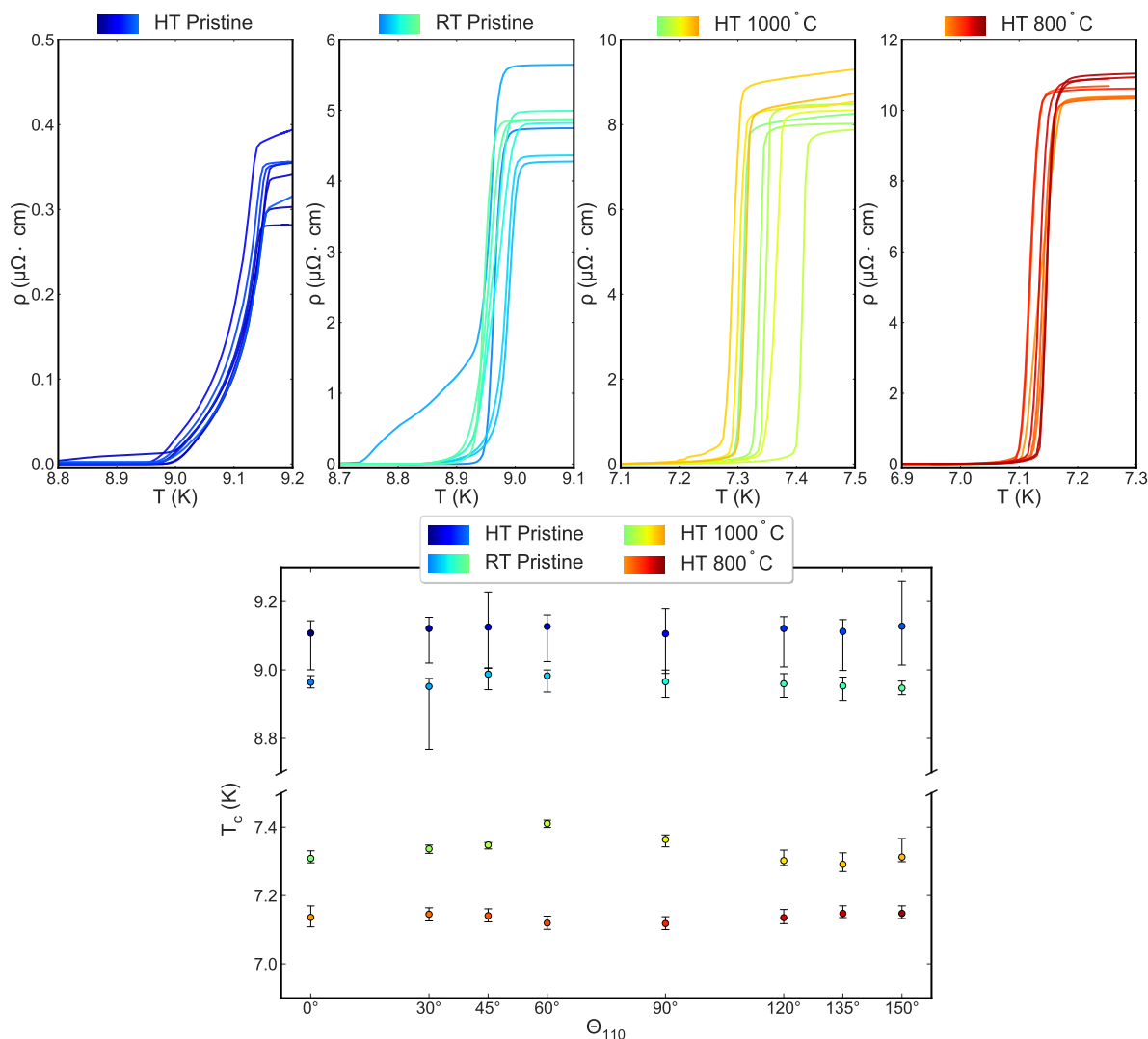


Figure 4.12: Top: Resistivity as a function of temperature about the superconducting transition. Bottom: T_c values determined from the midpoint of the transition where $R = 50\%R^N$. The error-bars additionally indicate the top and bottom of the transition according to the temperatures of where $R = 95\%R^N$ and $R = 5\%R^N$ respectively.

there is a clear and direct benefit to high temperature *deposition* conditions during sputtering, which cannot be replicated after the fact. Initially, we can determine from XRD that the HT pristine film is considerably more crystalline than its RT counterpart, which is substantially more

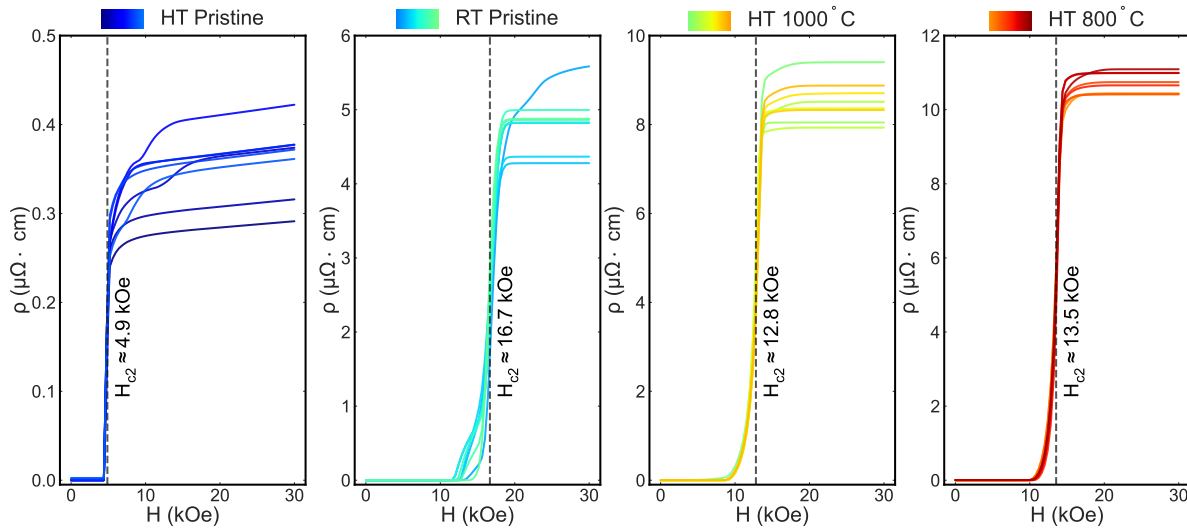


Figure 4.13: Resistivity as a function of field through the superconducting transition, measured at 4.2 K after zero field cooling. Values of H_{c2} are taken to be the value where the resistivity reached half of the normal state resistance at 30 kOe, averaged over the entire data set for each sample condition and are thus approximate.

amorphous. This translates into an enhanced RRR, the highest observed in any films we have studied for this work, as well as very high T_c values consistent with bulk Nb with an oxygen content of less than 0.13% [142]. Even then, the broadness of the transitions found in $R(T)$ indicates some inhomogeneity throughout the device, possibly in the cross section of the film due to gradation in the oxygen content or crystalline quality of the film, based on its general uniformity across the wafer. Room temperature deposition yields similar values for T_c , but considerably worse metallic behavior in the normal state at room temperature, and a large variation in the behavior under applied magnetic fields. One possibility would be that room temperature deposition yields roughly the same oxygen doping as high temperature deposition, but with substantially reduced grain sizes or an amorphous character. This is borne out by a broadened peak under XRD, high T_c despite a low RRR, and a large critical field which could be the result of dimensional limiting of the coherence length of the film by grain boundaries.

Secondly, the role of annealing even in UHV is two fold: annealing drives the surface oxide into the bulk and causes the formation of additional defects via relaxation of the film. This can be seen most clearly from the T_c suppression and increase in resistivity for both samples as these are broadly consistent with an oxygen concentration of about 2% [142]. The Hall bars annealed at 800 °C for 12 h are demonstrably more uniform in their transport properties within the plane than any other set of samples, and show the sharpest fringes under XRD. This tells us that the films started from a high purity, inhomogeneous source, and during annealing become heavily doped by incorporation of oxygen into the bulk while relaxing into a highly uniform crystalline state.

We can also note that there is a considerable disparity between qualitative assessments of the room temperature resistivity or structural characterizations made by techniques such as XRD and the eventual superconductivity of the Nb film. At 300 K, the resistivity of all samples studied lie within a factor of 2, and the XRD patterns for the annealed films seem to indicate lesser structural disorder than in the pristine films. Nevertheless, there are considerable differences between the four datasets when measuring their transport behavior at ^4He experimental temperatures with or without the application of a large magnetic field. Even at these temperatures, a single measurement is not well correlated with all superconducting phenomena. For instance, the T_c of the films do not track well with H_{c2} between the two pristine samples, nor with the RRR, indicating that multiple mechanisms are impacting the thermodynamics of the superconducting phase boundary in this case. This may also explain why there are no clear trends with regard to the orientation of the Hall bars with respect to the Nb lattice. As such, material characterization or straightforward $R(T)$ measurements alone are not a quality substitute for a wider study of the superconducting phenomenology when making assessments about the preparation and treatment of Nb films.

As a last point, we may note that even for the pristine HT deposition, there is considerable evidence

in these results to indicate that DC sputtering yields an inhomogeneous film, even when the overall quality of the material is quite good. The transition temperatures seen in those samples approach what has been observed for bulk Nb samples in the low O concentration limit [142], however H_{c2} in extremely high purity bulk Nb crystals (where RRR can exceed 2000) has been reported to be less than 3 kOe [165]. Based on this, we can conclude firmly that even under the highest quality conditions available at the moment, Nb films produced by DC sputtering are far from optimal superconductors.

CHAPTER 5

QUASIPARTICLE TRANSPORT STUDIES

As discussed, in state of the art qubits, control lines and capacitors are most commonly fabricated from Nb while their Josephson junctions consist of oxidized Al added via a secondary lithographic step. To return to the topic of quasiparticles in quantum devices, in this chapter we consider experiments on non-equilibrium quasiparticles in Al, rather than Nb, for the following reasons.

The first is simply that the form of the argument outlined in §2.1.2 is for interactions between the quasiparticles and the qubit due to tunneling across the Josephson element only, which occurs only over a short range about the tunnel barrier. As such, components of the qubit which are far from the junction contribute only indirectly via the generation rate for non-equilibrium quasiparticles which might diffuse towards the junction, and are less immediately impactful. In fact, it has been seen that the size of the gap in the outer regions of the device does not contribute greatly to decoherence when considering pair breaking of high energy phonons [172] which could be generated due to impacts with cosmic rays [85]. Similarly, it has been seen that essentially all quasiparticle based decoherence due to direct absorption of photons occurs in the Al leads contacting the junction itself, which act like antennas [173]. This latter observation agrees with the expectation that quasiparticles in the “macroscopic” parts of the qubit should be shielded from their environment by screening, and that all electromagnetic fields are at their strongest immediately across the tunnel junction itself where the dimensions are much smaller. Finally, as the gap in Al is an order of magnitude smaller than Nb, the thermal quasiparticle population will be highest there also, and their lifetimes should be longer.

The second matter is merely technical, as we will be using NIS junctions to generate non-equilibrium quasiparticles and thus require a robust oxide layer to serve as the tunnel barrier. Attempts to fabricate devices of the type explored in this chapter with Nb (rather than Al) consistently yielded ohmic contacts. This would proximitize the Nb sample volume by allowing quasiparticles to “leak” out into the normal leads, limiting the lifetime of the non-equilibrium states. As the native oxide of Al is self limiting and highly insulating, Al is the de-facto material for generating high quality NIS junctions (to the extent it is can also be used as the normal metal side of the NIS junction for experiments performed at $T > 2$ K). To complete these junctions, we use thick Cu electrodes as the normal metal. This choice is fairly standard, as it is a nonmagnetic metal which does not superconduct at any temperature, and does not form undesired intermetallic compounds with Al (as is now well known for Al–Au interfaces which our group is well familiar with).

5.1 Observations of Quasiparticles via Charge Imbalance

To proceed into our findings, we will first take the case of charge imbalance and its modification in the presence of a source of inelastic scattering via a disordered normal metal. This forms the basis for our results in Ref. [151], where charge imbalance is primarily considered as it gives a more quantitative means of understanding quasiparticle relaxation at mK temperatures. We then expand beyond the published findings associated with this work, to explore the chemical potential model for quasiparticle charge imbalance. In the following sections, we will then supplement this discussion with qualitative findings on the energy imbalance in those and similar devices, and consider experiments on similar, but miniaturized, NIS devices which can be operated in high magnetic fields. There, we will focus broadly on non-equilibrium energy mode imbalance; previously unreported non-local transport features; and the impact of applied in plane magnetic fields and large supercurrent biases.

Device	Metal	Angle	d (nm)	P (Torr)	Rate ($\text{\AA}/\text{s}$)
Control	Al	0°	20.1	4.0×10^{-7}	1.1
	Cu	-35°	80.2	6.0×10^{-7}	3.0
	Ti	-35°	5.0	2.8×10^{-7}	0.5
Bilayer	Cu	-10°	3.0	1.0×10^{-6}	1.2
	Al	0°	20.0	6.9×10^{-7}	1.05
	Cu	-35°	80.1	1.0×10^{-6}	3.0
	Ti	-35°	5.0	4.0×10^{-7}	0.8

Table 5.1: Deposition conditions during device fabrication for control and proximity effect bilayer devices. d is the thickness determined during deposition, and P is the recorded peak pressure during evaporation. A dynamic oxidation was performed subsequent to the first Al layer at ≈ 100 mTorr for 15 minutes, and all devices were fabricated in the ‘JoeTek’ chamber. Table reproduced from the supplementary material of Ref. [151].

5.1.1 Enhancement of Quasiparticle Relaxation in Cu/Al Bilayers

In our first devices for Ref. [157], arrays of NIS junctions were defined using the PMGI/PMMA methods described in §3.1.3.2, onto either a pure Al or proximity effect Cu/Al bilayer wire. Some details of the fabrication are presented in Tab. 5.1, which also describes the general process notes for the fabrication of most devices in this chapter.

In this study, we aimed to consider the transport dynamics of quasiparticles in the presence of a proximity coupled normal metal. This has been an experimental topic of interest, partly due to recent works on the encapsulation of superconductors and qubits with noble metals which prevents potentially unwanted oxide growth [174, 175, 176]. In a similar vein, the proximity effect has also been considered for so-called quasiparticle ‘traps’, where suppression of the superconducting gap due to the proximity effect [107] can cause quasiparticles to relax in energy below the gap within the rest of the device [177, 15, 178]. The design and performance of such traps requires a very careful understanding of the quasiparticle dynamics [179, 180, 181, 182], however at the moment relatively little is known experimentally about the direct impact of proximity to a normal metal on

the diffusion and relaxation of quasiparticles, which leads naturally to our study.

As discussed in §2.2.4, injection of electrons from a normal metal leads to both energy and charge mode non-equilibrium in a superconductor. This has served as the experimental basis for many tests of the BCS model over the last 50 years, where NIS (and/or SIS) junctions have been used to study non-equilibrium superconductivity. The basic premise for most experiments of this type is to use multiple junctions to inject and detect non-equilibrium quasiparticles and their impact of the superconducting gap, which can be either enhanced [94] or suppressed [183] from its equilibrium value. In older works, such measurements were made near T_c , where the lifetimes of these excitations diverge per Eq. 2.84 and Eq. 2.83. At temperatures far below T_c both τ_{Q^*} and τ_Δ will be reduced, just as the density of thermal quasiparticles is reduced in this limit, requiring much higher sensitivity and careful consideration of the experimental design.

Due to the short lifetimes of the quasiparticle excitation modes at mK temperatures, the corresponding transport length-scales are also much shorter than those studied in many of the older experiments, requiring nano-lithography to access. For instance, the charge imbalance mode lifetime can be associated with a length scale for relaxation of the chemical potential which we will call the charge imbalance length and denote λ_{Q^*} . This is a property of the (renormalized) diffusion of charged quasiparticles, such that

$$\lambda_{Q^*}^2 = D(\epsilon_k)\tau_{Q^*} = \frac{|\epsilon_k|}{\sqrt{\epsilon_k^2 + \Delta^2}} \times D_N\tau_{Q^*}. \quad (5.1)$$

The first measurements of λ_{Q^*} in superconducting wires at mK temperatures NIS junctions were performed by Hübner et al. in 2010, which found charge imbalance lengths on the order of 2-4 μm in Al [184]. In this work, the authors constructed a useful model for the conductance between two junctions due to quasiparticle charge imbalance alone which we have adopted in our study of

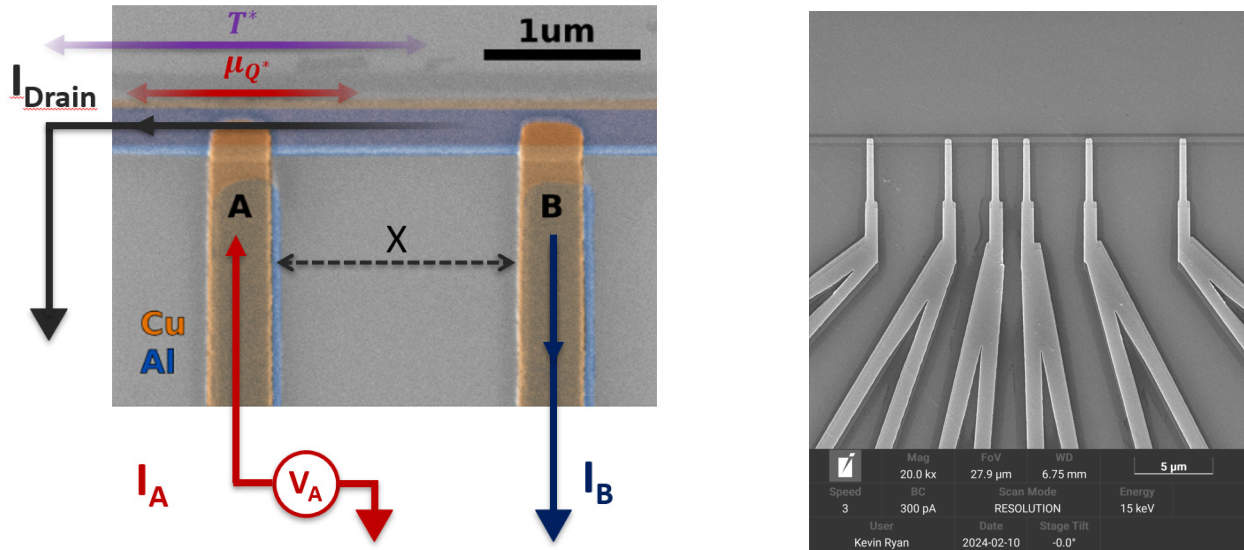


Figure 5.1: Left: Schematic of the non-local injector/detector scheme, using two TIA circuits as described in §3.2.2.1 to measure the nonlocal charge imbalance signal. During injection at junction A , both a finite μ_{Q^*} and elevated effective temperature T^* are generated throughout the superconducting wire via the diffusion of quasiparticles in both directions away from the injector. This relaxes and the resulting supercurrent is drained out to a ground on the side of the device opposite the detector junction B . The SEM micrograph used corresponds to the bilayer device, where one can see a slight extension of the Cu layer on the top of the wire, which is necessary to prevent shorting of the injector leads into the Cu of the bilayer. Right: Overview SEM micrograph of the spacing between six junctions arranged along a single Al wire. Each junction here has two leads used for diagnostics measurements only. Figure modified from Ref. [151].

proximity effect bilayers. More recently, other works have explored this approach for injection of spin-polarized quasiparticles and various other non-equilibrium transport effects [185, 186, 187, 188, 189].

Returning to our experiment, six NIS junctions were staggered with separations between $2\ \mu\text{m}$ and $6\ \mu\text{m}$ along a total length of $20\ \mu\text{m}$ on either a $20\ \text{nm}$ Al control device, or a $20\ \text{nm}/3\ \text{nm}$ Al/Cu bilayer, as shown in Fig. 5.1. The dimensions of the separately fabricated devices were matched as closely as possible so that they could be directly compared. These samples were wire-bonded via the standard process and measured in an Oxford MX-100 dilution refrigerator down to a base

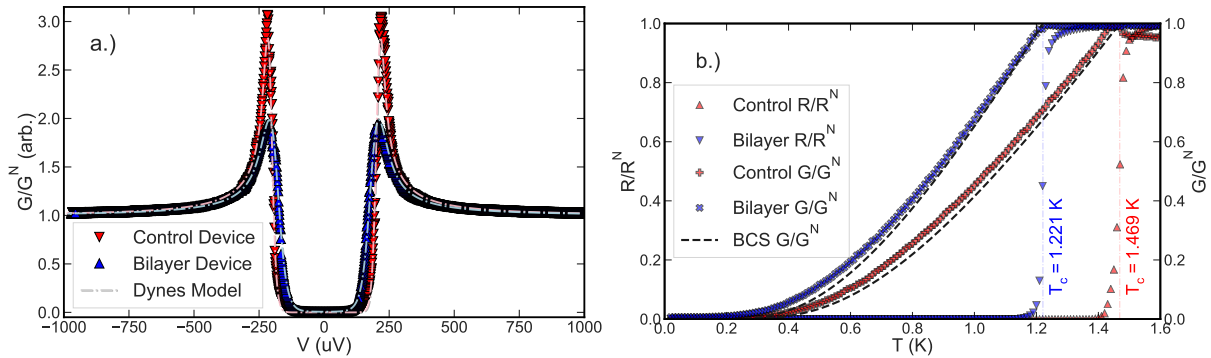


Figure 5.2: a.) Normalized local conductance and Dynes-type fits for two junctions, one from the control and one from the bilayer device, taken with identical measurement configurations at a bath temperature of 20.4 mK. *Fit parameters*— Control: $T_e = 101$ mK, $G^N = 202 \mu\text{S}$, $\Delta = 207 \mu\text{eV}$, and $\Gamma < 10^{-5} \Delta$. Bilayer: $T_e = 196$ mK, $G^N = 152 \mu\text{S}$, $\Delta = 189 \mu\text{eV}$, and $\Gamma < 0.6 \% \Delta$. b.) Resistance of the superconducting/bilayer wire, and conductance of their corresponding junctions normalized to their normal state conductance G_N at T_c . Also shown is the BCS expectation of the zero bias conductance. Figure reproduced from the supplementary material of Ref. [151].

temperature of 20 mK. The immediate role of the proximity effect was an expected reduction of T_c and Δ , which can be seen in both resistivity measurements of the wires and the conductance spectra of the NIS junctions, as shown in Fig. 5.2. The effect is consistent with the expected degree of gap suppression which occurs in superconductors with clean, transparent interfaces to a region of normal metal which can be determined by solution of the Usadel equations [107]. In this case, the T_c reduction of $\approx 17\%$ is slightly above expectation, but was thought to be due to a combination of lateral inhomogeneity of the wire due to the deliberate misalignment of the Cu and Al layers, and the thinning of the Al itself during oxidation. Fitting to the conductance of these devices to Eq. 2.68 revealed anomalously high effective electronic temperatures $T_e \approx 100$ mK in the control device. This was found to be even higher in the bilayer device, however in that case one does not expect a BCS like gap and the conductance broadening is more likely to be attributed to a gradient of the gap across the width of the wire (across the vertical overlap shown in the left

panel of Fig. 5.1), as in this model T_e should actually be that of the electron distribution in the Cu injectors. Attempts to constrain these fits to the measured temperature of the mixing chamber naturally leads to a heightened Γ parameter to account for the broadened conductance, however this was generally inconsistent with the height of the coherence peak maxima at $eV = \pm\Delta$ and with the subgap conductance. From this we are left to conclude that T_e is impacted by noise in this study, and cannot be extracted as a means for comparing changes in T^* . Despite this, we can still make strong conclusions about the quasiparticle dynamics via Q^* .

To compare the charge imbalance effect between devices, we employed the non-local conductance setup described in 3.2.2.1, with modified AD549 based TIAs to simultaneously bias an injector junction while detecting the *zero bias* conductance of the detector. In this, we employ a lock-in technique similar to that of Hübler et al. in Ref. [184], where a junction is held at the zero bias and detects the current due to quasiparticles tunneling out of the superconductor. Per Eq. 2.75 and Eq. 2.77, this will be the component due solely to charge imbalance. Using this face, Hübler et al. describe a differential conductance due to charge imbalance between an injector junction (labeled ‘A’) and detector junction (labeled ‘B’) as

$$\frac{dI_B}{dV_A} \equiv G_{BA} = g^*(eV_A)G_B^N G_A^N \frac{\rho_N \lambda_{Q^*}}{2A} e^{-X/\lambda_{Q^*}}. \quad (5.2)$$

The factors A and l are the cross sectional area and length of the central wire having a normal state resistance R^N . Terms G_A^N and G_B^N are the normal state local conductances of junctions A and B, while g^* is a dimensionless shape-function, roughly equal to the Heaviside function $\Theta(|eV_A| - \Delta)$ if one ignores thermal broadening [184]. This term will be a fitting function later in the text, but essentially accounts for the magnitude of spectral charge transferred into the quasiparticle density of states $g^* \approx q(E_k)N(E_k)/2eN_0$, due to the reciprocal nature of Eq. 2.61 and Eq. 2.49.

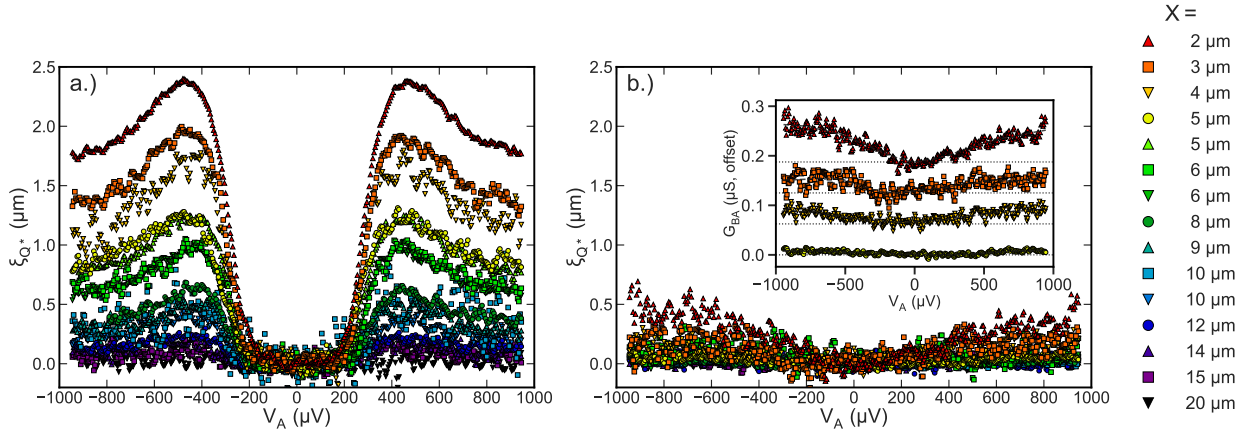


Figure 5.3: Quasiparticle conductance normalized as defined in Eq. 5.1.1 for different values of the length X between the injector and detector junctions, measured at 20.7 mK for both a.) the control and b.) bilayer device. The inset in b.) corresponds to the raw (offset) G_{BA} data measured in the bilayer device, which falls below the noise threshold for $X \geq 4$ μm . Note that repeated X values occur for certain combinations of junction pairs, and are reported for completeness. The legend is common to both plots. Figure reproduced from Ref. [151].

When providing a single drain to ground on the opposite side of the injector junction as shown in Fig. 5.1, this quasiparticle conductance is said to be non-local with respect to the injector. In practice, the only current that is actually drained is a supercurrent formed by the recombination of quasiparticles into pairs. As the critical current of these NIS junctions will be orders of magnitude smaller than that of the wire itself, this supercurrent is generally too small to affect the measurement (via modification of the h_T and h_L distributions in the kinetic equations) and one sees the same conductance regardless of which side of the wire is grounded.

By picking pairs of junctions with different separations X (taken to be between the midpoints of the junctions), the resulting conductance G_{BA} can be measured and traced out with respect to energy and position to determine the charge imbalance length. Such data for the control and bilayer device are shown in Fig. 5.3. Here, we have applied a normalization to the data to account for differences

in the junction conductance and device dimensions. This defines a new signal parameter

$$\xi_{Q^*}(eV_A) \equiv \frac{2l}{R^N} \frac{G_{BA}}{G_A^N G_B^N} = g^*(eV_A) \lambda_{Q^*} e^{-X/\lambda_{Q^*}} \quad (5.3)$$

which is merely a rescaling of λ_{Q^*} (with unit length) and should not be confused with any other physical property of the device such as the coherence length ξ_0 . These results demonstrated a large enhancement of the relaxation mechanism responsible for returning quasiparticle charge into the condensate due to proximity with the Cu underlayer, as seen by the order of magnitude reduction in ξ_{Q^*} for measurements taken at the same corresponding values of X . In the bilayer device, only a very weak charge imbalance signal is ever seen above the noise floor of $\xi_{Q^*} \approx 0.05 \mu\text{m}$.

To make the comparison quantitative, one can bin this data as a function of the injector bias (and therefore, E_k of the injected quasiparticles), and fit this for both g^* and λ_{Q^*} to obtain estimated values as reported in Fig. 5.4. The quality of fit in the control is fairly good, with λ_{Q^*} being in close agreement for similar thickness Al devices reported in the literature [184, 190]. In the bilayer, we obtains large error-bars for both fitting parameters, but characteristically λ_{Q^*} has been suppressed by about a factor of 2. This agrees generally with the approximate order of magnitude reduction in ξ_{Q^*} ($x = 2 \mu\text{m}$, which would be associated with a slightly larger factor of ≈ 3 reduction in λ_{Q^*}). Note that in both cases, the injector current below the gap is nominally zero and the model fits to the signal noise which causes λ_{Q^*} to become undefined over this regime.

From this, we can readily conclude that the proximity effect has a large impact on the quasiparticle transport in such a bilayer, associated with a dramatic increase in the inelastic scattering rate that leads to a reduced charge imbalance length. Before discussing the mechanism for this in more detail, we can consider what this implies for the dynamics of quasiparticles in this kind of system. Generically, by Eq. 5.1, inelastic scattering of quasiparticles down to the gap edge will not only

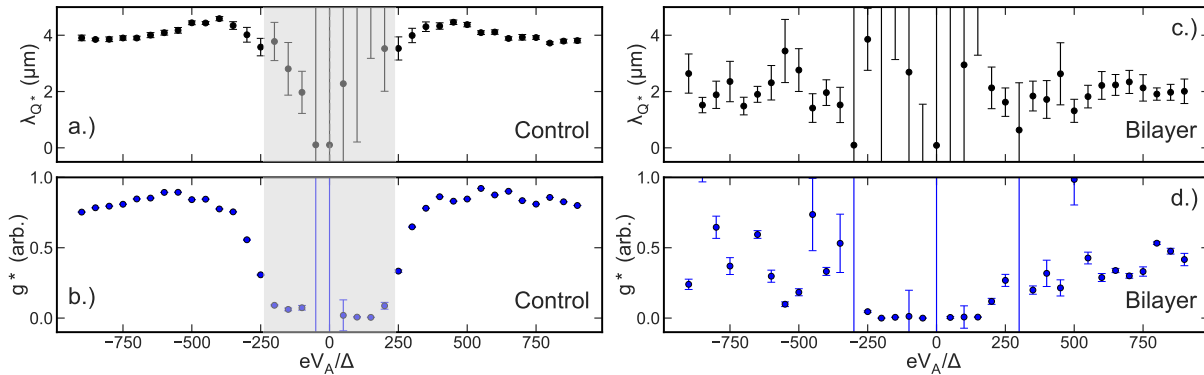


Figure 5.4: Results of fitting to data from both devices after binning ξ_{Q^*} by $50 \mu\text{V}$. Fitting was performed to Eq. 5.1.1 with g^* and λ_{Q^*} as independent parameters. Error-bars are propagated forward from both binning and fitting of the data. a.) and b.) graphs correspond to the control device, while c.) and d.) to the bilayer device. The gray region in a.) and b.) indicates energies where insufficient current I_A is injected to measure λ_{Q^*} . Figure reproduced from the supplementary material of Ref. [151].

cause them to lose charge, but slow down as their group velocity approaches zero. Consequently, the initially electron/hole like quasiparticles become neutral and diffuse more slowly after inelastic scattering. At higher temperatures, this can occur via scattering with thermal phonons, consistent with the Boltzmann picture from §2.2, but at low temperatures the inelastic relaxation will be very weak. This may be an issue as in the very clean metals desired for quantum experiments, the normal state diffusion constants can be very large leading to rapid transport of quasiparticles across the device. Without any inelastic relaxation, a high energy quasiparticle generated anywhere in a qubit might diffuse into the junction region leading to decoherence, but if it can relax inelastically first then the subsequent diffusion will be much slower. For this reason, one might consider engineering devices with a greater inelastic scattering rate, as we have done in this work, to help mitigate some of the quasiparticle induced decoherence in quantum devices without needed to necessarily trap or recombine them altogether.

	R_{\square}	w	d	l_{mfp}	D_N	$L_T^{20\text{mK}}$
Control	6.21 Ω	275 nm	20 nm	3.17 nm	21.5 cm ² s ⁻¹	906 nm
Bilayer	7.99 Ω	300 nm	23 nm	[†] 2.47 nm	[†] 16.7 cm ² s ⁻¹	[†] 799 nm

Table 5.2: Measured and Drude model calculated values for both control and bilayer devices, and device specific parameters. Here, w is the width of the wire, and d is the total thickness of the wire/bilayer for each device. For both devices, we estimate that $w \ll L_T^{20\text{mK}}$ (the Thouless length calculated from D_N for $T = 20\text{ mK}$) which indicates the wires to be generally 1D. [†]Approximate values for the bilayer calculated using the reported properties of Al alone. Table reproduced from the supplementary material of Ref. [151].

5.1.1.1 Estimating Inelastic Rates in Al and Cu Wires and Bilayers

To understand the inelastic scattering associated with these results, we can estimate the inelastic scattering rates at 20 mK based on normal state properties of the wires, which we determine above T_c as the resistivity of Al in our devices saturates well above this range. Using this, we can obtain the diffusion constant and thus the Thouless length $L_T = \sqrt{\hbar D_N / k_B T}$ to confirm that these devices are functionally 1D wires. Results of this analysis are reported in Tab. 5.2.

Making the assumption that quasiparticles with an energy $E_k \approx eV_A$ diffuse a length $\lambda_{Q^*}(D(E_k))$ in a time $\tau_{Q^*}(E_k)$ before relaxing all at once to the gap edge, we can first back out $\tau_{Q^*}(eV_A)$ for the control device to be

$$\tau_{Q^*}(V_A) \equiv \frac{\lambda_{Q^*}^2}{D_N} \frac{eV_A}{\sqrt{(eV_A)^2 - \Delta^2}}. \quad (5.4)$$

Using this, we can then choose to relate λ_{Q^*} to τ_E by Eq. 2.83, despite this being normally invoked for its accuracy near T_c . We do this both for lack of a formal theory appropriate to mK temperatures, and based on works by Pethick and Smith discussed in §2.2 in which the relaxation is explicitly ambiguous in origin when deriving this form [147]. Nevertheless, the exact prefactors relating τ_{Q^*} and τ_E are almost certainly on the order of unity, somewhat justifying the general rates we obtain, which are plotted on the right axis of Fig. 5.5.

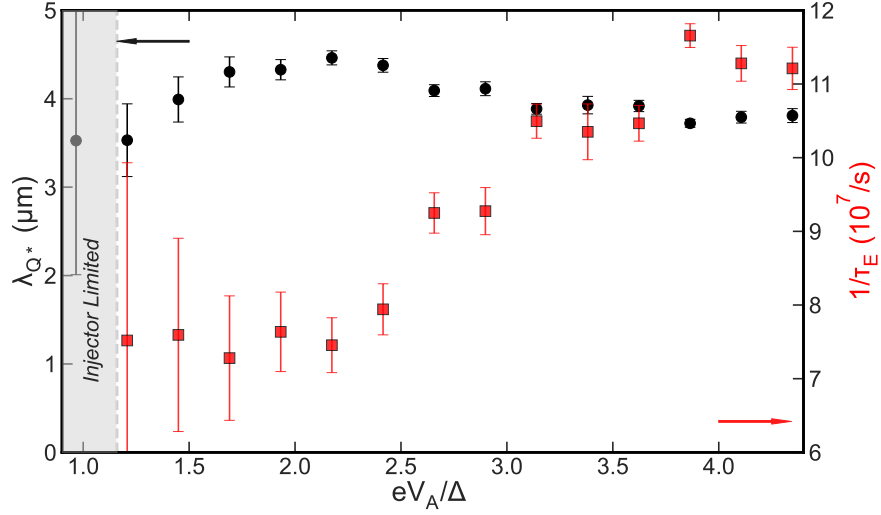


Figure 5.5: Charge imbalance length λ_{Q^*} (black circles) for the control device as a function of injector bias V_A , also shown in Fig. 5.4.a. Red squares show the corresponding τ_E values determined from λ_{Q^*} using Eq. 2.83 and Eq. 5.1, assuming an excitation energy of eV_A . Figure reproduced from Ref. [151].

In this description, we see that the inelastic relation rate picks up considerably for injection of quasiparticles at energies above 2.5Δ , and is generally on the order of $1 \times 10^8 \text{ s}^{-1}$. At the temperatures achieved in this experiment, it is known that electron-phonon scattering will have already fallen far below the bare inelastic electron-electron scattering rate for a 1D wire [191]

$$\frac{1}{\tau_{ee}} = \frac{1}{\pi^3} \frac{1}{\sqrt{2}} \frac{R_{\square}}{\hbar/e^2} \frac{D_N}{wL_T}. \quad (5.5)$$

Using the values estimated in Tab. 5.2 however, this is only on the order of $1 \times 10^5 \text{ s}^{-1}$ for the values relevant for our device, which is far too slow. Notably, this discrepancy cannot be accounted for by inserting an elevated temperature into our calculation of L_T , as this would require $T \gg T_c$ for electrons in the Al. To considering possible faster interactions due to small energy transfers which are not necessarily inelastic [192], we could instead estimate the Nyquist scattering rate [193] for

the control device

$$\frac{1}{\tau_N} = \left(\frac{1}{\sqrt{2}} \frac{R_{\square}}{\hbar/e^2} \frac{\sqrt{D_N^3}}{wL_T^2} \right)^{2/3}. \quad (5.6)$$

This comes out to a much better agreement, with a value of $3.4 \times 10^7 \text{ s}^{-1}$. While usually only considered for the dephasing of the electron wavefunction, this value is also close enough that the remaining factor of 2-3 could be accounted for by an elevated temperature. As such, we are uncertain if this is a coincidence, but feel strongly that electron-electron interactions play a considerable role in quasiparticle transport at these temperatures.

The scale of these relaxation rates also indicates a possible explanation for the further enhancement of quasiparticle relaxation in the bilayer device. Looking to the literature, we can find a similarity to the present device and theories related to the relaxation of quasiparticles in detectors making use of quasiparticle traps. In one example, a quasiclassical model by Golubov and Houwman [194] for a superconducting bilayer of materials S and S' was found to exhibit an effective inelastic relaxation rate τ_{Eff} due to the parallel contributions of both layers

$$\frac{1}{\tau_{Eff}} = \frac{1.82}{d_S} \left[\frac{L_{eff}}{\tau_{ES}} + \frac{L'_{eff}}{\tau_{ES'}} \right] \frac{A'}{A}, \quad (5.7)$$

Here, d_S is the thickness of a bulk superconductor which has been overlaid with a superconductor with a lower gap, and L_{eff}/L'_{eff} (A/A') are effective thicknesses (areas) of the layers extracted from their model. Because these contributions come entirely in parallel, we posit that it is reasonable to expect inelastic quasiparticle relaxation in a bilayer to be dominated by the fastest rate between the two layers, which can vary greatly if one of the layers is disordered. In the case of our experiment, the Cu film produced in our deposition is so thin that it may be percolation limited or else extremely disordered. This could reasonably be expected to enhance the inelastic relaxation so far over that of Al that only a very small volume as we have used is necessary to damp out the quasiparticle

transport [193].

5.1.2 Voltage Asymmetry of the Quasiparticle Chemical Potential

In addition to these non-local conductance measurements, a series of voltage measurements of the chemical potential via ac-coupled voltage pre-amplifiers were performed. The frequency of this lock-in experiment was 11.777 Hz, and the experiment performed at 20.3 mK using an identical grounding layout as the conductance measurements. These dV_B/dV_A measurements were expected to provide an independent measurement of μ_{Q^*} for comparison to the non-local conductance for the purpose of better modeling the charge imbalance length in these NIS junction arrays. To our surprise, this method showed asymmetries which cannot be associated with the charge imbalance

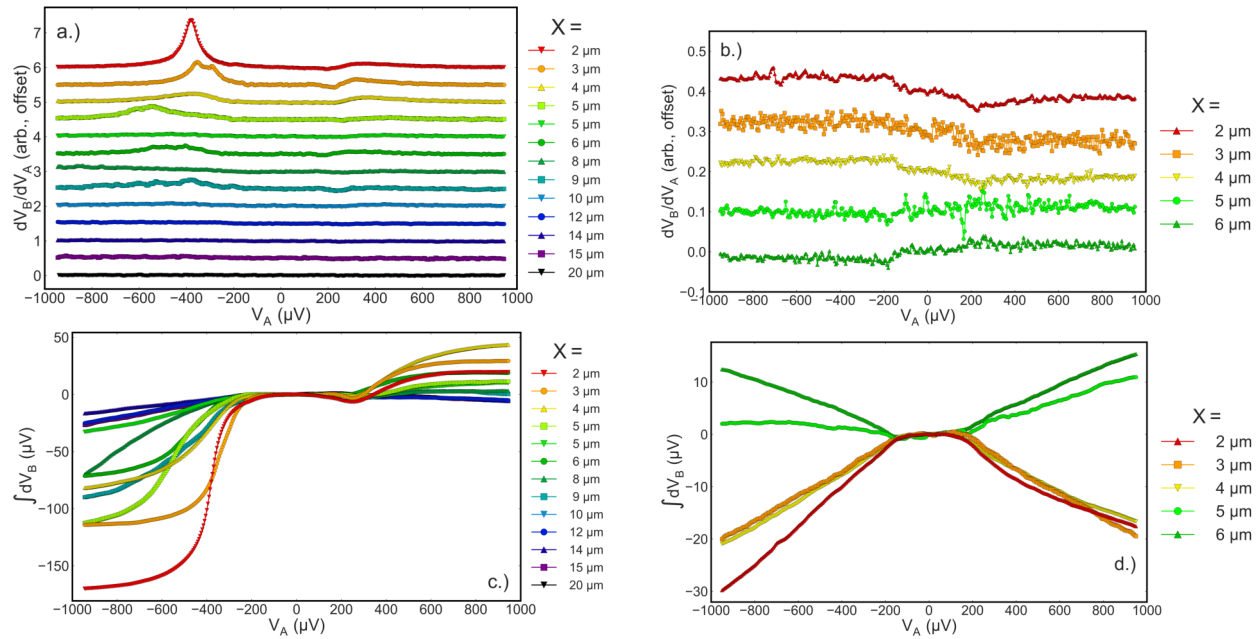


Figure 5.6: a.+b.) Nonlocal differential-voltage measurements of the control (a) and bilayer (b) devices, offset for clarity. c.+d.) Integral of the same data, demonstrating the large asymmetric change in the junction voltage of the control (c) device, and the unexpected symmetric voltage change of the bilayer (d) device.

itself, with particle-hole symmetry being clearly violated over length-scales on the order of λ_{Q^*} as seen in Fig. 5.6.

In a non-local conductance measurement, the zero bias current is nominally driven by the local quasiparticle chemical potential. In a voltage measurement, no current flows and the NIS junction should equilibrate to μ_{Q^*} , such that dV_B/dV_A should show peaks corresponding to the non-local conductance maxima when measured using the same set of junctions. However in the control device we clearly see a larger peak at negative bias. This was checked for every combination of pairs using non-local grounding on both sides of the device (i.e. mirroring the experiment) to preclude symmetry breaking due to the voltage reference leads, but in almost all cases the negative voltage peak was larger. Initially we considered that this might be due to the injected quasiparticles resolving into a supercurrent which has a well defined current path away from the injector, breaking inversion symmetry. However, attempts to additionally supercurrent bias the measurement in this arrangement did not change the peak magnitude considerably, up to the critical current of the wire (greatly in excess of the bias currents generated across the NIS junction). We can integrate the differential signal with respect to the injector voltage to extract the corresponding total change in the dc-voltage, $\int dV_B$ (this dc-value cannot be easily measured directly as explained in §3.2.2.1). Clearly, in the control device, there is a much larger negative bias saturation of the chemical potential at the detector, which decays with X , but in a highly non-systematic manner which we have not been able to correlate with properties of the injector/detector junctions themselves via any simple normalization. For a specific detector junction, the behavior is somewhat systematic, but it appears that the effect is simply different depending on what lead in the device is used.

In the control device, we can also observe a sub-gap reversal of the voltage, and a saturation at high bias. Some saturation of $\int dV_B$ is expected as the charge of individual quasiparticles will

also saturate at high energies. However as the total current increases linearly with V_A , the non-equilibrium contribution must be somehow balanced by increased relaxation, in agreement with our measured energy dependence for τ_E^{-1} . The negative differential voltage seen below $+1\Delta$ is also intriguing, as no corresponding non-local conductance effect was observed.

In the bilayer device, no symmetric peaks are seen in the differential voltage that can be associated with a shift in the chemical potential. Integration shows that $\int dV_B$ is much smaller than in the control device, and is generally symmetric and even changes sign. This is both a strong indication that the charge imbalance length in the bilayer is considerably smaller than in the control, and that the voltage determined in this manner is likely not consistent with a single well defined chemical potential determined by the charge imbalance alone.

These measurements presented additional concerns related to the stability of the apparatus, as measurements tended to retrace poorly (compared to the non-local conductance) and drifted slowly over time. At the time of writing, we remain unsure of the exact mechanism underpinning this effect. One possibility is that the actual non-equilibrium distribution is so far from a thermal one, that the chemical potential for quasiparticles is not well defined and thus equilibration of the Fermi-energy in the normal metal detector to that of the quasiparticles does not occur as expected. This is a well known effect in diffusive metals where non-Fermi distributions can be generated by certain boundary conditions for the Boltzmann equation, as has been experimentally observed in tunnel probes into normal metals [195]. In this way, non-local conductance measurements seem to be preferable, as they sample the entire transverse quasiparticle distribution and thus do not depend sensitively on the exact shape of the non-equilibrium distribution. This is alluded to in several similar studies, particularly Ref. [184] by Hübner et al., where it is briefly claimed that “at low temperature the chemical-potential model breaks down” and that the strong, non-linear

temperature dependence of the NIS junctions distorts such measurements, however it is unclear how this relates to the observed asymmetries.

5.2 Dual Bias Experiments in Junction Array Devices

In conjunction with the individually biased conductance measurements reported in §5.1.1, measurements were performed on both the control and bilayer devices under dual bias conditions similar to those reported by Kolenda et al. in Ref. [185], to instead measure $G_{BA}(V_A, V_B)$, for $X = 2 \mu\text{m}$. During dual-bias, one injects quasiparticles of either species simultaneously through two junctions, and the resulting non-local conductance can become quite complex to consider. For instance, the overall charge current at the detector will reverse directions depending on the sign and magnitude of both V_A and V_B , as both junctions act reciprocally as detectors and injectors of quasiparticles. For this purpose, we will retain the same sign convention as before such that charge imbalance generated by V_A always gives a positive non-local conductance. We present our results, also found in the supplementary material to Ref. [151] for these conditions in Fig. 5.7. Before considering the individual results here, one must note that the local conductance of both the injector and detector changes due to the mutual effect of their injected quasiparticles on Δ . As such we also simultaneously measured the local conductance of both junctions.

First, we can consider the non-local conductance of the bilayer device, which shows an overall anti-symmetric structure above the gap which is considerably larger than that seen for charge imbalance alone. Both the sign of the non-local conductance and the magnitude appear to be consistent with the purely thermal component of the model of Kolenda et al., whereupon the non-local conductance is caused by a softening of the gap due to Joule heating in the leads of the device during injection [185]. This causes an increase or decrease in the current I_B due to the electronic temperature of the junction $T_{e,B}$ becoming a function of V_A . This can be caused entirely by phonons and

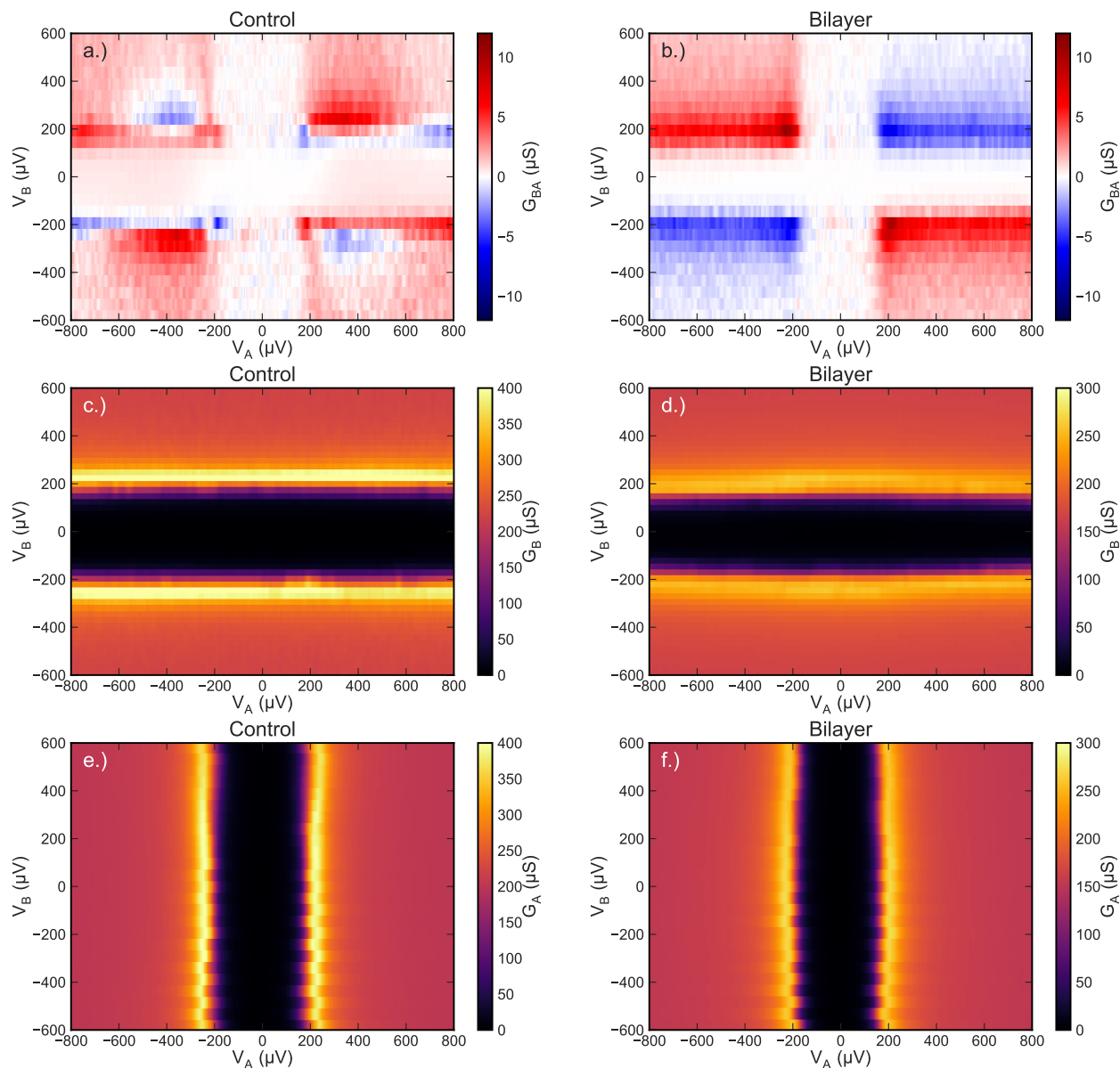


Figure 5.7: Dual-bias conductance measurements for $X = 2\mu\text{m}$ for both devices, measured simultaneously at 20.7 mK. No normalization is applied. Fig. a.) & b.) correspond to the non-local conductance as defined in the main text. c.) & d.) correspond to the local-conductance at the detector junction B. e.) & f.) correspond to the local-conductance at the injector junction A. Some jitter in the local conductance G_A is present, but is an artifact generated by averaging during the voltage sweep. Figure reproduced from the supplementary material of Ref. [151].

was argued to be the a dominant factor when the quasiparticle transport is weak and the junctions closely spaced. One caveat of this is that when $|eV_A| \approx \Delta$ the current is still fairly small and the heating effect should be minimal. However, the non-local conductance is in fact sharply peaked. In the local conductance of the bilayer device, we do not see any strong effects due to the previously discussed broadening.

In the control device, we see very little anti-symmetric conductance of the same type, and the general background is positive and symmetric with respect to both V_A and V_B , consistent with a strong charge imbalance contribution. There also emerges anti-symmetric “lobes” at $V_A \approx 400 \mu\text{V}$ with the opposite sign seen in the bilayer, indicating a different transport effect due to the simultaneous injection of quasiparticles and quasi holes which is not captured in current models of dual bias in NIS junctions. There is also a tilting of the subgap bias when $|eV_B| \leq \Delta$ which can be seen as an antisymmetric contribution to the non-local conductance, presumably due to energy-mode imbalance. In the control, G_A also varies somewhat more strongly with respect to V_B than in the bilayer, with a softening of the coherence peak maxima for $|eV_B| \geq \Delta$. This again motivates the thermal model of Kolenda et al., however in the control case the quasiparticle effects are clearly observable, while in the bilayer they are not. This serves as further qualitative support for the large increase in inelastic relaxation due to proximity with the disordered Cu layer, and expands these results beyond pure charge imbalance to consider the possibility that the energy mode is also suppressed in this experiment, which is of more direct concern for quantum devices as the sources of excess quasiparticles in those systems are generally charge neutral.

5.2.1 Dual Bias Differential Voltage Measurements

To further the analysis of §5.1.2, a similar dual bias scheme was employed to better understand the asymmetry seen in the differential voltage measurements. The measurement layout is essentially a

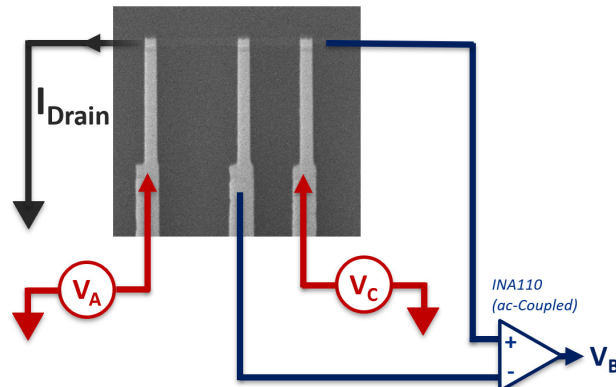


Figure 5.8: Short form schematic indicating the layout of the voltage biases and measurement leads for three junction differential measurement. The separation from the A to B junction is $3\ \mu\text{m}$, and the separation between B and C is $2\ \mu\text{m}$. A gain of $\times 500$ was used on the INA110 preamplifier, followed by an SR124 lock-in amplifier. The bias voltages were produced in the same manner as in dual-biased conductance measurements and uses the circuit described in §3.6.

combination of the non-local dual bias and non-local voltage measurements, as shown in Fig. 5.8, where two junctions are voltage biased at V_A and V_C while a third junction between them is used to monitor the differential voltage due to an ac-excitation applied to V_A to obtain $dV_B/dV_A(V_A, V_C)$. In this scheme, V_C acts to offset the chemical potential induced by V_A , which also effects the non-local conductance $G_{CA} = dI_C/dV_A$ similarly to Fig. 5.7.a.

The location of the peak in the differential voltage is seen to clearly shift due to the application of the (local) V_C bias, and jumps from negative to positive V_A when $V_C \approx -500\ \mu\text{V}$. The shape of the peak also evolves, broadening considerably for $|eV_C| \geq \Delta$, which may be an indication of increased effective temperature due to energy-mode imbalance generated by V_C . At the same time, the region of negative differential voltage also reverses, but always seems to occur near the V_A gap edge opposite the peak (a slightly positive kink is associated with the opposite gap edge but blends into the peak structure itself). No clear corresponding features are seen in the differential conductance *between* the outer injector junctions shown in Fig. 5.9.d, which clearly demonstrates

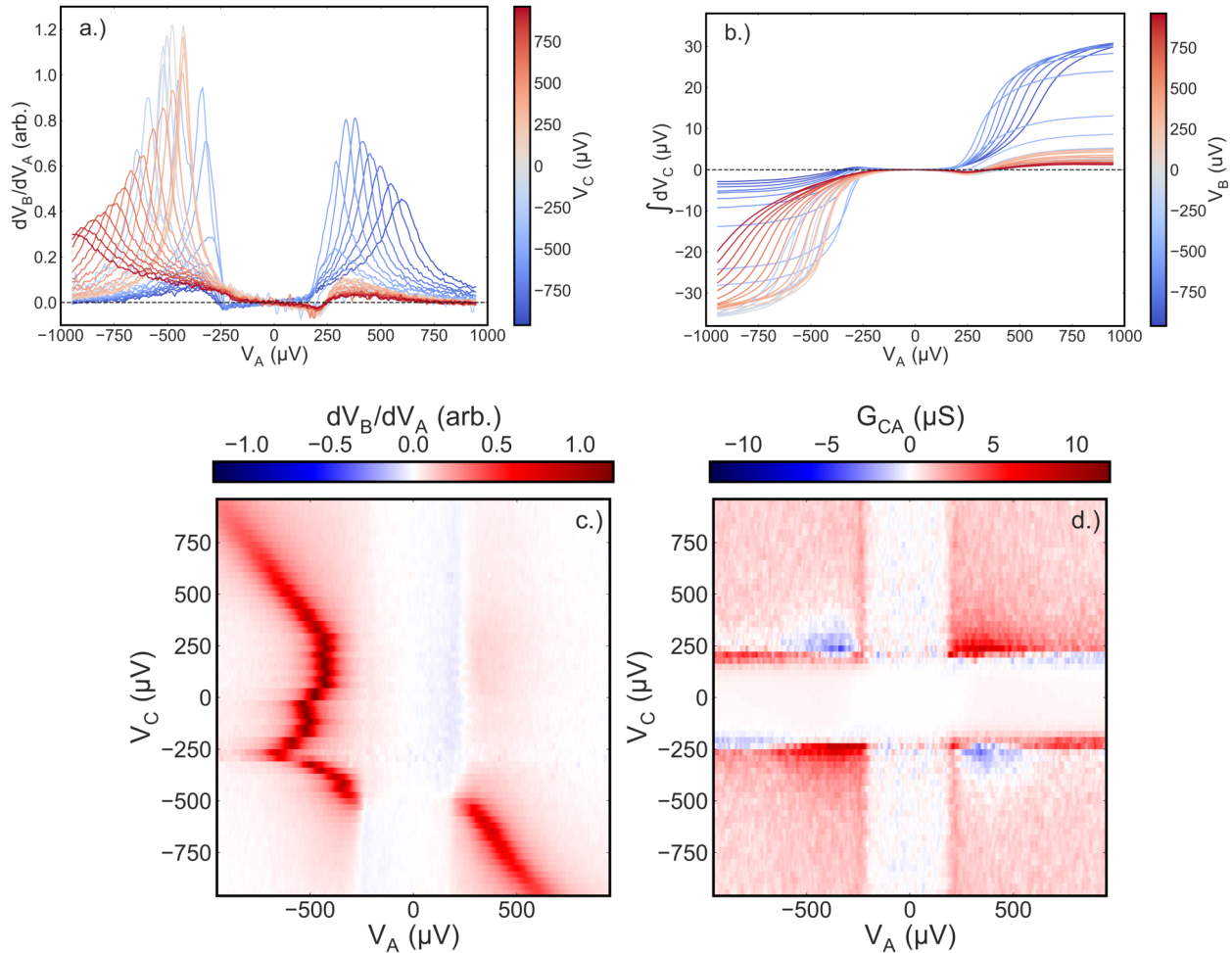


Figure 5.9: Three junction differential voltage/conductance measurement on the control device described in §5.1.1. a.) Raw differential voltage data taken as a function of bias on the outer two tunnel junctions. The horizontal dashed line at 0 is a guide for the eye, indicating the crossing over between positive and negative differential voltage. b.) Integral of a. demonstrating the magnitude of the chemical potential measured in this arrangement. c.) Re-plotting of the data in a. as a heatmap, indicating the magnitude of the differential voltage data. d.) Simultaneously measured non-local conductance data between junctions A and C .

the a-symmetric features shown before for $X = 2\ \mu\text{m}$. As such, it seems likely that this peak effect in the differential voltage stems from a source which does not drive a corresponding tunneling *current* when quasiparticles are drained at the detector at zero bias.

5.2.2 Replication Studies and Issues with Differential Voltage Detection

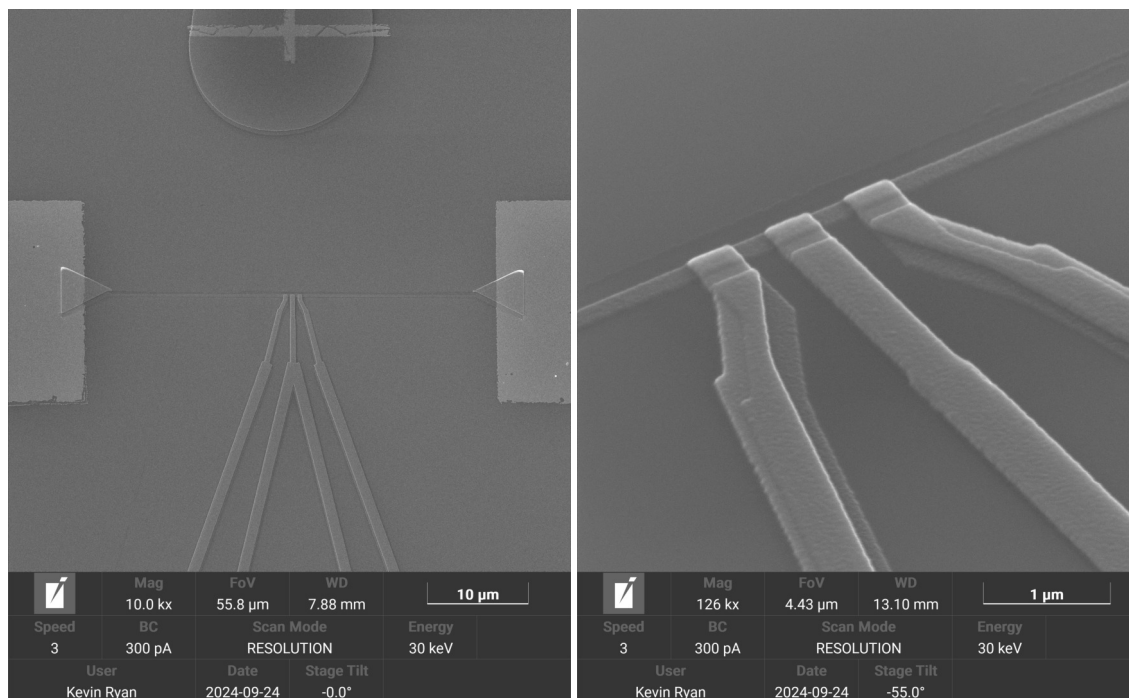


Figure 5.10: SEM micrographs of the short junction, three terminal device used for comparison to the results presented in §5.1.1.

At the time of writing, we do not fully understand these discrepancies, but more recent results have provided some hints about circumstances for this effect. An attempt to replicate this experiment was performed using devices with three, 400 nm wide NIS junctions on a 20 nm thick Al wire with a nominal width of 200 nm. This matches closely the design of the prior devices where $\lambda_{Q^*} \approx 4 \mu\text{m}$, however in this case the separation between junctions was reduced to 700 nm (measured between the center of each contact) such that the quasiparticles should not relax in charge nor energy before reaching the detector. Also, the Al wire was constructed such that, rather than extending out to wirebonding pads at the edges of the sample, the central wire terminated onto Au NS contacts on either side. This yields a higher lead resistance, but was hoped to provide better thermalized, normal state reservoirs. SEM micrographs of this style of device are shown in Fig.

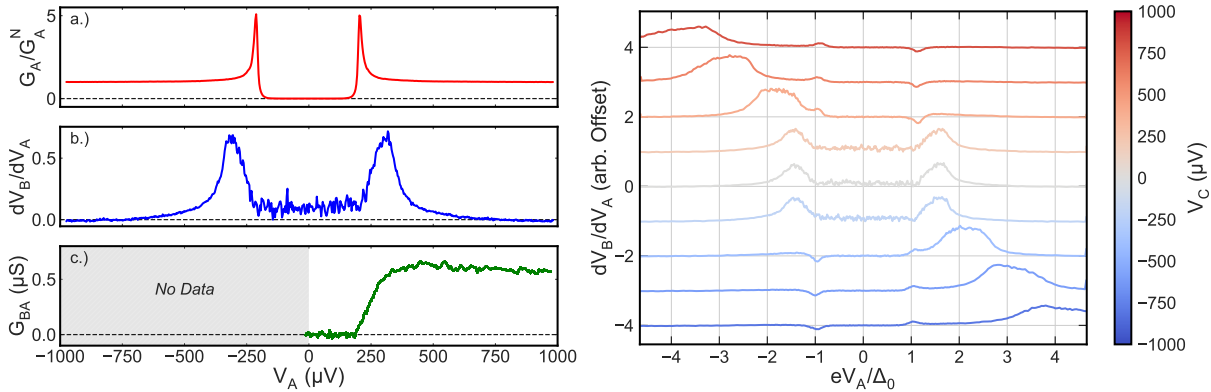


Figure 5.11: Characteristic data obtained from the three terminal device used in the replication study. a.) The normalized local conductance of the injector junction during measurement. b.) The differential non-local voltage of the central detector junction, measured simultaneously to the local conductance. c.) A separate measurement of the non-local conductance taken for $V_A \geq 0$. d.) Non-local differential voltage measured with an applied local bias V_C .

5.10. In reducing the total number of voltage probes down to just those required for this experiment (8 vs. 16 leads per device in the earlier measurement), the overall electronic temperature of the devices was found to be considerably lower, and could be fit to $T_e = 34$ mK with $\Delta_0 = 204$ μ eV (and with no Dynes parameter).

Measurements were performed at 25 mK using the same circuit from the prior discussion, and both non-local conductance and differential voltage measurements were performed. Examples of these results are shown in Fig. 5.11. In the two terminal version of the experiment, where V_C is allowed to float, we see in Fig. 5.11.b that the non-local differential voltage is symmetric with respect to V_A and generally positive. For $|eV_A| \leq \Delta$, the dV_B/dV_A is positive but uncharacteristically noisy, implying large fluctuations of the chemical potential take place when only a small current of quasiparticles are being injected. In this case, we see clearly that the differential voltage peaks reduce quickly to zero, which implies that the chemical potential saturates within a range of approximately Δ beyond the superconducting gap. This is paradoxical, as it this would imply that

resulting quasiparticle current would be constant, at which point the non-local conductance due to charge imbalance should go to *zero*. Instead, one sees only the ordinary non-local conductance measurement as is shown in Fig. 5.11.c, which is in good agreement with other works on the subject referenced earlier. The application of a third, local bias voltage V_C shifts the location of the differential voltage peak just as was seen in the prior device, and is shown in Fig. 5.11.d. This also reveals the previously missing antisymmetric peaks at the gap edge once the chemical potential has been shifted sufficiently far from equilibrium, and the sign of the peaks again reverses depending on the sign of V_C .

Clearly, the differential voltage observed in this method is a convolution of more than one factor, and is seemingly *not* well associated with the chemical potential that leads to a finite non-local conductance via charge imbalance. The difference of the equilibrium position of the dominant differential voltage peak between devices is also perplexing, and leads to the conclusion that this effect is either somehow related to the symmetry of the placement of the voltage leads, or alternatively, was compromised in the former experiment, possibly due to the very large number of electrical leads required. This could either be an issue of the effective temperature, or a physical defect somewhere in the wiring of the experiment (although arguably this can be ruled out also as no issues were seen in the conductance experiments, and the isolation of the measurement leads of the devices was repeatedly checked). One might also consider the possibility that thermoelectric effects might be at play due to temperature gradients induced in the device during biasing which produces energy mode non-equilibrium, however as only a small supercurrent is present and nominally no magnetic field was applied to these devices, this should be more or less ruled out by time-reversal (particle-hole) symmetry, which is fundamental to our models of quasiparticle excitation.

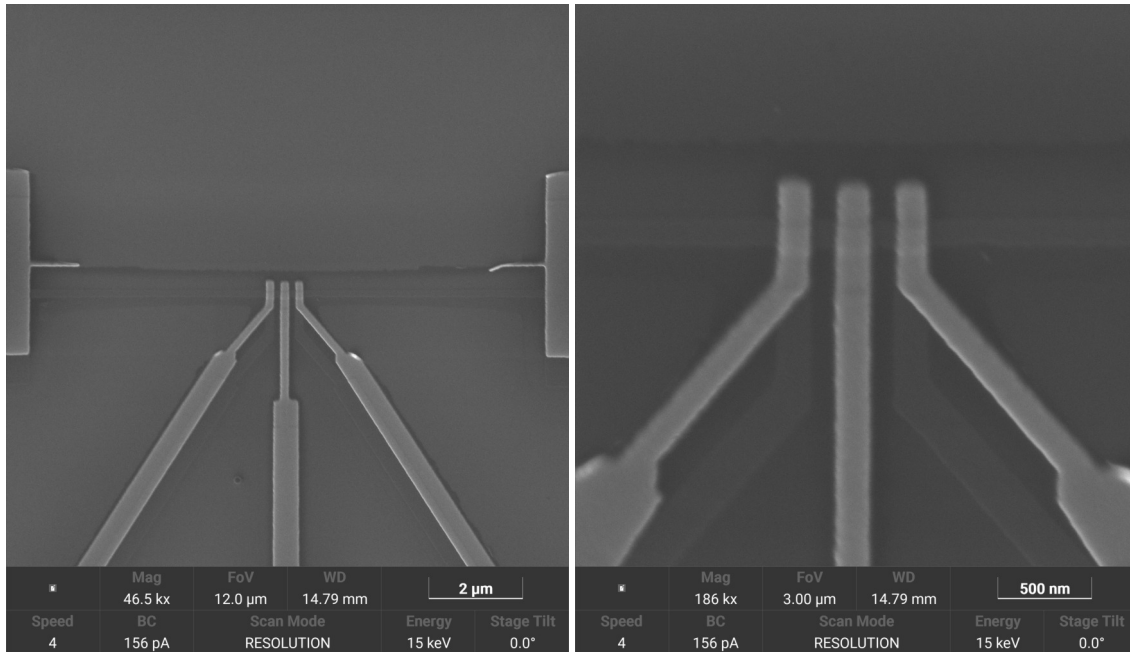


Figure 5.12: SEM micrographs of the mesoscopic three terminal devices.

5.3 Results on a Mesoscopic Thin Film Device

As a final experimental survey, further three terminal devices were prepared close to the design the limits our current techniques, using as thin and narrow a superconducting wire as possible to which thick (but narrow) Cu electrodes were deposited to form NIS junctions, as shown in Fig. 5.12. This was chosen to both place the junctions within a few superconducting coherence lengths of one another, and to minimize the orbital depairing which is known to occur in thicker superconducting films when subjected to a large in-plane magnetic field [196]. This has, in other experiments, allowed for a spin-selective tunneling of quasiparticles by lifting their spin-degeneracy via the Zeeman effect, leading to a separation of the spin-up and spin-down density of states [197]. The fabrication of these devices was performed in generally the same way as in Ref. [151], except that when narrowing the feature size of the Al wire, issues with the PMGI/PMMA interface required

R	l	w	d_{Al}	l_{mfp}	D_N	L_T^{20mK}	X	A_N	d_{Cu}
1.45 k Ω	11 μm	150 nm	8 nm †,*	2.49 nm †	16.9 cm 2 s $^{-1\dagger}$	803 nm †	300 nm	0.026 μm^2	80 μm^{2**}

Table 5.3: Normal state transport properties and physical dimensions of the junctions used in the mesoscopic device. The separation X is again measured between the midpoints of the junctions, and is reported for the nearest neighbor pairs which have a nominal contact area A_N . Other symbols are defined in the text. † Values are estimated using an upper bound for d_{Al} , as the thickness of the un-oxidized Al layer cannot be measured directly. The resulting estimates are thus lower bounds. $*$ Al deposited at $+10^\circ$, crystal monitor value reported. $**$ Cu deposited at -35° , crystal monitor value reported.

that the total length of the wire be shortened to yield a continuous wire. Like before, the number of total leads was minimized to just 7 to reduce noise coupling into the device, however no normal metal reservoirs were used, such that the central wire again extends (under a thick layer of Cu) all the way to the wire-bonds. In this section, we describe three sets of experiments taken on one such device which demonstrated particularly good local conductance spectra. For the purpose of consistency, we will refer to the three junctions on these devices as A, B, C , however most experiments discussed in the following sections will pertain only to A, B .

5.3.1 Basic Characterization and Non-local Conductance

The geometry and basic transport parameters of this device are summarized in Tab. 5.3. Bulk resistivity of the Al was measured at 25 mK by biasing the device above its critical current of $I_c \approx 20 \mu\text{A}$ and measuring the four terminal resistance of the central wire. Despite the higher overall resistance of the sample, we can find that the Thouless length of the Al wire is still considerably longer than the separation between junctions. As we cannot directly determine the thickness of the metallic Al after oxidation, it is difficult to establish exact values for the resistivity and derived constants. As such, we have assumed the largest possible value for the film thickness corresponding to the deposited film thickness before oxidation, such that these values are only lower bounds.

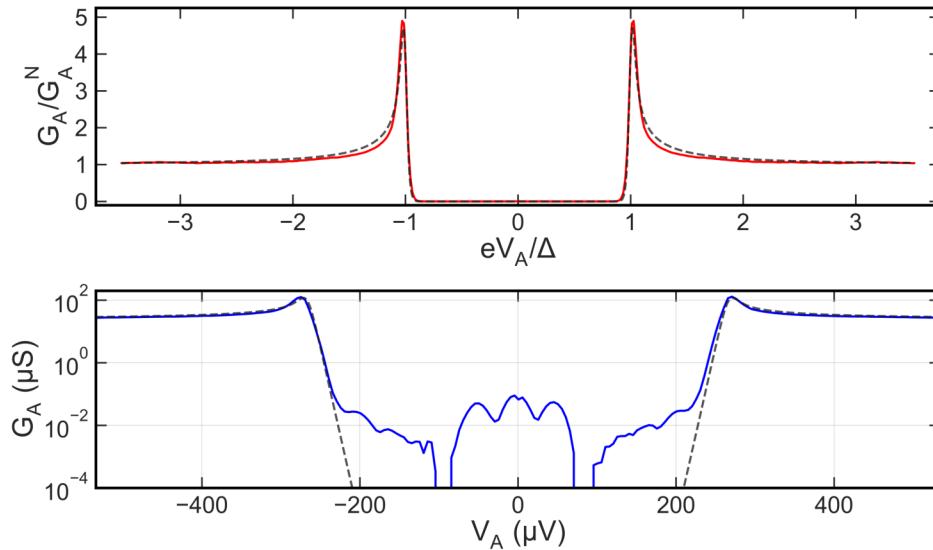


Figure 5.13: Top Panel: Full, normalized conductance spectra (red), fitted to $\Delta = 267 \mu\text{eV}$ and $T_e = 45 \text{ mK}$ with no Dynes parameter (black). Bottom Panel: The same, raw data (blue) on a log scale for biases near or below the gap energy, demonstrating the small anomalous conductance features near zero bias.

Each of the junctions themselves are between 20 to 25 μS in the normal state, such that the resistance area product is approximately the same as in the prior, larger area devices. The resulting current scales however are much lower, motivating our switch to AD4530 based TIAs which have a negligible input bias current and a higher gain of $1 \times 10^8 \text{ V A}^{-1}$. Individual conductance spectra for the junctions are sharp and can be fit to $\Delta \approx 265 \mu\text{eV}$ with no Dynes parameter and $T_e \approx 45 \text{ mK}$ as before, indicating an improved electronic noise. An example of this fit is shown in Fig. 5.13.

Curiously, with this improved sensitivity we were able to discern small conductance anomalies in the subgap region, which had not previously been seen in any other NIS junctions tested. These appear to be slightly different for each device, but are symmetric with respect to V_A and can occur with or without a peak at $V_A = 0$. In some contexts this would be an indication of magnetic defects within a superconductor which can lead to the formation of Shiba states [198] in the vicinity of the devices. In this case however, it is known that Al typically does not host magnetic moments due to

even strongly magnetic impurity species [199]. Moreover, in certain junctions we observe a periodicity of these peaks which cannot be readily explained by Shiba states, leaving their origin highly uncertain. Fortunately for our consideration of non-equilibrium states, the conductances of these features are quite small and thus we do not expect this to impact the quasiparticle transport.

5.3.1.1 Evidence for Energy Mode Non-equilibrium

We next consider dual-bias conductance measurements across the A, B pair of junctions for a wide range of biases. In the local conductance of the junction A , there is a clear “snapping” of the coherence peak position inwards when V_B reaches either gap edge as shown in the left panel of Fig. 5.14. The effect is considerably sharper than what was seen in other devices, and indicates a strong modification of the gap when quasiparticles with $E_k \approx \Delta$ are introduced (i.e. pure energy imbalance). The corresponding non-local conductance is also much more sharply defined than in prior experiments, with the antisymmetric lobes seen above the gap in Fig. 5.11.d being now resolved to occur sharply between $|eV_A| = \Delta$ and $|eV_A| \approx 3\Delta$. Similarly, one now sees a pronounced set of anti-symmetric peaks which extend to much higher energy in V_B when both

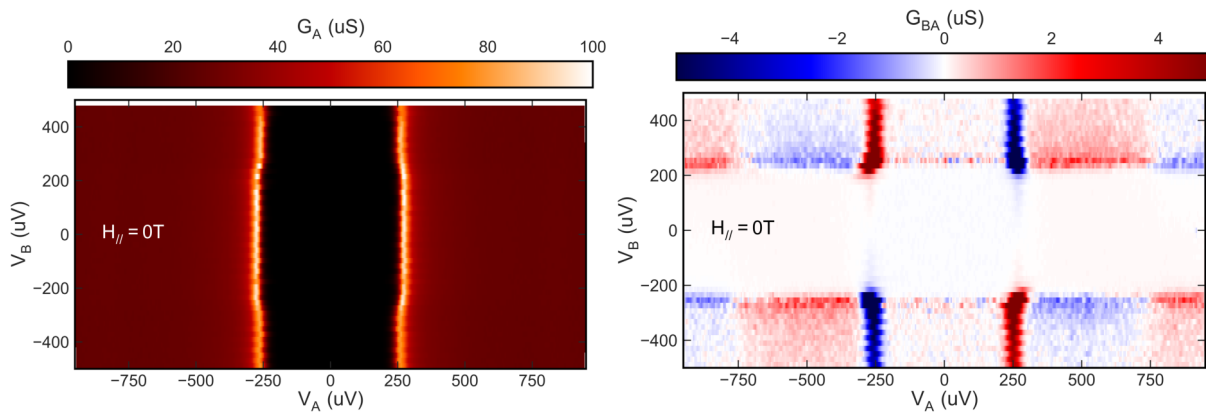


Figure 5.14: Local and non-local conductance data, measured simultaneously at 25 mK on the A, B junction pair of the mesoscopic device.

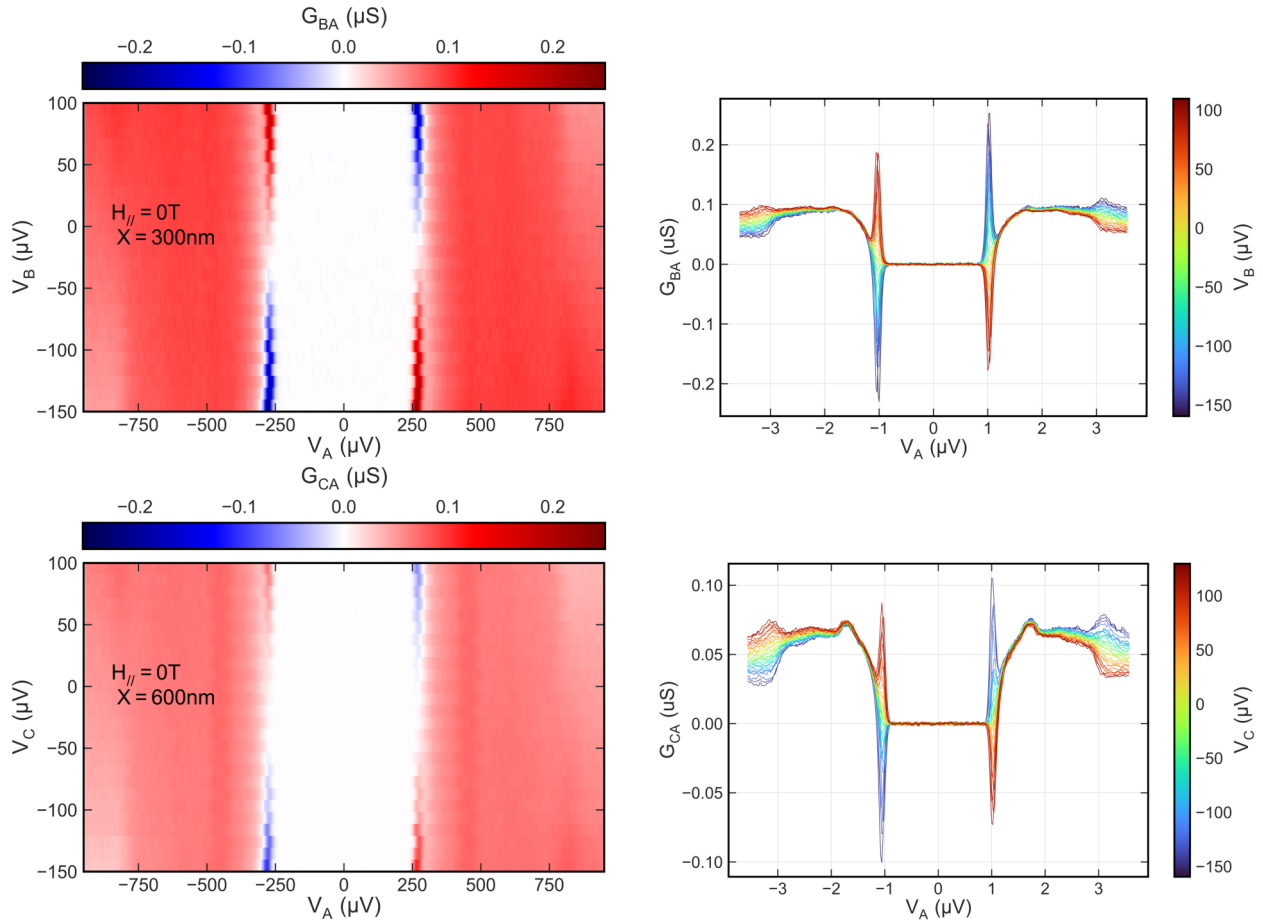


Figure 5.15: Non-local conductance measurements of the A, B and A, C junction pairs on the mesoscopic device. The left and right panel's data are the same, but are colored to highlight the asymmetric patterns. The heatmaps are scaled to the same absolute conductance values, but are not normalized to account for differences in the individual junction conductances.

junctions are biased near the gap edge.

Interestingly, these anti-symmetric peaks in G_{BA} extend for the case where V_B is biased *below* the gap, where in the former devices only a skewed but predominantly smooth and symmetric conductance due to charge imbalance was seen. Making a more sensitive measurement of the devices in this regime, we can clearly discern these sharp, antisymmetric ridges exactly for $|eV_A| = \Delta$, as shown in Fig. 5.15 as both heat-maps and individual traces, when detected using either the

B or C junctions. The overall magnitude of the signal is clearly reduced for the wider spaced A, C pair, with the relative magnitudes of the symmetric (charge imbalance-like) and anti-symmetric (energy-imbalance-like) components changing slightly when compared to the A, B pair. In G_{CA} in particular, this amplifies these features over what was discernible in the prior measurements, and there are large anti-symmetric components above $|eV_A| \geq 3\Delta$, as well as symmetric peaks near $|eV_A| \approx 400 \mu\text{eV}$. No clear effects are seen at 2Δ precisely (nor is this seen in the local conductance), which we take as an indication that no additional pair tunneling occurs.

While the exact shape of these curves may be interpreted in terms of phonon-spectra contributions to the local tunneling (not taken into account for the local conductance of our fits), the strong anti-symmetric behavior for sub-gap detector bias appears only in devices at this extremely short length-scale. In similar work by Kolenda et al. [185], those authors employed closely spaced NIS junctions with long, thin Cu leads. The resulting conductance spectra contained a similar antisymmetric peak structure near the gap edge, which was attributed to a non-local antisymmetric components near $|eV_A| \approx \Delta$ in the context of gap suppression due to phonons generated by Joule heating of the leads. However, this heating model does not predict such sharply peaked features nor the reappearance of an anti-symmetric component at higher bias. Moreover, the design of our devices should have a considerably lower Joule heating in the leads, as Kolenda et al. specifically constructed their devices to have large injector heating by using very thin Cu layers and $\approx 100\times$ larger normal state conductances for devices with a similar junction spacing. Finally, Kolenda et al. do not report any reversal of the sign of the anti-symmetric component as we have repeatedly seen. These features lead to the conclusion that, rather than a trivial heating effect, we see anti-symmetric features due to a spontaneous gap suppression via the injection of charge-neutral quasiparticles. The sign reversal of the effect with respect to V_B is associated with the sign of electron current flowing into/out of the normal lead as the chemical potential is varied. When the Fermi energy of

the detector is exactly matched to that of the condensate, no current flows except due to charge imbalance. However as this is tipped one way or the other, a net current may be established when drawing from the excess population of charge neutral quasiparticles, by a change in the probability factors for tunneling discussed earlier in Tab. 2.1. The sign reversal of the peaks with V_A is simply associated with the definition of dV_B/dV_A .

In this context the appearance of the additional anti-symmetric behavior, which mostly clearly appears at 3Δ , would indicate that further energy imbalance is being generated in addition to charge imbalance at these biases. One possible explanation could be an effect sometimes referred to as quasiparticle multiplication, where a single quasiparticle with $E_k = 3\Delta$ can emit a phonon with $\hbar\omega \approx 2\Delta$ to lower its energy to $E_k = \Delta$ [200]. That phonon in turn breaks a pair and thus yields two additional $E_k = \pm\Delta$ quasiparticles, leading to the injection of three charge neutral quasiparticles rather than a single charged one. Because of the finite excitation energy of quasiparticles, this has a sharp energy onset around 3Δ which has (to our knowledge) only been studied previously in Josephson junction based devices [201].

5.3.2 Effect of a Large in Plane Magnetic Field

Attempts to perform the same experiments under a large Zeeman splitting field were unfortunately not successful. In a simple treatment, the expectation is that the quasiparticle density of states for spin-up and spin-down branches are split by a Zeeman energy $2\mu_B H$, which is the same as that of the constituent electrons [196, 74]. The exact field values and film thicknesses required to see this effect however are somewhat varied, with some experiments showing strong spin splitting in Al at modest in plane fields [197, 189, 188] and other reporting it only at very high fields [74] or via exchange coupling with ferromagnetic bilayers [149], just to name a handful of cases. In our current work, we have not yet achieved a clear splitting of the quasiparticle density of states at fields up to

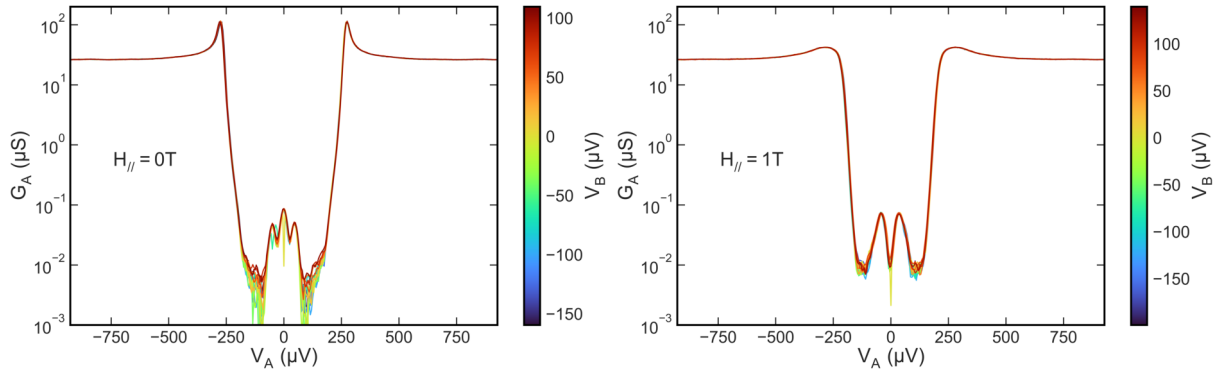


Figure 5.16: Local conductance spectra of the A, B junction pair, focusing on the subgap features with and without an applied 1T in plane field.

1 T, and appear to be dominated by a large broadening associated with either pair-breaking due to stray fields in the environment of our dilution refrigerator, or by spin-orbit scattering which yields broadening due to intermixing of the quasiparticle spin orientations [196]. This was also seen in attempts to apply a large field to the three terminal device shown in Fig. 5.10. In both attempts, the magnetic field was oriented along the direction of the wire, and the negative results confirmed by carefully compensating for any perpendicular component using the split-coil of our magnet (to no avail). The lack of peak splitting can be seen in the local conductance of our mesoscopic device under a 1 T applied field (which was expected to split the peaks by $110 \mu\text{eV}$). In those measurements, only the sub-gap features are modified by the application of a large in plane field as shown in Fig. 5.16. No second peak or shoulder are found in the coherence maxima, despite the very small degree of thermal broadening in this experiment.

The effect of such a large in plane field on the non-local conductance is considerable, but largely amounts to an overall broadening and strong suppression in magnitude of the non-local conductance. This is shown in Fig. 5.17 for the A, B pair (which we will focus on for the rest of this discussion). In this case, we find that the pronounced peaks at $|eV_A| = \Delta$ now show as lobes which taper off more quickly, while the antisymmetric regions for $V_A \geq \Delta$ to $V_A \leq 3\Delta$ are

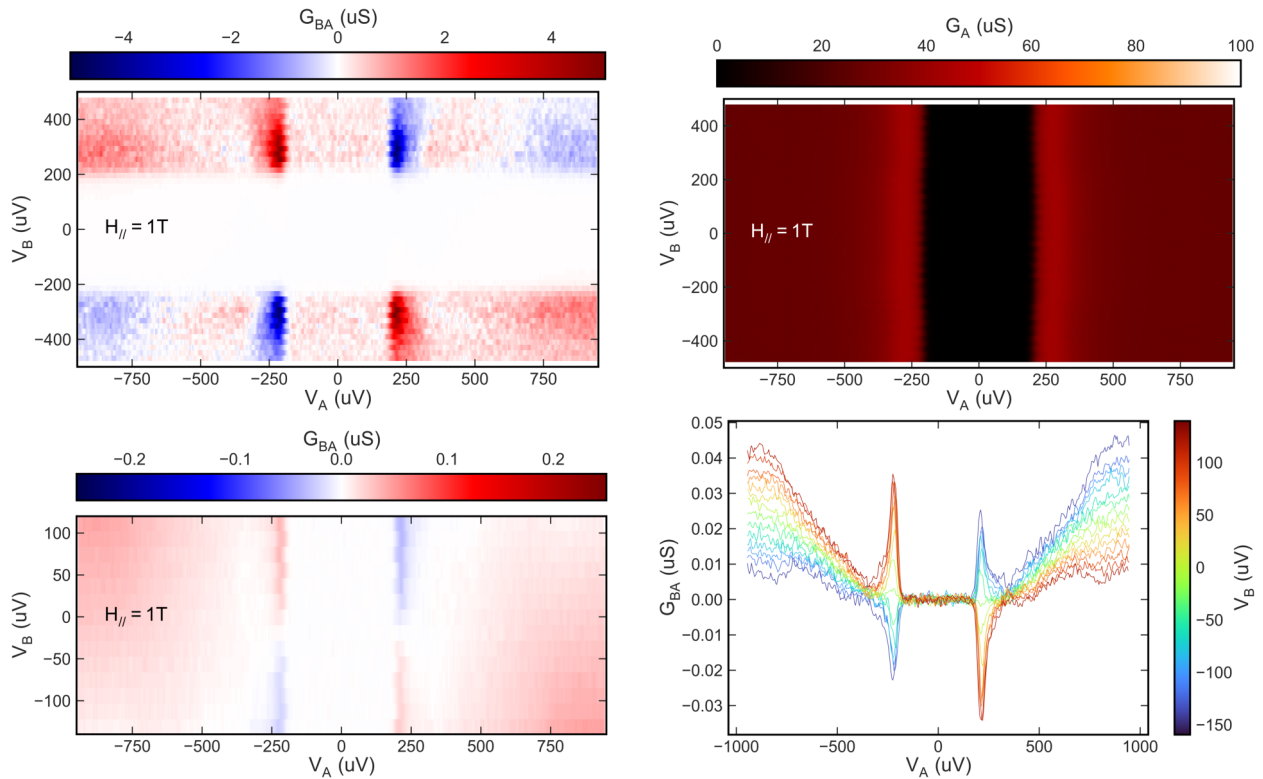


Figure 5.17: Top Left: Non-local conductance G_{BA} of the mesoscopic high field device in a 1T magnetic field, biased over the same range as Fig. 5.14. Top Right: Local conductance G_A , demonstrating a highly broadened transition without discernible peak splitting. Bottom Left: Subgap V_B bias, remeasured at higher gain. Bottom Right: Same data as bottom left, presented as individual traces for clarity.

softened, and almost appear to be slightly canted away from the V_B gap edge (this is seen most readily in the upper right and lower left quadrants of the G_{BA} heatmap for $|eV_B| \approx 300 \mu\text{eV}$). For $|eV_B| \leq \Delta$, peaks are still seen at the V_A gap edges, and a broadly asymmetric behavior is seen at higher energies, still containing a component that is largely anti-symmetric in V_B (although without strong kinks).

Much of the observed behavior at $H_{\parallel} = 1 \text{ T}$ can likely be attributed to the presence of trapped flux lines within the superconductor, which are known to serve as a loci for quasiparticle trapping [202]

due to the isolated normal core of an Abrikosov vortex. This would significantly reduce the quasiparticles responsible for non-local conductance in this experiment, but is of interest as this effect has been considered as a means to induce strong quasiparticle trapping in superconducting quantum devices [203, 204]. Anecdotally, we expect there to be several mT of stray perpendicular field in these results, but it would require a lengthy and studious effort to perform a detailed experiment on the flux dependence of the full non-local conductance by the present method. As such, these findings are mostly inconclusive, due to the strongly reduced non-local conductance and the lack of discernible transport of the two spin-split quasiparticle species.

5.3.3 Imbalance Mode Mixing via Supercurrent Injection

To conclude, we will describe the effects seen when applying a large super-current (on the scale of the critical current) across the wire while varying V_A and holding V_B at a small fixed bias. This was done by use of a floating voltage source and a pair of matched $10\text{ M}\Omega$ resistors placed on opposite sides of the central wire of the device. These currents flow with respect to the ground, taken to be on the left side of the device (closest to junction A) and thus do not cause a large offset bias across the junctions. In this arrangement, we are able to drive the wire completely normal, although the process is highly stochastic, and a switch into the normal state can sometimes be triggered at fairly low current biases due to (seemingly) mechanical vibrations in the laboratory etc. The small bias on V_B is on the order of $-20\text{ }\mu\text{eV}$, and is due to the input voltage offset of the amplifier.

First we can consider the local conductance of the injector and the relationship between quasiparticle injection and the critical current. No magnetic field is applied to the device, and we first measure by sweeping the supercurrent I_S at fixed V_A all the way above I_c . We plot only the data in the superconducting state, however there are some artifacts (particularly near $I_S = 0$) due to re-trapping effects. This is reported in Fig. 5.18 where two features are clearly seen. First, the

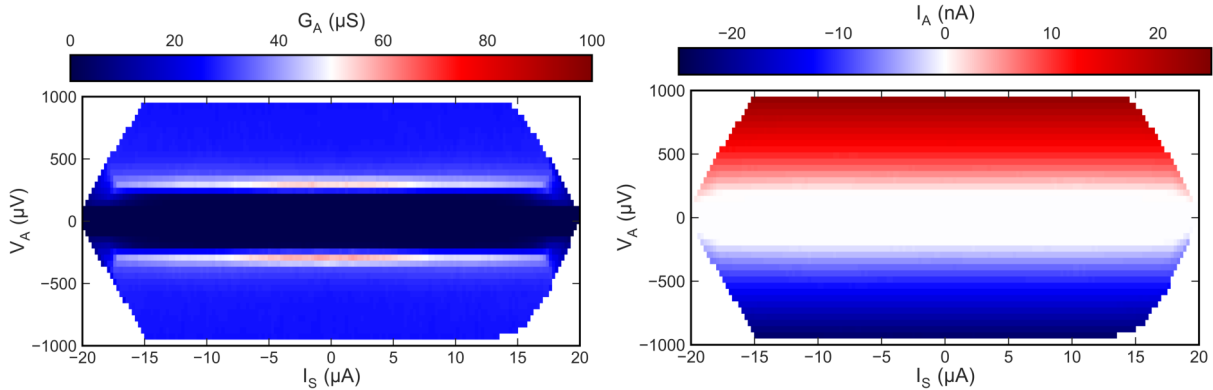


Figure 5.18: Local conductance and injector current measured during the application of a large supercurrent I_S along the superconducting wire. The regions without data indicate the normal state of the device, such that I_c is approximated by the boundaries of the data in this plot.

critical current itself is suppressed roughly linearly with V_A . Second, the subgap conductance is raised slightly at the highest supercurrent biases, and the magnitude of the local current increased correspondingly. These effects are likely related to the Doppler shift in the excitation energy for quasiparticles due to the superfluid velocity, as discussed in §2.3.2.

By performing the same measurement, but instead set fixed values for I_S , we can more clearly see the spectroscopic effects of the applied supercurrent on the quasiparticle density of states. This is shown in Fig. 5.19, where we can now more easily see the tapering in of the coherence peak maxima during I_S bias. Fitting this to a Dynes type model where Γ , T_e , and Δ are allowed to vary, we find a superficial correspondence with the picture discussed in §2.3.2, as Δ is suppressed by the application of the supercurrent and beyond a critical superfluid velocity $|v_{s,c}|$ a finite Γ term appears for $I_S \gtrsim 5 \mu\text{A}$. These fits are presented in left three panels of Fig. 5.20.

Taking a closer at the conductance spectra at high I_S bias however, it is clear that no *equilibrium* DOS could describe the data, as pronounced shoulders appear above the coherence peaks as shown in Fig. 5.20. This likely explains the large variations in T_e which would be un-physical as no heat

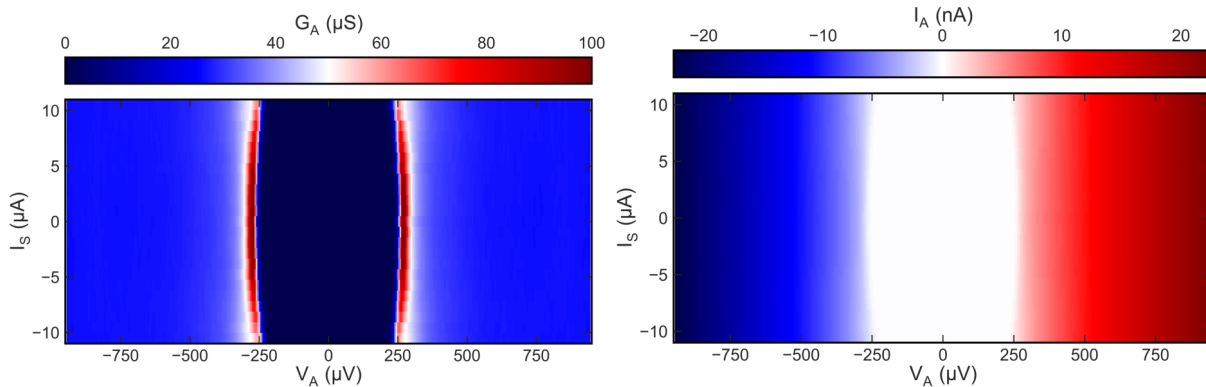


Figure 5.19: Local conductance and injector current remeasured at a smaller range of I_S values, as a function of V_A .

is dissipated in the normal metal electrodes during biasing in this fashion, as well as the linear trend in Γ/Δ_0 which matches poorly with theory. One possible explanation is during super-current injection, the role of the much larger superconducting reservoirs can no longer be ignored. There the supercurrent density will be much lower, and thus the gap will be less effected by the bias, leading to a proximity effect with the wire itself and a highly non-equilibrium spectrum of quasi-particles. This would require a rigorous quasi-classical treatment of the problem to decouple from

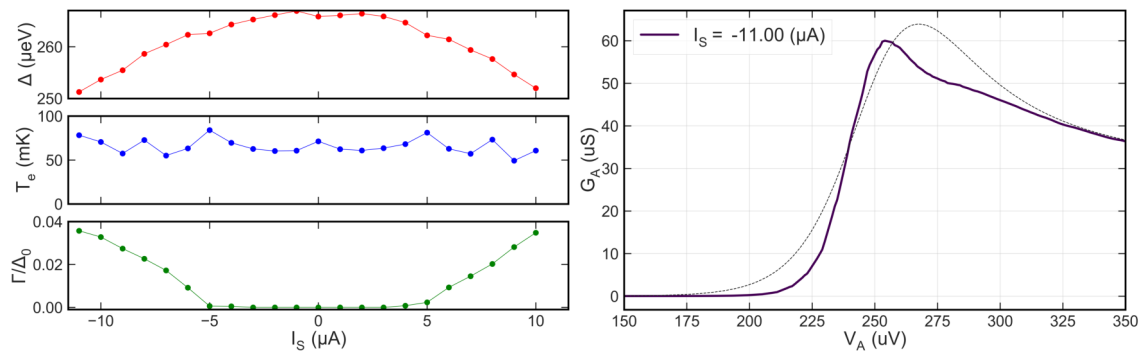


Figure 5.20: Left Panels: Fits to the local conductance shown in Fig. 5.19. Right Panel: Local conductance G_A at a large, subcritical supercurrent bias of $11 \mu\text{A}$ shown for the range about the positive V_A gap edge. The additional broadened shoulder above the coherence peak maxima is not seen at zero bias. The dashed lines indicate an equilibrium thermal fit with no Dynes parameter.

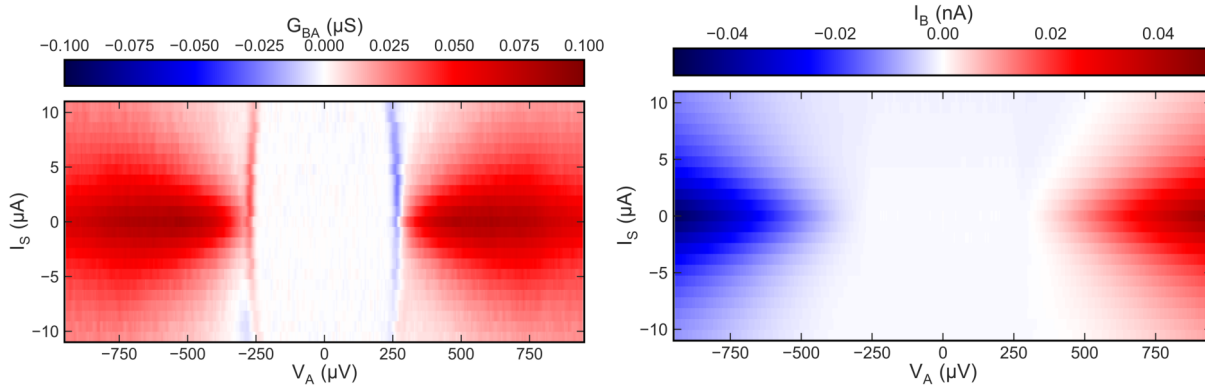


Figure 5.21: Non-local conductance and detector current measured over a range of I_S values, as a function of V_A .

the effect of the NIS junction bias, and makes examination of Doppler shift of E_k for quasiparticle states difficult.

This leads us to finally consider the mixing of the charge and energy non-equilibrium modes generated by NIS tunneling in the presence of a large I_S , with the caveat that the equilibrium quasiparticle distributions are no longer entirely BCS-like. Due to the contributions in the non-local conductance from both charge and energy mode non-equilibrium established in §5.3.1.1, this mixing is shown in Fig. 5.21 where we report both the non-local conductance and the detector current, measured simultaneously with the data in Fig. 5.19. Here, the non-local conductance is eminently a-symmetric, with a decaying charge mode contribution over a region $I_S \approx \pm 5 \mu\text{A}$ and an energy mode contribution as expected only at the gap edge.

Recalling from the kinetic terms of the Usadel equation, we expect that h_T and h_L distributions will be coupled linearly by the spectral supercurrent Q , although the exact forms of this are not obvious and would need to be solved numerically to understand the exact magnitude of this mixing. The charge imbalance component of G_{BA} is positive and symmetric with respect to the injector voltage and occurs only at $E_k \gg \Delta$, while the energy imbalance component is anti-symmetric with respect

to both voltage biases and appears in G_{BA} near $E_k \approx \Delta$. Under the assumption that a supercurrent bias will convert charge neutral quasiparticles into charged excitations, we posit that mixing from energy mode imbalance into charge mode will yield a component to G_{BA} which is anti-symmetric in I_S , while the unperturbed contributions will be symmetric under the same transformation. To check this, we decompose G_{BA} based on these symmetries in Fig. 5.22.

The components which are symmetric in I_S appear to be fairly clearly the ordinary charge and energy imbalance components of G_{BA} , and vary in I_S only through suppression of the gap and potentially increased charge mode relaxation. Taking the components which are anti-symmetric in I_S , we find there is very little symmetric signal with respect to V_A , while there is clearly an

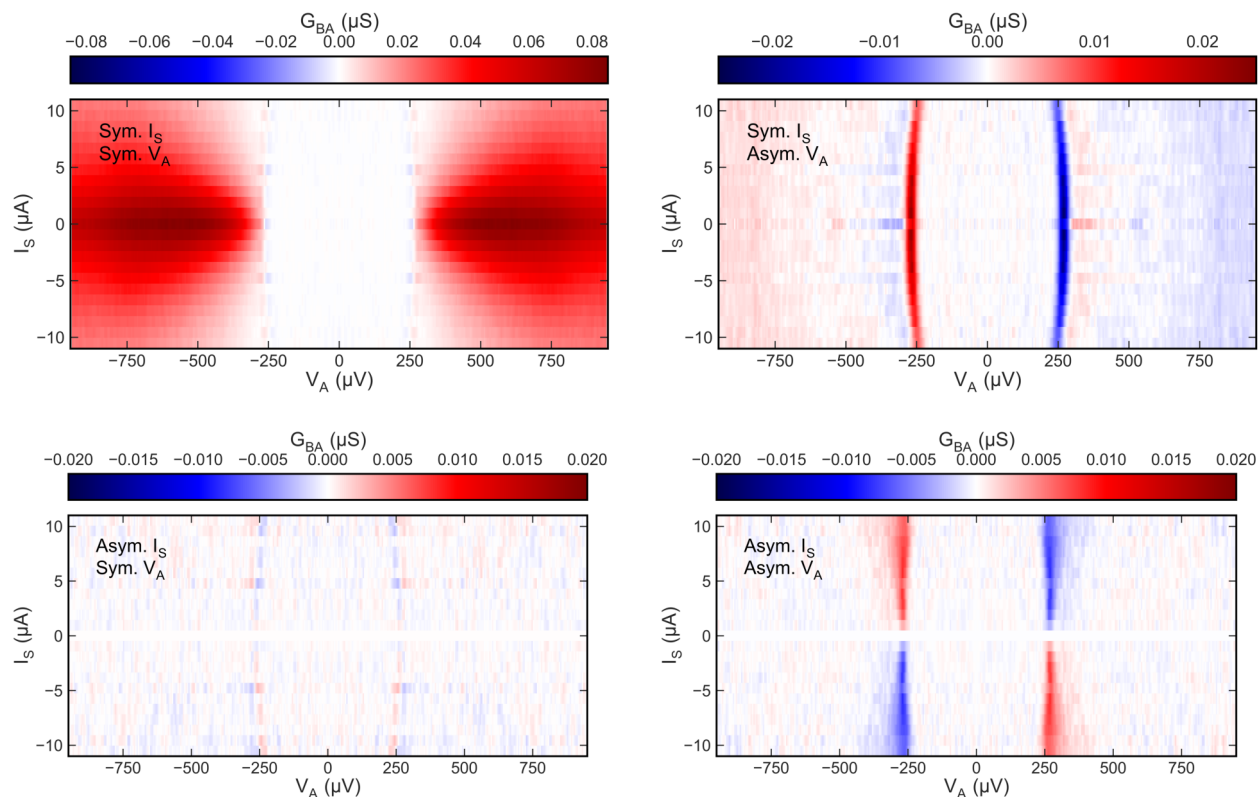


Figure 5.22: Symmetry decompositions of the I_S biased non-local conductance G_{BA} . Note the scale bars are not uniform to help clarify the general trends.

anti-symmetric signal that fans upwards in energy as the supercurrent is increased. While lacking a formal theory, we can deduce based on the energy ranges involved that the totally anti-symmetric component is that of excess charge imbalance generated by conversion of the energy imbalance mode via the supercurrent. Taking a step back, the four lobes seen here are cases where charge neutral quasiparticles are injected, but then converted to charged quasiparticles or quasi-holes by the supercurrent, thus modifying the charge imbalance. A corresponding charge-mode to energy-mode imbalance conversion does not appear to be discernible by the current method, or may be excluded in some manner by particle-hole symmetry. As taking this analysis further would require considerable theoretical development, we will conclude the analysis of non-equilibrium transport here.

CHAPTER 6

CONCLUSIONS AND FUTURE WORK

6.1 On Transport Measurements in Nb

Our studies of superconductivity in Nb films for SQMS have revealed a considerable degree of disorder in the materials used in quantum devices, despite in many cases being produced via state of the art fabrication methods. Inhomogeneity within Nb films, largely driven by film granularity and the pernicious Nb_2O_5 surface oxide, can be clearly seen in the superconducting phase boundary even when normal state properties of the films such as RRR or would tend to indicate a highly metallic nature. Similarly, there appear to be cases where improved crystallinity of the film (obtained via annealing or otherwise and observed via x-ray experiments) is not well correlated with strong or even uniform superconductivity. These findings also outline several broad considerations for the preparation of high quality superconducting Nb devices. Above all else, high temperature deposition via dc-sputtering is clearly preferable for producing Nb films of the highest quality. Conversely, ex-situ annealing is highly detrimental for T_c due to the dissolution of oxygen within the bulk of the film, despite the films being more generally uniform and crystalline. Vacuum conditions are also important for growth of Nb films at elevated temperatures, as any oxygen incorporation from the source material, out gassing or chamber leaks immediately degrade T_c and broaden the transition.

The $T_c - H_{c2}$ phase boundaries measured for Nb in our work are almost invariably non-linear, and the relationship between this curvature and material disorder seems likely. In heavily annealed

films, the linear phase boundary is restored at the cost of bulk superconductivity, and we expect that positive phase boundary curvature is a generic property of highly granular superconducting films. Positively curvature of the phase boundary near zero field may not inherently be an issue for quantum devices, as we have seen this fairly clearly in Nb films from Rigetti and NIST deposited under conditions used in state of the art qubits.

Future studies using the techniques described in this work may benefit from focusing on encapsulated materials such as Au encapsulated Nb, as these samples would have relatively fewer surface oxides and might clarify the issue of the GL phase boundary prediction for granular films. Conversely, the inverse proximity effect may be interesting to study in this manner, as it introduces a different type of inhomogeneity and will modify the shape of the resistive transition. The process used for ion milling presented here has successfully been used to etch Au, and this type of experiment could be readily performed. It may also be interesting to perform this type of measurement repeatedly on a single sample subject to repeated thermal cycling, vacuum annealing, chemical treatment or even radiation induced disorder or ion implantation to see more clearly how the phase boundary evolves under controlled disorder (outside of that generated during film growth).

6.2 On Quasiparticle Non-equilibrium

Quasiparticle transport experiments using NIS junctions at mK temperatures appear to reveal considerable information about non-equilibrium dynamics in superconductors in this regime. Very few direct experimental probes are available at these temperatures and with a similar degree of energy sensitivity, and only a handful of experiments of this type have been demonstrated recently. Our principle finding is demonstration of tunable inelastic quasiparticle relaxation independent of thermal phonons due to disorder induced electron-electron interactions. Inelastic relaxation leads to slower diffusion of quasiparticles, but as the material quality of the superconductor is improved,

fewer and fewer relaxation pathways will be available and quasiparticles will diffuse faster. Introducing some degree of disorder to slow this process, without compromising the superconductivity itself may thus be a useful pathway for future attempts to mitigate quasiparticle poisoning.

More fundamentally, we have seen that non-equilibrium charge and energy mode imbalance are both relevant for charge transport in NIS junctions, provided the correct experimental program is followed. By using independent biases, we have observed non-local conductance in mesoscopic devices with a energy resolution that has been previously unmatched in the literature. This is partly due to tight constraints we have uncovered for both the mechanical stability of TIA based experiments and for the degree of noise coupling for these types of measurements which should be performed with a minimum of extraneous junctions/connections. The chemical potential observed via equilibration of NIS junctions to non-equilibrium distributions of quasiparticles in our measurements appears to be entirely different from our expectations based on quasiparticle tunneling due to charge imbalance. This discrepancy continues as an unanswered question, as do the exact conditions required to see spin-splitting of quasiparticles in 1D wires, or the mechanisms by which sub-gap states begin to appear in more mesoscopic NIS junctions. Injection of a large supercurrent bias however appears to have a major effect on the non-local conductance seen by our method, and may spur interesting future work to understand this process via the Usadel equations, or to employ this in the context of more complex transport experiments. On a final note, the sensitivity of the non-local transport technique we have employed may be useful for an experiment examining the interference of partially charged quasiparticles due to Aharonov–Bohm effect, which has not yet been confidently observed and may be of considerable fundamental interest.

REFERENCES

- ¹Y. Nakamura, Y. A. Pashkin, and J. S. Tsai, “Coherent control of macroscopic quantum states in a single-Cooper-pair box”, *Nature* **398**, 786–788 (1999).
- ²T. A. Fulton and G. J. Dolan, “Observation of single-electron charging effects in small tunnel junctions”, *Physical Review Letters* **59**, 109–112 (1987).
- ³A. D. Zaikin, D. S. Golubev, A. van Otterlo, and G. T. Zimányi, “Quantum Phase Slips and Transport in Ultrathin Superconducting Wires”, *Physical Review Letters* **78**, 1552–1555 (1997).
- ⁴P. Joyez, P. Lafarge, A. Filipe, D. Esteve, and M. H. Devoret, “Observation of parity-induced suppression of Josephson tunneling in the superconducting single electron transistor”, *Physical Review Letters* **72**, 2458–2461 (1994).
- ⁵V. Bouchiat, D. Vion, P. Joyez, D. Esteve, and M. H. Devoret, “Quantum coherence with a single Cooper pair”, *Physica Scripta* **1998**, 165 (1998).
- ⁶A. Somoroff, Q. Ficheux, R. A. Mencia, H. Xiong, R. Kuzmin, and V. E. Manucharyan, “Millisecond Coherence in a Superconducting Qubit”, *Physical Review Letters* **130**, 267001 (2023).
- ⁷M. Smith, A. Leu, K. Miyanishi, M. Gely, and D. Lucas, “Single-Qubit Gates with Errors at the 10^{-7} Level”, *Physical Review Letters* **134**, 230601 (2025).
- ⁸A. Premkumar, C. Weiland, S. Hwang, B. Jaeck, A. P. M. Place, I. Waluyo, A. Hunt, V. Bisogni, J. Pellicciari, A. Barbour, M. S. Miller, P. Russo, F. Camino, K. Kisslinger, X. Tong, M. S. Hybertsen, A. A. Houck, and I. Jarrige, “Microscopic Relaxation Channels in Materials for Superconducting Qubits”, [arXiv:2004.02908](https://arxiv.org/abs/2004.02908) [cond-mat, physics:physics, physics:quant-ph] (2020).
- ⁹C. E. Murray, “Material matters in superconducting qubits”, *Materials Science and Engineering: R: Reports* **146**, 100646 (2021).
- ¹⁰A. M. J. Zwerver, T. Krähenmann, T. F. Watson, L. Lampert, H. C. George, R. Pillarisetty, S. A. Bojarski, P. Amin, S. V. Amitonov, J. M. Boter, R. Caudillo, D. Corras-Serrano, J. P. Dehollain, G. Droulers, E. M. Henry, R. Kotlyar, M. Lodari, F. Lüthi, D. J. Michalak, B. K. Mueller, S. Neyens, J. Roberts, N. Samkharadze, G. Zheng, O. K. Zietz, G. Scappucci, M.

- Veldhorst, L. M. K. Vandersypen, and J. S. Clarke, “Qubits made by advanced semiconductor manufacturing”, *Nature Electronics* **5**, 184–190 (2022).
- ¹¹A. Osman, J. Simon, A. Bengtsson, S. Kosen, P. Krantz, D. Perez, M. Scigliuzzo, J. Bylander, and A. F. Roudsari, “Simplified Josephson-junction fabrication process for reproducibly high-performance superconducting qubits”, [arXiv:2011.05230](https://arxiv.org/abs/2011.05230) (2020).
- ¹²A. A. Murthy, J. Lee, C. Kopas, M. J. Reagor, A. P. McFadden, D. P. Pappas, M. Checchin, A. Grassellino, and A. Romanenko, “TOF-SIMS analysis of decoherence sources in superconducting qubits”, *Applied Physics Letters* **120**, 044002 (2022).
- ¹³A. A. Murthy, P. M. Das, S. M. Ribet, C. Kopas, J. Lee, M. J. Reagor, L. Zhou, M. J. Kramer, M. C. Hersam, M. Checchin, A. Grassellino, R. d. Reis, V. P. Dravid, and A. Romanenko, “Potential Nanoscale Sources of Decoherence in Niobium based Transmon Qubit Architectures”, [arXiv:2203.08710 \[cond-mat, physics:quant-ph\]](https://arxiv.org/abs/2203.08710) (2022).
- ¹⁴K. Serniak, M. Hays, G. de Lange, S. Diamond, S. Shankar, L. Burkhardt, L. Frunzio, M. Houzet, and M. Devoret, “Hot Nonequilibrium Quasiparticles in Transmon Qubits”, *Physical Review Letters* **121**, 157701 (2018).
- ¹⁵K. Lang, S. Nam, J. Aumentado, C. Urbina, and J. Martinis, “Banishing quasiparticles from Josephson-junction qubits: Why and how to do it”, *IEEE Transactions on Applied Superconductivity* **13**, 989–993 (2003).
- ¹⁶E. T. Mannila, P. Samuelsson, S. Simbierowicz, J. T. Peltonen, V. Vesterinen, L. Grönberg, J. Hassel, V. F. Maisi, and J. P. Pekola, “A superconductor free of quasiparticles for seconds”, [arXiv:2102.00484 \[cond-mat, physics:quant-ph\]](https://arxiv.org/abs/2102.00484) (2021).
- ¹⁷J. M. Martinis, M. Ansmann, and J. Aumentado, “Energy Decay in Superconducting Josephson-Junction Qubits from Nonequilibrium Quasiparticle Excitations”, *Physical Review Letters* **103**, 097002 (2009).
- ¹⁸J. Aumentado, G. Catelani, and K. Serniak, “Quasiparticle poisoning in superconducting quantum computers”, *Physics Today* **76**, 34–39 (2023).
- ¹⁹M Saffman, “Quantum computing with atomic qubits and Rydberg interactions: progress and challenges”, *Journal of Physics B: Atomic, Molecular and Optical Physics* **49**, 202001 (2016).
- ²⁰C. Oh, “Recent Theoretical and Experimental Progress on Boson Sampling”, *Current Optics and Photonics* **9**, 1–18 (2025).

- ²¹M. Kjaergaard, M. E. Schwartz, J. Braumüller, P. Krantz, J. I.-J. Wang, S. Gustavsson, and W. D. Oliver, “Superconducting Qubits: Current State of Play”, [Annual Review of Condensed Matter Physics](#) **11**, 369–395 (2020).
- ²²G. Burkard, T. D. Ladd, A. Pan, J. M. Nichol, and J. R. Petta, “Semiconductor spin qubits”, [Reviews of Modern Physics](#) **95**, 025003 (2023).
- ²³L. Glazman and G. Catelani, “Bogoliubov quasiparticles in superconducting qubits”, [SciPost Physics Lecture Notes](#), 31 (2021).
- ²⁴G. Catelani, R. J. Schoelkopf, M. H. Devoret, and L. I. Glazman, “Relaxation and frequency shifts induced by quasiparticles in superconducting qubits”, [Physical Review B](#) **84**, 064517 (2011).
- ²⁵R. Shekhter, “Zero Anomalies in the Resistance of a Tunnel Junction Containing Metallic Inclusions in the Oxide Layer”, [Sov. Phys. JETP](#) **36**, 747 (1973).
- ²⁶L. I. Glazman and V. Chandrasekhar, “Coulomb Blockade Oscillations in a Double-Dot System”, [Europhysics Letters](#) **19**, 623 (1992).
- ²⁷J. Koch, T. M. Yu, J. Gambetta, A. A. Houck, D. I. Schuster, J. Majer, A. Blais, M. H. Devoret, S. M. Girvin, and R. J. Schoelkopf, “Charge-insensitive qubit design derived from the Cooper pair box”, [Physical Review A](#) **76**, 042319 (2007).
- ²⁸G. Catelani, “Parity switching and decoherence by quasiparticles in single-junction transmons”, [Physical Review B](#) **89**, 094522 (2014).
- ²⁹N. N. Bogoljubov, “On a new method in the theory of superconductivity”, [Il Nuovo Cimento \(1955-1965\)](#) **7**, 794–805 (1958).
- ³⁰M. Tinkham, *Introduction to superconductivity*, 2 ed, Dover books on physics (Dover Publ, Mineola, NY, 2015).
- ³¹C. J Pethick and H Smith, “Relaxation and collective motion in superconductors: a two-fluid description”, [Annals of Physics](#) **119**, 133–169 (1979).
- ³²J. Aumentado, M. W. Keller, J. M. Martinis, and M. H. Devoret, “Nonequilibrium Quasiparticles and $2e\Phi_0$ Periodicity in Single-Cooper-Pair Transistors”, [Physical Review Letters](#) **92**, 066802 (2004).

- ³³G. Catelani, L. I. Glazman, and K. E. Nagaev, “Effect of quasiparticles injection on the ac response of a superconductor”, *Physical Review B* **82**, 134502 (2010).
- ³⁴L. Sun, L. DiCarlo, M. D. Reed, G. Catelani, L. S. Bishop, D. I. Schuster, B. R. Johnson, G. A. Yang, L. Frunzio, L. Glazman, M. H. Devoret, and R. J. Schoelkopf, “Measurements of Quasiparticle Tunneling Dynamics in a Band-Gap-Engineered Transmon Qubit”, *Physical Review Letters* **108**, 230509 (2012).
- ³⁵D. Ristè, C. C. Bultink, M. J. Tiggelman, R. N. Schouten, K. W. Lehnert, and L. DiCarlo, “Millisecond charge-parity fluctuations and induced decoherence in a superconducting transmon qubit”, *Nature Communications* **4**, 1913 (2013).
- ³⁶C. Wang, Y. Y. Gao, I. M. Pop, U. Vool, C. Axline, T. Brecht, R. W. Heeres, L. Frunzio, M. H. Devoret, G. Catelani, L. I. Glazman, and R. J. Schoelkopf, “Measurement and control of quasiparticle dynamics in a superconducting qubit”, *Nature Communications* **5**, 5836 (2014).
- ³⁷R. Benevides, M. Drimmer, G. Bisson, F. Adinolfi, U. Lüpke, H. Doleman, G. Catelani, and Y. Chu, “Quasiparticle Dynamics in a Superconducting Qubit Irradiated by a Localized Infrared Source”, *Physical Review Letters* **133**, 060602 (2024).
- ³⁸S. Gustavsson, F. Yan, G. Catelani, J. Bylander, A. Kamal, J. Birenbaum, D. Hover, D. Rosenberg, G. Samach, A. P. Sears, S. J. Weber, J. L. Yoder, J. Clarke, A. J. Kerman, F. Yoshihara, Y. Nakamura, T. P. Orlando, and W. D. Oliver, “Suppressing relaxation in superconducting qubits by quasiparticle pumping”, *Science* **354**, 1573–1577 (2016).
- ³⁹T. Connolly, P. D. Kurilovich, S. Diamond, H. Nho, C. G. Bøttcher, L. I. Glazman, V. Fatemi, and M. H. Devoret, “Coexistence of Nonequilibrium Density and Equilibrium Energy Distribution of Quasiparticles in a Superconducting Qubit”, *Physical Review Letters* **132**, 217001 (2024).
- ⁴⁰D. S. Lvov, S. A. Lemziakov, E. Ankerhold, J. T. Peltonen, and J. P. Pekola, “Thermometry based on a superconducting qubit”, *Physical Review Applied* **23**, 054079 (2025).
- ⁴¹R. McDermott, “Materials Origins of Decoherence in Superconducting Qubits”, *IEEE Transactions on Applied Superconductivity* **19**, 2–13 (2009).
- ⁴²P. Krantz, M. Kjaergaard, F. Yan, T. P. Orlando, S. Gustavsson, and W. D. Oliver, “A quantum engineer’s guide to superconducting qubits”, *Applied Physics Reviews* **6**, 021318 (2019).

- ⁴³Z.-T. Zhang and Y. Yu, “Coupling mechanism between microscopic two-level system and superconducting qubits”, [Physical Review A **84**, 064301 \(2011\)](#).
- ⁴⁴R. W. Simmonds, K. M. Lang, D. A. Hite, S. Nam, D. P. Pappas, and J. M. Martinis, “Decoherence in Josephson Phase Qubits from Junction Resonators”, [Physical Review Letters **93**, 077003 \(2004\)](#).
- ⁴⁵L. V. Abdurakhimov, I. Mahboob, H. Toida, K. Kakuyanagi, Y. Matsuzaki, and S. Saito, “Identification of Different Types of High-Frequency Defects in Superconducting Qubits”, [PRX Quantum **3**, 040332 \(2022\)](#).
- ⁴⁶J. Lisenfeld, A. Bilmes, and A. V. Ustinov, “Enhancing the coherence of superconducting quantum bits with electric fields”, [npj Quantum Information **9**, 8 \(2023\)](#).
- ⁴⁷J. M. Martinis, K. B. Cooper, R. McDermott, M. Steffen, M. Ansmann, K. D. Osborn, K. Cicak, S. Oh, D. P. Pappas, R. W. Simmonds, and C. C. Yu, “Decoherence in Josephson Qubits from Dielectric Loss”, [Physical Review Letters **95**, 210503 \(2005\)](#).
- ⁴⁸Z. Wang, C. C. Yu, and R. Wu, “Why superconducting Ta qubits have fewer tunneling two-level systems at the vacuum-oxide interface than Nb qubits”, [Physical Review Applied **23**, 024017 \(2025\)](#).
- ⁴⁹M. Kristen, J. Voss, M. Wildermuth, A. Bilmes, J. Lisenfeld, H. Rotzinger, and A. Ustinov, “Giant Two-Level Systems in a Granular Superconductor”, [Physical Review Letters **132**, 217002 \(2024\)](#).
- ⁵⁰A. Lupaşcu, P. Bertet, E. F. C. Driessen, C. J. P. M. Harmans, and J. E. Mooij, “One- and two-photon spectroscopy of a flux qubit coupled to a microscopic defect”, [Physical Review B **80**, 172506 \(2009\)](#).
- ⁵¹J. Lisenfeld, G. J. Grabovskij, C. Müller, J. H. Cole, G. Weiss, and A. V. Ustinov, “Observation of directly interacting coherent two-level systems in an amorphous material”, [Nature Communications **6**, 6182 \(2015\)](#).
- ⁵²A. Bilmes, A. Megrant, P. Klimov, G. Weiss, J. M. Martinis, A. V. Ustinov, and J. Lisenfeld, “Resolving the positions of defects in superconducting quantum bits”, [Scientific Reports **10**, 3090 \(2020\)](#).
- ⁵³X.-X. Yang, X.-Y. Yang, L.-L. Guo, L. Du, P. Duan, Z.-L. Jia, H.-O. Li, and G.-P. Guo, “Locating Two-Level Systems in a Superconducting Xmon Qubit”, [Applied Sciences **13**, 6672 \(2023\)](#).

- ⁵⁴J. H. Cole, C. Müller, P. Bushev, G. J. Grabovskij, J. Lisenfeld, A. Lukashenko, A. V. Ustinov, and A. Shnirman, “Quantitative evaluation of defect-models in superconducting phase qubits”, [Applied Physics Letters](#) **97**, 252501 (2010).
- ⁵⁵S. E. de Graaf, L. Faoro, L. B. Ioffe, S. Mahashabde, J. J. Burnett, T. Lindström, S. E. Kubatkin, A. V. Danilov, and A. Y. Tzalenchuk, “Two-level systems in superconducting quantum devices due to trapped quasiparticles”, [Science Advances](#) **6**, eabc5055 (2020).
- ⁵⁶C. Carbillet, V. Cherkez, M. A. Skvortsov, M. V. Feigel’man, F. Debontridder, L. B. Ioffe, V. S. Stolyarov, K. Ilin, M. Siegel, D. Roditchev, T. Cren, and C. Brun, “Spectroscopic evidence for strong correlations between local superconducting gap and local Altshuler-Aronov density of states suppression in ultrathin NbN films”, [Physical Review B](#) **102**, 024504 (2020).
- ⁵⁷G. Berti, C. G. Torres-Castanedo, D. P. Goronzy, M. J. Bedzyk, M. C. Hersam, C. Kopas, J. Marshall, and M. Iavarone, “Scanning tunneling microscopy and spectroscopy characterization of Nb films for quantum applications”, [Applied Physics Letters](#) **122**, 192605 (2023).
- ⁵⁸C. Song, T. W. Heitmann, M. P. DeFeo, K. Yu, R. McDermott, M. Neeley, J. M. Martinis, and B. L. T. Plourde, “Microwave response of vortices in superconducting thin films of Re and Al”, [Physical Review B](#) **79**, 174512 (2009).
- ⁵⁹W. Chen, M. Abbasi, Y. N. Joglekar, and K. W. Murch, “Quantum Jumps in the Non-Hermitian Dynamics of a Superconducting Qubit”, [Physical Review Letters](#) **127**, 140504 (2021).
- ⁶⁰Y. Choi, S. N. Coppersmith, and R. Joynt, “Using stochastic resonance of two-level systems to increase qubit coherence times”, [Physical Review A](#) **110**, 052408 (2024).
- ⁶¹L. N. Cooper, “Bound Electron Pairs in a Degenerate Fermi Gas”, [Physical Review](#) **104**, 1189–1190 (1956).
- ⁶²N. W. Ashcroft and N. D. Mermin, *Solid State Physics* (Saunders College, Philadelphia, 1976).
- ⁶³J. N. Ullom, P. A. Fisher, and M. Nahum, “Energy-dependent quasiparticle group velocity in a superconductor”, [Physical Review B](#) **58**, 8225–8228 (1998).
- ⁶⁴S. A. Kivelson and D. S. Rokhsar, “Bogoliubov quasiparticles, spinons, and spin-charge decoupling in superconductors”, [Physical Review B](#) **41**, 11693–11696 (1990).
- ⁶⁵Q. Si, “Spin Conductivity and Spin-Charge Separation in the High- T_c Cuprates”, [Physical Review Letters](#) **78**, 1767–1770 (1997).

- ⁶⁶S. A. Parameswaran, S. A. Kivelson, R. Shankar, S. L. Sondhi, and B. Z. Spivak, “Microscopic Model of Quasiparticle Wave Packets in Superfluids, Superconductors, and Paired Hall States”, *Physical Review Letters* **109**, 237004 (2012).
- ⁶⁷N. Mason and M. Stehno, “No charge for spin transport”, *Nature Physics* **9**, 67–68 (2013).
- ⁶⁸C. H. L. Quay and M. Aprili, “Out-of-equilibrium spin transport in mesoscopic superconductors”, *Philosophical Transactions of the Royal Society A: Mathematical, Physical and Engineering Sciences* **376**, 20150342 (2018).
- ⁶⁹G. Yang, C. Ciccarelli, and J. W. A. Robinson, “Boosting spintronics with superconductivity”, *APL Materials* **9**, 050703 (2021).
- ⁷⁰Y. Ronen, Y. Cohen, J.-H. Kang, A. Haim, M.-T. Rieder, M. Heiblum, D. Mahalu, and H. Shtrikman, “Charge of a quasiparticle in a superconductor”, *Proceedings of the National Academy of Sciences* **113**, 1743–1748 (2016).
- ⁷¹H. Pothier, S. Guéron, D. Esteve, and M. H. Devoret, “Flux-Modulated Andreev Current Caused by Electronic Interference”, *Physical Review Letters* **73**, 2488–2491 (1994).
- ⁷²K. Y. Arutyunov, A. S. Gurskiy, E. P. Pozdnyakova, D. L. Shapovalov, G.-W. Deng, A. M. Chekushkin, M. A. Markina, and M. A. Tarasov, “Normal Metal–Insulator–Superconductor Aharonov-Bohm Interferometer”, *Journal of Superconductivity and Novel Magnetism* **37**, 1913–1916 (2024).
- ⁷³F. W. J. Hekking and Y. V. Nazarov, “Subgap conductivity of a superconductor–normal-metal tunnel interface”, *Physical Review B* **49**, 6847–6852 (1994).
- ⁷⁴R. Meservey and P. M. Tedrow, “Spin-polarized electron tunneling”, *Physics Reports* **238**, 173–243 (1994).
- ⁷⁵R. C. Dynes, V. Narayanamurti, and J. P. Garno, “Direct Measurement of Quasiparticle-Lifetime Broadening in a Strong-Coupled Superconductor”, *Physical Review Letters* **41**, 1509–1512 (1978).
- ⁷⁶G. Webb, F. Marsiglio, and J. Hirsch, “Superconductivity in the elements, alloys and simple compounds”, *Physica C: Superconductivity and its Applications* **514**, 17–27 (2015).
- ⁷⁷H. Kurkjian and J. Tempere, “Absorption and emission of a collective excitation by a fermionic quasiparticle in a Fermi superfluid”, *New Journal of Physics* **19**, 113045 (2017).

- ⁷⁸S. B. Kaplan, C. C. Chi, D. N. Langenberg, J. J. Chang, S. Jafarey, and D. J. Scalapino, “Quasiparticle and phonon lifetimes in superconductors”, *Physical Review B* **14**, 4854–4873 (1976).
- ⁷⁹A. D. Córcoles, J. M. Chow, J. M. Gambetta, C. Rigetti, J. R. Rozen, G. A. Keefe, M. Beth Rothwell, M. B. Ketchen, and M. Steffen, “Protecting superconducting qubits from radiation”, *Applied Physics Letters* **99**, 181906 (2011).
- ⁸⁰R. Barends, J. Wenner, M. Lenander, Y. Chen, R. C. Bialczak, J. Kelly, E. Lucero, P. O’Malley, M. Mariantoni, D. Sank, H. Wang, T. C. White, Y. Yin, J. Zhao, A. N. Cleland, J. M. Martinis, and J. J. A. Baselmans, “Minimizing quasiparticle generation from stray infrared light in superconducting quantum circuits”, *Applied Physics Letters* **99**, 113507 (2011).
- ⁸¹M. Houzet, K. Serniak, G. Catelani, M. Devoret, and L. Glazman, “Photon-Assisted Charge-Parity Jumps in a Superconducting Qubit”, *Physical Review Letters* **123**, 107704 (2019).
- ⁸²C. Liu, D. Harrison, S. Patel, C. Wilen, O. Rafferty, A. Shearrow, A. Ballard, V. Iaia, J. Ku, B. Plourde, and R. McDermott, “Quasiparticle Poisoning of Superconducting Qubits from Resonant Absorption of Pair-Breaking Photons”, *Physical Review Letters* **132**, 017001 (2024).
- ⁸³R. Anthony-Petersen, A. Biekert, R. Bunker, C. L. Chang, Y.-Y. Chang, L. Chaplinsky, E. Fascione, C. W. Fink, M. Garcia-Sciveres, R. Germond, W. Guo, S. A. Hertel, Z. Hong, N. Kurinsky, X. Li, J. Lin, M. Lisovenko, R. Mahapatra, A. Mayer, D. N. McKinsey, S. Mehrotra, N. Mirabolfathi, B. Neblosky, W. A. Page, P. K. Patel, B. Penning, H. D. Pinckney, M. Platt, M. Pyle, M. Reed, R. K. Romani, H. Santana Queiroz, B. Sadoulet, B. Serfass, R. Smith, P. Sorensen, B. Suerfu, A. Suzuki, R. Underwood, V. Velan, G. Wang, Y. Wang, S. L. Watkins, M. R. Williams, V. Yefremenko, and J. Zhang, “A stress-induced source of phonon bursts and quasiparticle poisoning”, *Nature Communications* **15**, 6444 (2024).
- ⁸⁴A. P. Vepsäläinen, A. H. Karamlou, J. L. Orrell, A. S. Dogra, B. Loer, F. Vasconcelos, D. K. Kim, A. J. Melville, B. M. Niedzielski, J. L. Yoder, S. Gustavsson, J. A. Formaggio, B. A. VanDevender, and W. D. Oliver, “Impact of ionizing radiation on superconducting qubit coherence”, *Nature* **584**, 551–556 (2020).
- ⁸⁵J. M. Martinis, “Saving superconducting quantum processors from decay and correlated errors generated by gamma and cosmic rays”, *npj Quantum Information* **7**, 90 (2021).
- ⁸⁶C. D. Wilen, S. Abdullah, N. A. Kurinsky, C. Stanford, L. Cardani, G. D’Imperio, C. Tomei, L. Faoro, L. B. Ioffe, C. H. Liu, A. Opremcak, B. G. Christensen, J. L. DuBois, and R. McDermott, “Correlated charge noise and relaxation errors in superconducting qubits”, *Nature* **594**, 369–373 (2021).

- ⁸⁷P. Kumar, S. Sendelbach, M. Beck, J. Freeland, Z. Wang, H. Wang, C. C. Yu, R. Wu, D. Pappas, and R. McDermott, “Origin and Reduction of $1/f$ Magnetic Flux Noise in Superconducting Devices”, *Physical Review Applied* **6**, 041001(R) (2016).
- ⁸⁸M. V. P. Altoé, A. Banerjee, C. Berk, A. Hajr, A. Schwartzberg, C. Song, M. Alghadeer, S. Aloni, M. J. Elowson, J. M. Kreikebaum, E. K. Wong, S. M. Griffin, S. Rao, A. Weber-Bargioni, A. M. Minor, D. I. Santiago, S. Cabrini, I. Siddiqi, and D. F. Ogletree, “Localization and Mitigation of Loss in Niobium Superconducting Circuits”, *PRX Quantum* **3**, 020312 (2022).
- ⁸⁹P. J. Hirschfeld, P. Wölfle, J. A. Sauls, D. Einzel, and W. O. Putikka, “Electromagnetic absorption in anisotropic superconductors”, *Physical Review B* **40**, 6695–6710 (1989).
- ⁹⁰M. A. Tanatar, D. Torsello, K. R. Joshi, S. Ghimire, C. J. Kopas, J. Marshall, J. Y. Mutus, G. Ghigo, M. Zarea, J. A. Sauls, and R. Prozorov, “Anisotropic superconductivity of niobium based on its response to nonmagnetic disorder”, *Physical Review B* **106**, 224511 (2022).
- ⁹¹M. Zarea, H. Ueki, and J. A. Sauls, “Effects of anisotropy and disorder on the superconducting properties of niobium”, *Frontiers in Physics* **11** (2023).
- ⁹²J. Clarke, “Experimental Observation of Pair-Quasiparticle Potential Difference in Nonequilibrium Superconductors”, *Physical Review Letters* **28**, 1363–1366 (1972).
- ⁹³M. Tinkham and J. Clarke, “Theory of Pair-Quasiparticle Potential Difference in Nonequilibrium Superconductors”, *Physical Review Letters* **28**, 1366–1369 (1972).
- ⁹⁴K. E. Gray, “Enhancement of superconductivity by quasiparticle tunneling”, *Solid State Communications* **26**, 633–635 (1978).
- ⁹⁵G. E. Blonder, M. Tinkham, and T. M. Klapwijk, “Transition from metallic to tunneling regimes in superconducting microconstrictions: Excess current, charge imbalance, and supercurrent conversion”, *Physical Review B* **25**, 4515–4532 (1982).
- ⁹⁶F. Giazotto, T. T. Heikkilä, A. Luukanen, A. M. Savin, and J. P. Pekola, “Opportunities for mesoscopies in thermometry and refrigeration: Physics and applications”, *Reviews of Modern Physics* **78**, 217–274 (2006).
- ⁹⁷A. Feshchenko, L. Casparis, I. Khaymovich, D. Maradan, O.-P. Saira, M. Palma, M. Meschke, J. Pekola, and D. Zumbühl, “Tunnel-Junction Thermometry Down to Millikelvin Temperatures”, *Physical Review Applied* **4**, 034001 (2015).

- ⁹⁸M. Tinkham, “Tunneling Generation, Relaxation, and Tunneling Detection of Hole-Electron Imbalance in Superconductors”, *Physical Review B* **6**, 1747–1756 (1972).
- ⁹⁹D. M. Ginsberg, “Upper Limit for Quasi-Particle Recombination Time in a Superconductor”, *Physical Review Letters* **8**, 204–207 (1962).
- ¹⁰⁰B. I. Miller and A. H. Dayem, “Relaxation and Recombination Times of Quasiparticles in Superconducting Al Thin Films”, *Physical Review Letters* **18**, 1000–1004 (1967).
- ¹⁰¹C. C. Chi and J. Clarke, “Quasiparticle branch mixing rates in superconducting aluminum”, *Physical Review B* **19**, 4495–4509 (1979).
- ¹⁰²C. C. Chi and J. Clarke, “Addendum to ”Quasiparticle branch mixing rates in superconducting aluminum””, *Physical Review B* **21**, 333–337 (1980).
- ¹⁰³T. R. Lemberger and J. Clarke, “Charge-imbalance relaxation in the presence of a pair-breaking interaction in superconducting AlEr films”, *Physical Review B* **23**, 1088–1099 (1981).
- ¹⁰⁴A. Schmid, “Stability of Radiation-Stimulated Superconductivity”, *Physical Review Letters* **38**, 922–925 (1977).
- ¹⁰⁵A. Schmid and G. Schön, “Linearized kinetic equations and relaxation processes of a superconductor near T_c ”, *Journal of Low Temperature Physics* **20**, 207–227 (1975).
- ¹⁰⁶G. Eilenberger, “Transformation of Gorkov’s equation for type II superconductors into transport-like equations”, *Zeitschrift für Physik A Hadrons and nuclei* **214**, 195–213 (1968).
- ¹⁰⁷V. Chandrasekhar, “Proximity-Coupled Systems: Quasiclassical Theory of Superconductivity”, in *Superconductivity: Conventional and Unconventional Superconductors*, edited by K. H. Bennemann and J. B. Ketterson (Springer, Berlin, Heidelberg, 2008), pp. 279–313.
- ¹⁰⁸K. D. Usadel, “Generalized Diffusion Equation for Superconducting Alloys”, *Physical Review Letters* **25**, 507–509 (1970).
- ¹⁰⁹M. Y. Kurpianov and V. F. Lukichev, “Influence of boundary transparency on the critical current of dirty SS’S structures”, **67**, 1163–1168 (1988).
- ¹¹⁰F. S. Bergeret, M. Silaev, P. Virtanen, and T. T. Heikkilä, “Colloquium: Nonequilibrium effects in superconductors with a spin-splitting field”, *Reviews of Modern Physics* **90**, 041001 (2018).

- ¹¹¹T. T. Heikkilä, M. Silaev, P. Virtanen, and F. S. Bergeret, “Thermal, electric and spin transport in superconductor/ferromagnetic-insulator structures”, *Progress in Surface Science* **94**, 100540 (2019).
- ¹¹²F. London and H. London, “The electromagnetic equations of the supraconductor”, *Proceedings of the Royal Society of London. Series A - Mathematical and Physical Sciences* **149**, 71–88 (1935).
- ¹¹³N. Ashcroft and N. Mermin, *Solid state physics* (Cengage Learning, 2011).
- ¹¹⁴D. Gennes and P. G, “Superconductivity of metals and alloys”, (1965).
- ¹¹⁵A. Leggett, *Lecture Notes, Superconducting alloys: electromagnetic response of clean and dirty superconductors*, 2015.
- ¹¹⁶P. W. Anderson, “Theory of dirty superconductors”, *Journal of Physics and Chemistry of Solids* **11**, 26–30 (1959).
- ¹¹⁷P. Ferrari, S. Rojas, D. E. Diaz-Droguett, and A. L. Cabrera, “EVAPORATION OF LOW-VAPOR PRESSURE METALS USING A CONVENTIONAL MINI ELECTRON BEAM EVAPORATOR”, *Instrumentation Science & Technology* **42**, 142–152 (2014).
- ¹¹⁸K. Zhang, M. Wen, G. Cheng, X. Li, Q. Meng, J. Lian, and W. Zheng, “Reactive magnetron sputtering deposition and characterization of niobium carbide films”, *Vacuum* **99**, 233–241 (2014).
- ¹¹⁹M. P. Arbutov and V. G. Chuprina, “The oxidation of niobium and the structure of niobium oxides”, *Soviet Physics Journal* **8**, 87–89 (1966).
- ¹²⁰B. G. C. Bos, D. J. Thoen, E. A. F. Haalebos, P. M. L. Gimbel, T. M. Klapwijk, J. J. A. Baselmans, and A. Endo, “Reactive Magnetron Sputter Deposition of Superconducting Niobium Titanium Nitride Thin Films With Different Target Sizes”, *IEEE Transactions on Applied Superconductivity* **27**, 1–5 (2017).
- ¹²¹J. Halbritter, “ARXPS analysis and oxidation of niobium compounds”, *Electrochimica Acta* **34**, 1153–1155 (1989).
- ¹²²F. Barkov, A. Romanenko, and A. Grassellino, “Direct observation of hydrides formation in cavity-grade niobium”, *Physical Review Special Topics - Accelerators and Beams* **15**, 122001 (2012).

- ¹²³K. H. Bennemann and J. B. Ketterson, eds., *Superconductivity* (Springer Berlin Heidelberg, Berlin, Heidelberg, 2008).
- ¹²⁴E. L. Wolf, J. Zasadzinski, J. W. Osmun, and G. B. Arnold, “Proximity electron tunneling spectroscopy I. Experiments on Nb”, *Journal of Low Temperature Physics* **40**, 19–50 (1980).
- ¹²⁵C. P. Koçer, K. J. Griffith, C. P. Grey, and A. J. Morris, “First-principles study of localized and delocalized electronic states in crystallographic shear phases of niobium oxide”, *Physical Review B* **99**, 075151 (2019).
- ¹²⁶A. A. Murthy, P. M. Das, S. M. Ribet, C. Kopas, J. Lee, M. J. Reagor, L. Zhou, M. J. Kramer, M. C. Hersam, M. Checchin, A. Grassellino, R. d. Reis, V. P. Dravid, and A. Romanenko, *Insights into Improving Performance of Niobium Superconducting Transmon Qubit Devices through Advanced Microscopy*, tech. rep. arXiv:2203.08710 (arXiv, May 2022).
- ¹²⁷J. Verjauw, A. Potočnik, M. Mongillo, R. Acharya, F. Mohiyaddin, G. Simion, A. Pacco, T. Ivanov, D. Wan, A. Vanleenhove, L. Souriau, J. Jussot, A. Thiam, J. Swerts, X. Piao, S. Couet, M. Heyns, B. Govoreanu, and I. Radu, “Investigation of Microwave Loss Induced by Oxide Regrowth in High- Q Niobium Resonators”, *Physical Review Applied* **16**, 014018 (2021).
- ¹²⁸E. Sheridan, T. F. Harrelson, E. Sivonxay, K. A. Persson, M. V. P. Altoé, I. Siddiqi, D. F. Ogle-tree, D. I. Santiago, and S. M. Griffin, “Microscopic Theory of Magnetic Disorder-Induced Decoherence in Superconducting Nb Films”, arXiv:2111.11684 [cond-mat, physics:quant-ph] (2021).
- ¹²⁹B. W. Roberts, “Survey of superconductive materials and critical evaluation of selected properties”, *Journal of Physical and Chemical Reference Data* **5**, 581–822 (1976).
- ¹³⁰L. Y. L. Shen, N. M. Senozan, and N. E. Phillips, “Evidence for Two Energy Gaps in High-Purity Superconducting Nb, Ta, and V”, *Physical Review Letters* **14**, 1025–1027 (1965).
- ¹³¹A. Ikushima and T. Mizusaki, “Superconductivity in niobium and niobium-tantalum alloys”, *Journal of Physics and Chemistry of Solids* **30**, 873–879 (1969).
- ¹³²X. Zheng and D. Walmsley, “Visualised predictions of gap anisotropy to test new electron pairing scheme”, *Physica C: Superconductivity and its Applications* **534**, 19–28 (2017).
- ¹³³A. Oota and Y. Masuda, “Investigation of Thermal Conductivity of Nb within the Framework of Strong Coupling Theory”, *Journal of the Physical Society of Japan* **41**, 434–441 (1976).

- ¹³⁴J. Bostock, K. H. Lo, W. N. Cheung, V. Diadiuk, and M. L. A. MacVicar, “Superconductivity in Niobium: Implications for Strong Coupling Superconductivity Theory”, in *Superconductivity in d- and f-Band Metals: Second Rochester Conference*, edited by D. H. Douglass (Springer US, Boston, MA, 1976), pp. 367–380.
- ¹³⁵J. Bostock, V. Diadiuk, W. N. Cheung, K. H. Lo, R. M. Rose, and M. L. A. Mac Vicar, “Does Strong-Coupling Theory Describe Superconducting Nb?”, *Physical Review Letters* **36**, 603–606 (1976).
- ¹³⁶J. Bostock, V. Diadiuk, W. N. Cheung, K. H. Lo, R. M. Rose, and M. L. A. Macvicar, “Determination of the superconducting strong-coupling microscopic parameters of Nb by electron tunneling”, *Ferroelectrics* **16**, 249–252 (1977).
- ¹³⁷W. H. Butler, F. J. Pinski, and P. B. Allen, “Phonon linewidths and electron-phonon interaction in Nb”, *Physical Review B* **19**, 3708–3721 (1979).
- ¹³⁸C. J. Thompson, M. F. Van Duinen, M. M. Kelley, T. A. Arias, and S. J. Sibener, “Correlating Electron–Phonon Coupling and In Situ High-Temperature Atomic-Scale Surface Structure at the Metallic Nb(100) Surface by Helium Atom Scattering and Density Functional Theory”, *The Journal of Physical Chemistry C* **128**, 6149–6157 (2024).
- ¹³⁹A. Calverley, A. C. Rose-Innes, and K. A. G. Mendelssohn, “Trapped flux in superconducting mixed-crystals”, *Proceedings of the Royal Society of London. Series A. Mathematical and Physical Sciences* **255**, 267–276 (1997).
- ¹⁴⁰R. A. French, “Intrinsic type-2 superconductivity in pure niobium”, *Cryogenics* **8**, 301–308 (1968).
- ¹⁴¹R. Prozorov, M. Zarea, and J. A. Sauls, “Niobium in the clean limit: An intrinsic type-I superconductor”, *Physical Review B* **106**, L180505 (2022).
- ¹⁴²C. C. Koch, J. O. Scarbrough, and D. M. Kroeger, “Effects of interstitial oxygen on the superconductivity of niobium”, *Physical Review B* **9**, 888–897 (1974).
- ¹⁴³J. Bardeen, “Critical Fields and Currents in Superconductors”, *Reviews of Modern Physics* **34**, 667–681 (1962).
- ¹⁴⁴G. E. VOLOVIK, “Superconductivity with lines of GAP nodes: density of states in the vortex”, *Superconductivity with lines of GAP nodes: density of states in the vortex* **58**, 469–473 (1993).

- ¹⁴⁵C. Kübert and P. J. Hirschfeld, “Vortex contribution to specific heat of dirty *d*-wave superconductors: Breakdown of scaling”, *Solid State Communications* **105**, 459–463 (1998).
- ¹⁴⁶A. Anthore, H. Pothier, and D. Esteve, “Density of States in a Superconductor Carrying a Supercurrent”, *Physical Review Letters* **90**, 127001 (2003).
- ¹⁴⁷C. J. Pethick and H. Smith, “Generation of Charge Imbalance in a Superconductor by a Temperature Gradient”, *Physical Review Letters* **43**, 640–642 (1979).
- ¹⁴⁸J. Clarke and M. Tinkham, “Theory of Quasiparticle Charge Imbalance Induced in a Superconductor by a Supercurrent in the Presence of a Thermal Gradient”, *Physical Review Letters* **44**, 106–109 (1980).
- ¹⁴⁹F. Aikebaier, M. A. Silaev, and T. T. Heikkilä, “Supercurrent-induced charge-spin conversion in spin-split superconductors”, *Physical Review B* **98**, 024516 (2018).
- ¹⁵⁰V. V. Bal, Z. Huang, K. Han, Ariando, T. Venkatesan, and V. Chandrasekhar, “Low-temperature magnetoresistance of (111) (La_{0.3}Sr_{0.7})(Al_{0.65}Ta_{0.35})O₃/SrTiO₃”, *Physical Review B* **99**, 035408 (2019).
- ¹⁵¹K. M. Ryan and V. Chandrasekhar, “Enhanced quasiparticle relaxation in a superconductor via the proximity effect”, *Applied Physics Letters* **127**, 072603 (2025).
- ¹⁵²B. Cord, C. Dames, K. K. Berggren, and J. Aumentado, “Robust shadow-mask evaporation via lithographically controlled undercut”, *Journal of Vacuum Science & Technology B: Microelectronics and Nanometer Structures Processing, Measurement, and Phenomena* **24**, 3139–3143 (2006).
- ¹⁵³T. T. Foxe, B. D. Hunt, C. Rogers, A. W. Kleinsasser, and R. A. Buhrman, “Reactive ion etching of niobium”, *Journal of Vacuum Science and Technology* **19**, 1394–1397 (1981).
- ¹⁵⁴J.-H. Huh, C. Hermannstädter, H. Sato, S. Ito, Y. Idutsu, H. Sasakura, K. Tanaka, T. Akazaki, and I. Suemune, “Precise slit-width control of niobium apertures for superconducting LEDs”, *Nanotechnology* **22**, 045302 (2011).
- ¹⁵⁵A. A. Hossain, S. Murphy, D. S. Catherall, A. J. Ardizzi, and A. J. Minnich, “Atomic layer etching of niobium nitride using sequential exposures of O₂ and H₂/SF₆ plasmas”, *Journal of Vacuum Science & Technology A* **43**, 042605 (2025).

- ¹⁵⁶M. De Lucia, P. Dal Bo, E. Di Giorgi, T. Lari, C. Puglia, and F. Paolucci, “Transition Edge Sensors: Physics and Applications”, *Instruments* **8**, 47 (2024).
- ¹⁵⁷K. M. Ryan, C. G. Torres-Castanedo, D. P. Goronzy, D. A. G. Wetten, M. Field, C. J. Kopas, J. Marshall, M. J. Reagor, M. J. Bedzyk, M. C. Hersam, and V. Chandrasekhar, “Characterization of Nb films for superconducting qubits using phase boundary measurements”, *Applied Physics Letters* **121**, 202601 (2022).
- ¹⁵⁸J. G. Adler and J. E. Jackson, “System for Observing Small Nonlinearities in Tunnel Junctions”, *Review of Scientific Instruments* **37**, 1049–1054 (1966).
- ¹⁵⁹H. Vloeberghs, V. V. Moshchalkov, C. Van Haesendonck, R. Jonckheere, and Y. Bruynseraede, “Anomalous Little-Parks oscillations in mesoscopic loops”, *Phys. Rev. Lett.* **69**, 1268–1271 (1992).
- ¹⁶⁰M. Mehta, “Interplay between superconductivity and ferromagnetism at the LaAlO₃/SrTiO₃ interface”, PhD Thesis (2015).
- ¹⁶¹D. A. Dikin, V. Chandrasekhar, V. R. Misko, V. M. Fomin, and J. T. Devreese, “Nucleation of superconductivity in mesoscopic star-shaped superconductors”, *The European Physical Journal B - Condensed Matter* **34**, 231–235 (2003).
- ¹⁶²N. Pinto, S. J. Rezvani, A. Perali, L. Flammia, M. V. Milošević, M. Fretto, C. Cassiago, and N. De Leo, “Dimensional crossover and incipient quantum size effects in superconducting niobium nanofilms”, *Scientific Reports* **8**, 4710 (2018).
- ¹⁶³S. Ganjam, Y. Wang, Y. Lu, A. Banerjee, C. U. Lei, L. Krayzman, K. Kisslinger, C. Zhou, R. Li, Y. Jia, M. Liu, L. Frunzio, and R. J. Schoelkopf, “Surpassing millisecond coherence in on chip superconducting quantum memories by optimizing materials and circuit design”, *Nature Communications* **15**, 3687 (2024).
- ¹⁶⁴A. Wildes, J. Mayer, and K. Theis-Bröhl, “The growth and structure of epitaxial niobium on sapphire”, *Thin Solid Films* **401**, 7–34 (2001).
- ¹⁶⁵D. K. Finnemore, T. F. Stromberg, and C. A. Swenson, “Superconducting Properties of High-Purity Niobium”, *Physical Review* **149**, 231–243 (1966).
- ¹⁶⁶V. Kozhevnikov, A.-M. Valente-Feliciano, P. J. Curran, G. Richter, A. Volodin, A. Suter, S. J. Bending, and C. Van Haesendonck, “Equilibrium Properties of the Mixed State in Supercon-

- ducting Niobium in a Transverse Magnetic Field: Experiment and Theoretical Model”, [Journal of Superconductivity and Novel Magnetism](#) **31**, 3433–3444 (2018).
- ¹⁶⁷A. V. Narlikar and D. Dew-Hughes, “Superconductivity in deformed niobium alloys”, [Journal of Materials Science](#) **1**, 317–335 (1966).
- ¹⁶⁸X. Lu, D. P. Goronzy, C. G. Torres-Castanedo, P. Masih Das, M. Kazemzadeh-Atoufi, A. McFadden, C. R. H. McRae, P. W. Voorhees, V. P. Dravid, M. J. Bedzyk, M. C. Hersam, and J. M. Rondinelli, “Stability, metallicity, and magnetism in niobium silicide nanofilms”, [Physical Review Materials](#) **6**, 064402 (2022).
- ¹⁶⁹B. Cao, M. Yang, J. Chen, M. Liang, T. Cui, and F. Tian, “Impact of varying Nb content on conventional superconductivities in Nb-Si systems”, [Materials Today Communications](#) **38**, 107666 (2024).
- ¹⁷⁰D. Dew-Hughes, “Is Nb₃Si a 25 K superconductor?”, [Cryogenics](#) **26**, 660–664 (1986).
- ¹⁷¹T. Proslir, M. Kharitonov, M. Pellin, J. Zasadzinski, and Ciovati, “Evidence of Surface Paramagnetism in Niobium and Consequences for the Superconducting Cavity Surface Impedance”, [IEEE Transactions on Applied Superconductivity](#) **21**, 2619–2622 (2011).
- ¹⁷²A. Bargerbos, L. J. Splitthoff, M. Pita-Vidal, J. J. Wesdorp, Y. Liu, P. Krogstrup, L. P. Kouwenhoven, C. K. Andersen, and L. Grünhaupt, “Mitigation of Quasiparticle Loss in Superconducting Qubits by Phonon Scattering”, [Physical Review Applied](#) **19**, 024014 (2023).
- ¹⁷³X. Pan, Y. Zhou, H. Yuan, L. Nie, W. Wei, L. Zhang, J. Li, S. Liu, Z. H. Jiang, G. Catelani, L. Hu, F. Yan, and D. Yu, “Engineering superconducting qubits to reduce quasiparticles and charge noise”, [Nature Communications](#) **13**, 7196 (2022).
- ¹⁷⁴R. D. Chang, N. Shumiya, R. A. McLellan, Y. Zhang, M. P. Bland, F. Bahrami, J. Mun, C. Zhou, K. Kisslinger, G. Cheng, A. C. Pakpour-Tabrizi, N. Yao, Y. Zhu, M. Liu, R. J. Cava, S. Gopalakrishnan, A. A. Houck, and N. P. d. Leon, *Eliminating Surface Oxides of Superconducting Circuits with Noble Metal Encapsulation*, Aug. 2024.
- ¹⁷⁵M. Bal, A. A. Murthy, S. Zhu, F. Crisa, X. You, Z. Huang, T. Roy, J. Lee, D. v. Zanten, R. Pilipenko, I. Nekrashevich, A. Lunin, D. Bafia, Y. Krasnikova, C. J. Kopas, E. O. Lachman, D. Miller, J. Y. Mutus, M. J. Reagor, H. Cansizoglu, J. Marshall, D. P. Pappas, K. Vu, K. Yadavalli, J.-S. Oh, L. Zhou, M. J. Kramer, F. Lecocq, D. P. Goronzy, C. G. Torres-Castanedo, P. G. Pritchard, V. P. Dravid, J. M. Rondinelli, M. J. Bedzyk, M. C. Hersam, J. Zasadzinski, J. Koch,

- J. A. Sauls, A. Romanenko, and A. Grassellino, “Systematic improvements in transmon qubit coherence enabled by niobium surface encapsulation”, *npj Quantum Information* **10**, 1–8 (2024).
- ¹⁷⁶M. C. d. Ory, V. Rollano, D. Rodriguez, M. T. Magaz, D. Granados, and A. Gomez, “Low loss hybrid nb/au superconducting resonators for quantum circuit applications”, *Advanced Quantum Technologies*, 2400699 (2025).
- ¹⁷⁷J. P. Pekola, D. V. Anghel, T. I. Suppala, J. K. Suoknuuti, A. J. Manninen, and M. Manninen, “Trapping of quasiparticles of a nonequilibrium superconductor”, *Applied Physics Letters* **76**, 2782–2784 (2000).
- ¹⁷⁸R.-P. Riwar, A. Hosseinkhani, L. D. Burkhardt, Y. Y. Gao, R. J. Schoelkopf, L. I. Glazman, and G. Catelani, “Normal-metal quasiparticle traps for superconducting qubits”, *Physical Review B* **94**, 104516 (2016).
- ¹⁷⁹A. Hosseinkhani, R.-P. Riwar, R. Schoelkopf, L. Glazman, and G. Catelani, “Optimal Configurations for Normal-Metal Traps in Transmon Qubits”, *Physical Review Applied* **8**, 064028 (2017).
- ¹⁸⁰R.-P. Riwar, L. I. Glazman, and G. Catelani, “Dissipation by normal-metal traps in transmon qubits”, *Physical Review B* **98**, 024502 (2018).
- ¹⁸¹A. Hosseinkhani and G. Catelani, “Proximity effect in normal-metal quasiparticle traps”, *Physical Review B* **97**, 054513 (2018).
- ¹⁸²R.-P. Riwar and G. Catelani, “Efficient quasiparticle traps with low dissipation through gap engineering”, *Physical Review B* **100**, 144514 (2019).
- ¹⁸³J. Fuchs, P. W. Epperlein, M. Welte, and W. Eisenmenger, “Energy Gap Reduction in Superconducting Tin Films by Quasiparticle Injection”, *Physical Review Letters* **38**, 919–922 (1977).
- ¹⁸⁴F. Hübner, J. C. Lemyre, D. Beckmann, and H. v. Löhneysen, “Charge imbalance in superconductors in the low-temperature limit”, *Physical Review B* **81**, 184524 (2010).
- ¹⁸⁵S. Kolenda, M. J. Wolf, D. S. Golubev, A. D. Zaikin, and D. Beckmann, “Nonlocal transport and heating in superconductors under dual-bias conditions”, *Physical Review B* **88**, 174509 (2013).
- ¹⁸⁶C. H. L. Quay, D. Chevallier, C. Bena, and M. Aprili, “Spin imbalance and spin-charge separation in a mesoscopic superconductor”, *Nature Physics* **9**, 84–88 (2013).

- ¹⁸⁷M. J. Wolf, F. Hübler, S. Kolenda, H. V. Löhneysen, and D. Beckmann, “Spin injection from a normal metal into a mesoscopic superconductor”, *Physical Review B* **87**, 024517 (2013).
- ¹⁸⁸M. Kuzmanović, B. Y. Wu, M. Weideneder, C. H. L. Quay, and M. Aprili, “Evidence for spin-dependent energy transport in a superconductor”, *Nature Communications* **11**, 4336 (2020).
- ¹⁸⁹P. Maier and D. Beckmann, “Spin-dependent coupling of supercurrent and nonequilibrium quasiparticles in high-field superconductors”, *Physical Review B* **107**, 054504 (2023).
- ¹⁹⁰M. J. Wolf, F. Hübler, S. Kolenda, and D. Beckmann, “Charge and spin transport in mesoscopic superconductors”, *Beilstein Journal of Nanotechnology* **5**, 180–185 (2014).
- ¹⁹¹B. L. Al’tshuler and A. G. Aronov, “Magnetoresistance of thin films and of wires in a longitudinal magnetic field”, *JETP Letters* **33**, 515 (1981).
- ¹⁹²S. Wind, M. J. Rooks, V. Chandrasekhar, and D. E. Prober, “One-Dimensional Electron-Electron Scattering with Small Energy Transfers”, *Physical Review Letters* **57**, 633–636 (1986).
- ¹⁹³B. L. Altshuler, A. G. Aronov, and D. E. Khmel’nitsky, “Effects of electron-electron collisions with small energy transfers on quantum localisation”, *Journal of Physics C: Solid State Physics* **15**, 7367 (1982).
- ¹⁹⁴A. A. Golubov, E. P. Houwman, J. G. Gijssbertsen, J. Flokstra, H. Rogalla, J. B. le Grand, and P. A. J. de Korte, “Quasiparticle lifetimes and tunneling times in a superconductor-insulator-superconductor tunnel junction with spatially inhomogeneous electrodes”, *Physical Review B* **49**, 12953–12968 (1994).
- ¹⁹⁵H. Pothier, S. Guéron, N. O. Birge, D. Esteve, and M. H. Devoret, “Energy Distribution Function of Quasiparticles in Mesoscopic Wires”, *Physical Review Letters* **79**, 3490–3493 (1997).
- ¹⁹⁶P. Fulde, “High field superconductivity in thin films”, *Advances in Physics* **22**, 667–719 (1973).
- ¹⁹⁷D. Beckmann, “Spin Transport in High-Field Superconductors”, *Annalen der Physik* **536**, 2400054 (2024).
- ¹⁹⁸H. Shiba, “Classical Spins in Superconductors”, *Progress of Theoretical Physics* **40**, 435–451 (1968).
- ¹⁹⁹M. D. Daybell and W. A. Steyert, “Localized Magnetic Impurity States In Metals: Some Experimental Relationships”, *Reviews of Modern Physics* **40**, 380–389 (1968).

- ²⁰⁰N. E. Booth, “Quasiparticle trapping and the quasiparticle multiplier”, [Applied Physics Letters](#) **50**, 293–295 (1987).
- ²⁰¹G. Burnell, P. A. Warburton, and M. G. Blamire, “Inelastic quasiparticle scattering and multiplication in superconductors”, [Journal of Applied Physics](#) **76**, 1105–1110 (1994).
- ²⁰²A. A. Golubov and E. P. Houwman, “Quasiparticle relaxation rates in a spatially inhomogeneous superconductor”, [Physica C: Superconductivity](#) **205**, 147–153 (1993).
- ²⁰³M. Taupin, I. M. Khaymovich, M. Meschke, A. S. Mel’nikov, and J. P. Pekola, “Tunable quasiparticle trapping in Meissner and vortex states of mesoscopic superconductors”, [Nature Communications](#) **7**, 10977 (2016).
- ²⁰⁴J. Krause, G. Marchegiani, L. Janssen, G. Catelani, Y. Ando, and C. Dickel, “Quasiparticle effects in magnetic-field-resilient three-dimensional transmons”, [Physical Review Applied](#) **22**, 044063 (2024).

VITA

EDUCATION

- Northwestern University (NU)**
2018—2025
Doctor of Philosophy in Physics
PhD Advisor: Prof. Venkat Chandrasekhar
- University of Illinois at Urbana-Champaign (UIUC)**
2014—2018
Bachelor of Science in Physics
Minors in *Mathematics* and *Materials Science*

RESEARCH EXPERIENCE

- Graduate Research Assistant, NU, Chandrasekhar Group & SQMS**
2018 - Present
 — Studied non-equilibrium superconductivity in mesoscopic devices with a focus on mitigating quasiparticle poisoning via engineered relaxation in proximity bilayer devices, as part of the Superconducting Quantum Materials and Systems (SQMS) center hosted by Fermilab.
 — Examined the superconducting properties of niobium films in quantum applications with close ties to the Hersam and Bedzyk labs at NU, and occasional collaboration with Rigetti Computing.
 — Led transport studies of ferroic 2D materials in collaboration with the Dravid and Kanatzidis groups at NU, with an emphasis on magneto-electricity in vdW heterostructures with $M_2P_2S_6$ chalcophosphates.
 — Developed new instruments for: the assembly of vdW devices, cryogenic measurements at microwave frequency, e-beam lithography, transport measurements including low-noise amplifiers, microwave impedance microscopy, and feedback control of transport experiments.
- Undergraduate Research Assistant, UIUC, Dale van Harlingen Group**
2016 - 2018
 — Synthesized films of the cuprate superconductor $La_{1.8-x}Eu_{0.2}Sr_xCuO_4$ by pulsed laser deposition, and characterized their quality via x-ray diffraction and superconducting magnetic gradiometry.
- Summer Undergraduate Laboratory Intern, Argonne National Lab Superconductivity and Magnetism Group / Wai-Kwong Kwok Group**
2016 & 2017
 — Explored critical current enhancement in defect doped commercial high temperature superconductors.
 — Assisted on magneto-transport of magnetic/topological superconductors $EuRbFe_4As_4$ and $Nb_xBi_2Se_3$.

INSTRUCTIONAL EXPERIENCE

- **Graduate Teaching Assistant**, Northwestern University, Department of Physics
 - TA'd for introductory lab and lecture courses on kinematics, electrostatics and modern-physics/waves, and advanced E&M over the course of 5 quarters (4 in-person, 1 virtual).
- **Research Mentor**, Northwestern University, Mesoscopic Physics Group
 - Mentored and directed research projects for summer students (4 local highschoolers, 1 REU student), as well as long term junior projects by Northwestern undergraduates (7 students, 1 of which is currently in the lab, and 3 which are now in PhD programs) and Masters degree students (2 students, both now in PhD programs), primarily through hands on lab experiences with 2D materials, cryogenic instruments, and circuit design of electronics for transport measurements.

PUBLICATIONS AND TALKS

- ¹K. M. Ryan and V. Chandrasekhar, “Enhanced quasiparticle relaxation in a superconductor via the proximity effect”, [Applied Physics Letters](#) **127**, 072603 (2025).
- ²K. M. Ryan and V. Chandrasekhar, “Quasiparticle Injector-Detector Experiments on Superconductors and Proximity Effect Bilayers”, in APS March Meeting Abstracts, Vol. MAR-W24-10 (Mar. 21, 2025), W24–10.
- ³K. Ryan and V. Chandrasekhar, “Quasiparticle Relaxation in Superconductors Coupled to Normal Metals”, in [Bulletin of the American Physical Society](#) (Mar. 8, 2024).
- ⁴K. Ryan and V. Chandrasekhar, “Quasiparticle Calorimetry using Dayem-Bridges”, in [APS March Meeting Abstracts](#), Vol. 2023 (Mar. 2023), Y75–013.
- ⁵E. K. Qian, A. K. Iyer, M. Cheng, K. M. Ryan, L. Jirousek, D. G. Chica, P. Krantz, Y.-S. Lee, V. Chandrasekhar, V. P. Dravid, and M. G. Kanatzidis, “Synthesizing Mono- and Bimetallic 2D Selenophosphates Using a P₂Se₅ Reactive Flux”, [Chemistry of Materials](#) **35**, 3671–3685 (2023).
- ⁶L. Jirousek, K. Ryan, and V. Chandrasekhar, “Transport Behavior of Planar Fe₃GeTe₂ Josephson Junctions”, in [APS March Meeting Abstracts](#), Vol. 2023 (Mar. 2023), G00–014.
- ⁷K. M. Ryan, C. G. Torres-Castanedo, D. P. Goronzy, D. A. G. Wetten, M. Field, C. J. Kopas, J. Marshall, M. J. Reagor, M. J. Bedzyk, M. C. Hersam, and V. Chandrasekhar, “Characterization of Nb films for superconducting qubits using phase boundary measurements”, [Applied Physics Letters](#) **121**, 202601 (2022).

- ⁸K. Ryan, P. Krantz, C. Torres, P. Masih Das, K. Narayanachari, D. Goronzy, M. Bedzyk, V. Dravid, M. Hersam, A. McFadden, C. R. McRae, M. Field, C. Kopas, J. Marshall, M. Reagor, and V. Chandrasekhar, “Optimization of Nb Superconducting Films for Quantum Devices by HT Phase Boundary Analysis”, in [APS March Meeting Abstracts](#), Vol. 2022 (Mar. 2022), F36–007.
- ⁹P. Krantz, K. Ryan, E. Qian, A. Iyer, M. Cheng, Y.-S. Lee, V. Dravid, M. Kanatzidis, and V. Chandrasekhar, “Searching for Multiferroic Coupling in Stacked Chalcophosphate Heterostructures”, in [APS March Meeting Abstracts](#), Vol. 2022 (Mar. 2022), Y68–004.
- ¹⁰K. Ryan, P. Krantz, Z. Liu, D. Chica, A. Iyer, M. Cheng, V. Dravid, M. Kanatzidis, and V. Chandrasekhar, “Fabrication and Characterization of Metallic Thiophosphate Heterostructures: A Path Towards Magnetoelectric Transport Devices”, in [APS March Meeting Abstracts](#), Vol. 2021 (Mar. 2021), Y56–006.
- ¹¹D. G. Chica, A. K. Iyer, M. Cheng, K. M. Ryan, P. Krantz, C. Laing, R. dos Reis, V. Chandrasekhar, V. P. Dravid, and M. G. Kanatzidis, “P2S5 Reactive Flux Method for the Rapid Synthesis of Mono- and Bimetallic 2D Thiophosphates $M_2-xM'xP_2S_6$ ”, [Inorganic Chemistry](#) (2021).
- ¹²M. P. Smylie, K. Willa, J.-K. Bao, K. Ryan, Z. Islam, H. Claus, Y. Simsek, Z. Diao, A. Rydh, A. E. Koshelev, W.-K. Kwok, D. Y. Chung, M. G. Kanatzidis, and U. Welp, “Anisotropic superconductivity and magnetism in single-crystal $RbEuFe_4As_4$ ”, [Physical Review B](#) **98**, 104503 (2018).
- ¹³D. Hamilton, K. Ryan, T. Johnson, G. Gu, G. MacDougall, D. Van Harlingen, and A. Zakrzewski, “Signatures of pair-density wave order via phase sensitive measurement of $La_{2-x}Ba_xCuO_4$ and $La_{2-x-y}Eu_ySr_xCuO_4$ SQUIDs and Josephson junctions”, in [APS March Meeting Abstracts](#), Vol. 2018 (Mar. 2018), pp. L30–009.
- ¹⁴M. P. Smylie, K. Willa, K. Ryan, H. Claus, W. K. Kwok, Y. Qiu, Y. S. Hor, and U. Welp, “An increase in T_c under hydrostatic pressure in the superconducting doped topological insulator $Nb_{0.25}Bi_2Se_3$ ”, [Physica C: Superconductivity and its Applications](#) **543**, 58–61 (2017).